Towards a measurement of the nuclear magnetic octupole moment of barium-137

Adam Kleczewski

A dissertation submitted in partial fulfillment of
the requirements for the degree of

Doctor of Philosophy

University of Washington

2011

Program Authorized to Offer Degree: Department of Physics

University of Washington
Graduate School

This is to certify that I have examined this copy of a doctoral dissertation by

Adam Kleczewski

and have found that it is complete and satisfactory in all respects,
and that any and all revisions required by the final
examining committee have been made.

Chair of the Supervisory Committee:

_____

Boris Blinov

Reading Committee:

_____

Boris Blinov

_____

Norval Fortson

_____

Alejandro Garcia

Date: _____

In presenting this dissertation in partial fulfillment of the requirements for the doctoral degree at the University of Washington, I agree that the Library shall make its copies freely available for inspection. I further agree that extensive copying of this dissertation is allowable only for scholarly purposes, consistent with "fair use" as prescribed in the U.S. Copyright Law. Requests for copying or reproduction of this dissertation may be referred to Proquest Information and Learning, 300 North Zeeb Road, Ann Arbor, MI 48106-1346, 1-800-521-0600, to whom the author has granted "the right to reproduce and sell (a) copies of the manuscript in microform and/or (b) printed copies of the manuscript made from microform."

Signature_____

Date_____

University of Washington

Abstract

Towards a measurement of the nuclear magnetic octupole moment of barium-137

Adam Kleczewski

Chair of the Supervisory Committee:
Professor Boris Blinov
Physics

A description of a 2051 nm laser system designed and built for use in a number of proposed experiments is presented. Results of spectroscopic measurements of the $6S_{1/2}$ to $5D_{3/2}$ transition in $^{138}Ba^{+}$ are discussed. The laser is shown to produce coherent excitation of the atomic transition. The observed 2 ms laser-ion coherence times demonstrate the laser linewidth to be no more than 500 Hz. The proposed measurement of the nuclear magnetic octupole measurement of ^{137}Ba is reviewed. The prospects for developing this laser system into a barium ion optical frequency standard are discussed.

TABLE OF CONTENTS

LIST OF FIGURES

GLOSSARY

AOM: Acousto-Optic Modulator

CCD: Charged Cathode Device

ECDL: External cavity diode laser

EOM: Electro-Optic Modulator

HWP: Half wave plate

LED: Light Emitting Diode

NSM: Nuclear Shell Model

PBS: Polarizing Beam Splitter

PHA: Pulse Height Analyzer

PLL: Phase locked loop

PMT: Photo-Multiplier Tube

PNC: Parity Non-Conservation

PPLN: Periodically poled lithium niobate

QWP: Quarter wave plate

RWA: Rotating Wave Approximation

TAC: Time to Amplitude Converter

ULE: Ultra Low Expansion; as in ULE glass

DEDICATION

To my family for all their support

Chapter 1

INTRODUCTION

A single trapped ion is a nearly ideal environment for observing a wide range of quantum mechanical phenomena. In recent years a number of practical applications of ion traps have emerged. Optical atomic clocks referenced to a transition in a single trapped ion are on the verge of supplanting cesium atomic clocks as the world's primary frequency standard. The entangled state of a large number of trapped ions is currently the one of the most promising candidates for realizing a quantum computer. In addition to the emerging practical applications of ion trapping, precision measurements of the spectrum of a trapped ion are an effective method for testing quantum mechanics and other theories that could describe new physics. Barium ions in particular have a number of properties that make them particularly well suited for such precision measurements.

First, although barium is a rather heavy atom with 56 protons in its nucleus, barium ions have a simple electronic energy level structure. All but one of the 55 electrons in a barium ion exist in a fully occupied electron shell. In theoretical calculations of electron wavefunctions, these closed shell electrons can be treated as a radially symmetric charge distribution that screen the nuclear charge from the valence electron but otherwise do not contribute to the internal dynamics of the ion. A barium ion can therefore be treated as a single electron atom to very good approximation. Theoretical calculations can be carried out with much greater precision than usual for heavy atoms allowing for the interpretation of small shifts in the spectrum of Ba^+

Second, the $5D_{3/2}$ level in a barium ion is unusual in that its energy is greater than that of the ground state $6S_{1/2}$ level but lower than that of the $6P_{1/2}$ level. As a result the $5D_{3/2}$ level has a natural lifetime of approximately 80 seconds. It is possible to drive the ion from the $6S_{1/2}$ level to the $5D_{3/2}$ level via an electric quadrupole transition at 2051 nm. The stability of the $5D_{3/2}$ and the resulting narrow linewidth of the 2051 nm transition are

necessary for three proposed experiments.

The original motivation for the development of the 2051 nm laser system described in this thesis was a proposal to observe parity non-conservation (PNC) in a single trapped barium atom [25]. A discussion of this challenging experiment can be found in the theses of previous graduate students ([55] for example). While the work presented in this thesis represents an important step towards a PNC measurement, we are primarily motivated by the more immediate goals of measuring the nuclear magnetic octupole moment of ^{137}Ba.

Hyperfine shifts due to the magnetic dipole moment and electric quadrupole moment of nuclei with non-zero angular momentum have been resolved in numerous elements. However hyperfine shifts due to the magnetic octupole moment of a nucleus have only been observed in a handful of atoms. In nearly every case, interactions among valence electrons made it difficult to calculate electronic wavefunctions with sufficient precision to separate the determine a value for the nuclear magnetic octupole moment. One notable exception is a recent measurement of the hyperfine structure in the $6P_{3/2}$ level of ^{133}Cs. Like barium ions, neutral cesium atoms have only one valence electron so electronic wavefunctions are known remarkably well. The experimentally determined coupling constant combined with the theoretically calculated electronic wavefunctions implied a value for the nuclear magnetic octupole moment that was 40 times larger than the value predicted by the nuclear shell model. With the 2051 nm laser system we have developed it is straight forward processes to selectively populate $5D_{3/2}$ hyperfine sublevels of $^{137}Ba^{+}$. We can then perform precision RF spectroscopy to measure the hyperfine splittings. The long lifetime of the $5D_{3/2}$ level allows for a much greater level of precision than can be achieved in the $6P_{3/2}$ level of ^{133}Cs making it possible to resolve the nuclear magnetic octupole moment of ^{137}Ba even if it is smaller than the nuclear shell model prediction. A measurement of the nuclear magnetic octupole moment in barium could provide some insight into the unexpected result of the cesium measurement.

After completing the octupole measurement the 2051 nm laser will be converted into a optical frequency standard referenced to the $6S_{1/2}$ to $5D_{3/2}$ transition in $^{137}Ba^{+}$. This transition has a number of properties that make it an excellent candidate for clock work. All of the work presented in this thesis can be viewed as preliminary steps necessary for the

development of a barium ion optical frequency standard. The final chapter of this thesis contains a discussion of this project.

Chapter 2

ATOMIC PHYSICS

Trapping and laser cooling a single ion requires and understanding of a considerable amount of atomic physics. We present here an overview of atomic physics concepts necessary to understand the work that follows. For more detail the reader is referred to an introductory atomic physics text such as [24].

2.1 Barium Ion Energy Level Structure

We begin by presenting the a classical non-relativistic model of atomic structure. This model will allow us to explain nearly all of the features of barium ion necessary relevant to this work. In chapter 6 we will add to the our presentation of the hyperfine interaction to include higher order multipole corrections.

2.1.1 Central Field and Atomic Orbitals

The Coulomb interaction provides the attractive potential that binds electrons to nuclei. In the case of hydrogen we can write the Hamiltonian

$$H_{hyd} = -\frac{\hbar^2}{2m_e}\nabla^2 - \frac{e^2}{4\pi\epsilon_0 r} \tag{2.1}$$

where m_e is the mass of the electron, e is the charge of the electron ϵ_0, and $\hbar$ is the Planck constant divided by 2π. We can then derive the hydrogen wavefunctions labeled by quantum numbers n and l.

The electronic structure of a barium ion resembles that of a neutral alkali atom in that a single valence electron exists outside a number of closed electron shells. A complete theoretical treatment of the interactions among the constituent parts of a barium atom is beyond the scope of this thesis. Instead we will proceed by assuming that since closed electron shells form radially symmetric charge distributions and the nucleus can (for now)

be approximated as a point charge, the potential that attracts the outermost electron is radially symmetric. We will not concern ourselves with the exact form of the attractive potential but simply write the Hamiltonian as

$$H_{Ba} = -\frac{\hbar^2}{2m_e}\nabla^2 - V_{CF}(r) \tag{2.2}$$

where $V_{CF}(r)$ is the central field potential. We now turn our attention to the angular components of the problem.

This rather vaguely specified Hamiltonian yields a set of atomic orbitals that, just like in hydrogen, can be labeled by the quantum numbers n and l. However unlike in hydrogen, states where all levels with principal quantum number n have (nearly) the same energy, the energy of atomic orbitals in multi-electron atoms, such as barium, depend heavily on angular momentum. One consequence of the energy of an orbital depending on angular momentum is that the order in which atomic orbitals are filled can be modified. States with large amounts of angular momentum can have energies that exceed those of states with higher principal quantum numbers. A clear example of this which has important experimental implications is the fact that the 5D orbital in a barium ion has a higher energy than the 6S orbital.

2.1.2 Fine Structure

An electron moving with velocity $\vec{v}$ through the electric field $\vec{E}$ created by a positively charged nucleus "sees" a magnetic field of the form

$$\vec{B} = -\frac{1}{c^2}\vec{v} \times \vec{E}$$

arising from the Lorentz transform of the electric field.

An electron possess spin angular momentum and a magnetic dipole moment $\vec{\mu} = -g_s\mu_B\vec{S}$ where g_s is the Lande g factor for the electron, μ_B is the Bohr magneton, and $\vec{S}$ is the electron spin angular momentum operator. The interaction between the electron's magnetic dipole moment and the magnetic field seen by the orbiting electron is known as the spin-orbit interaction. The spin-orbit Hamiltonian is proportional to the scalar product of the

electron's orbital and spin angular momentum. Deriving the correct constant of proportionality requires a relativistic treatment of atomic structure beginning with the Dirac equation [54]. Instead we will simply write the spin-orbit Hamiltonian as

$$H_{SO} \propto \vec{S} \cdot \vec{L} \tag{2.3}$$

where $\vec{S}$ and $\vec{L}$ are the electronic spin and orbital angular momentum vector operators. If we include a $\vec{S} \cdot \vec{L}$ term in the Hamiltonian the states $|lm_l sm_s\rangle$ are no longer eigenstates of the Hamiltonian. If we define $\vec{J} = \vec{L} + \vec{S}$ and write the eigenstates as

$$|lsjm_j\rangle = \sum_{m_l, m_s} \langle lsjm_j|\, lm_l sm_s\rangle\, |lm_l sm_s\rangle \tag{2.4}$$

the states $|lsjm_j\rangle$ are eigenstates of the spin-orbit Hamiltonian. The matrix elements $\langle lsjm_j|\, lm_l sm_s\rangle$ are known as Clebsch-Gordan coefficients. The spin-orbit interaction breaks the degeneracy of the states $|lsjm_j\rangle$. These energy splittings are known as the fine structure.

2.1.3 Hyperfine Structure

A non-zero nuclear angular momentum vector defines an axis of cylindrical symmetry for the nucleus. In this case the non-uniform nuclear charge and current distributions will create electric and magnetic fields which will couple to the orbiting electrons. Electron fine structures levels will be split into hyperfine sublevels corresponding to different orientations of the nuclear angular momentum vector relative to the electronic angular momentum vector.

The standard way of treating the hyperfine interaction in elementary text books is to treat the nucleus like a point charge with spin angular momentum $\vec{I}$ and a magnetic dipole moment $\vec{\mu_N} = g_N \mu_B \vec{I}$ where g_N is the nuclear magneton. The nuclear angular magnetic dipole moment interacts with the magnetic field created by the moving electron giving rise to an additional term in the Hamiltonian of the form

$$H_{HF} = A\vec{I} \cdot \vec{J} \tag{2.5}$$

where A is a constant with units of energy.

Following the same procedure as we did for spin-orbit coupling we note that the states $|lsjm_j\rangle$ are not eigenstates of the hyperfine interaction Hamiltonian but if we define

$$\vec{F} \equiv \vec{J} + \vec{I}$$

$$\vec{I} \cdot \vec{J} = \frac{1}{2}\left(\left|\vec{F}\right|^2 - \left|\vec{I}\right|^2 - \left|\vec{J}\right|^2\right)$$

$$|JIFm_F\rangle = \sum_{m_J, m_I} \langle JIFm_F|\ Jm_J Im_I\rangle\, |Jm_J Im_I\rangle \tag{2.6}$$

the basis states $|JIFm_F\rangle$ are eigenstates of the hyperfine interaction Hamiltonian.

The hyperfine interaction eq. 2.5 lifts the energy degeneracy of the states $|JIFm_F\rangle$. The energy shifts that arise from the dipole hyperfine interaction can be written as

$$\begin{aligned} E_{HF} &= A\left\langle \vec{I} \cdot \vec{J} \right\rangle \\ &= \frac{A}{2}\left[F(F-1) - I(I-1) - J(J-1)\right] \end{aligned} \tag{2.7}$$

This equation implies the following relationship between the energy interval separating two hyperfine sublevels with angular momentum F and $F-1$.

$$E_F - E_{F-1} = AF \tag{2.8}$$

The experimentally measured values for the hyperfine splittings in the $6S_{1/2}$, $6P_{1/2}$, $5D_{3/2}$, and $5D_{5/2}$ levels of ^{137}Ba are shown in figure 2.1. These levels clearly violate the interval rule. In chapter 6 we will resolve this discrepancy by presenting a more sophisticated treatment of the hyperfine interaction which includes the effect of higher order discrepancy corrections.

2.2 Atomic Transitions

Here we review the classic problem of a single atom interacting with monochromatic radiation. We follow a standard treatment found in many introductory atomic physics texts ([24] for example).

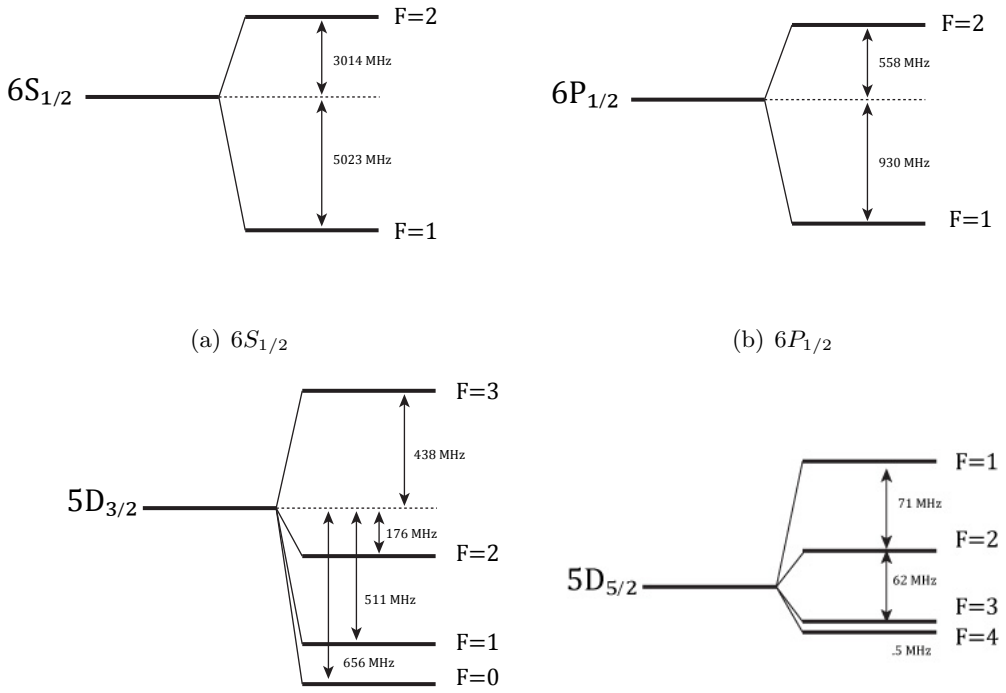

(a) $6S_{1/2}$ (b) $6P_{1/2}$

(c) $5D_{3/2}$ (d) $5D_{5/2}$

Figure 2.1: Hyperfine splittings in a ^{137}Ba ion. Note the different energy scales in each figure. These intervals have been previously published in the literature [17, 61, 65]

The experiments discussed in this thesis employ a variety of sources of electro-magnetic radiation to drive atomic transitions. Consider an electron bound to a nucleus system with states $|n\rangle$ that satisfy the time-independent Schroedinger equation

$$H_0 |n\rangle = E_n |n\rangle \tag{2.9}$$

$$H_0 = \frac{\vec{p}^2}{2m_e} + V \tag{2.10}$$

where $\vec{p}$ is the momentum of the electron. V contains the $1/r$ Coulomb potential and other terms that give rise to fine structure and possibly hyperfine structure . Suppose the bound electron interacts with an electromagnetic field defined by a vector potential

$$\vec{A} = 2A_0 \cos\left(\omega t - \vec{k}\cdot\vec{r}\right)\hat{n} \tag{2.11}$$

where ω is the radial frequency of the oscillating vector potential, $\vec{k}$ is the wavevector of the plane wave, and $\hat{n}$ is a unit vector. The Hamiltonian then becomes

$$H = \frac{1}{2m_e}\left(\vec{p} + e\vec{A}\right)^2 + eV \tag{2.12}$$

In writing this Hamiltonian we have neglected the spin of the electron which would couple to the magnetic field arising from the vector potential. Although this is a fairly serious omission, the qualitative features of the physics we wish to illustrate with this model will be unchanged.

Adopting the gauge condition $\nabla \cdot \vec{A} = 0$ orients the electric field parallel to $\vec{A}$ and allows us to write $\vec{p}\vec{A} + \vec{A}\vec{p} = 2\vec{p}\vec{A}$. After dropping terms of order $\vec{A}^2$ which describe two-photon interactions that are not relevant to this work, the Hamiltonian can be written as $H = H_0 + H'$ with

$$H' = \frac{eA_0}{m_e}\left(\vec{p}\cdot\hat{n}\right)\cos\left(\omega t - \vec{k}\cdot\vec{r}\right)$$

Let us now restrict ourselves to a two level atomic system consisting of the eigenstates $|1\rangle$ and $|2\rangle$. The wavefunction $|\Psi(\vec{r},t)\rangle$ of this system is

$$|\Psi(r,t)\rangle = c_1(t)\,|1\rangle\, e^{-i\omega_1 t} + c_2(t)\,|2\rangle\, e^{-i\omega_2 t} \tag{2.13}$$

where $\omega_n = E_n/\hbar$ and $c_1(t)$ and $c_2(t)$ are amplitudes that satisfy the normalization condition

$$|c_1(t)|^2 + |c_2(t)|^2 = 1$$

$|c_1(t)|^2$ and $|c_2(t)|^2$ represent the probability of finding the quantum system in the state $|1\rangle$ or $|2\rangle$.

$$i\hbar\dot{c_1} = c_2 \left\langle 1\right| H' \left|2\right\rangle e^{-i\omega_0 t} \tag{2.14a}$$

$$i\hbar\dot{c_2} = c_1 \left\langle 2\right| H' \left|1\right\rangle e^{i\omega_0 t} \tag{2.14b}$$

where $\omega_0 = \omega_2 - \omega_1$. The time dependent exponentials in equation 2.13 will combine with the exponentials in equations 2.14a and 2.14a. Terms that have $e^{i(\omega+\omega_0)t}$ time dependence will oscillate rapidly and can be neglected for our purposes. This is known as the rotating wave approximation (RWA). We can write the result so far compactly as

$$i\dot{c_1} = c_2 e^{i(\omega-\omega_0)t}\Omega \tag{2.15a}$$

$$i\dot{c_2} = c_1 e^{-i(\omega-\omega_0)t}\Omega^* \tag{2.15b}$$

where

$$\Omega = \frac{eA_0}{\hbar m} \left\langle 1\right| (\vec{p}\cdot\hat{n})\, e^{i\vec{k}\cdot\vec{r}} \left|2\right\rangle \tag{2.16}$$

is the Rabi frequency. Combining the differential equations 2.15a and 2.15b yields

$$\ddot{c_2} + i(\omega-\omega_0)\dot{c_2} + \left|\frac{\Omega}{2}\right|^2 c_2 = 0 \tag{2.17}$$

Taking $c_1(0) = 1$ and $c_2(0) = 0$ as boundary conditions results in the following expression for the population of the excited state as a function of time.

$$|c_2(t)|^2 = \frac{\Omega^2}{W^2}\sin^2\left(\frac{Wt}{2}\right) \tag{2.18}$$

where $W^2 = \Omega^2 + \delta^2$ and $\delta = \omega - \omega_0$. W is known as the generalized Rabi frequency.

With a laser tuned such that $\delta = 0$ the probability of finding the ion in the excited state as a function of time oscillates between 0 and 100% at a frequency of $\frac{\Omega}{2\pi}$. Detuning the laser from resonance reduces the contrast between the maximum and minimum excitation probabilities and increases the frequency of oscillation as shown in figure 2.2.

These oscillations in the population of the two level system, or 'Rabi flops', cannot continue indefinitely. Spontaneous emission from the excited state randomize the phase of the atom, variations in the external magnetic field shift the frequency of the atomic

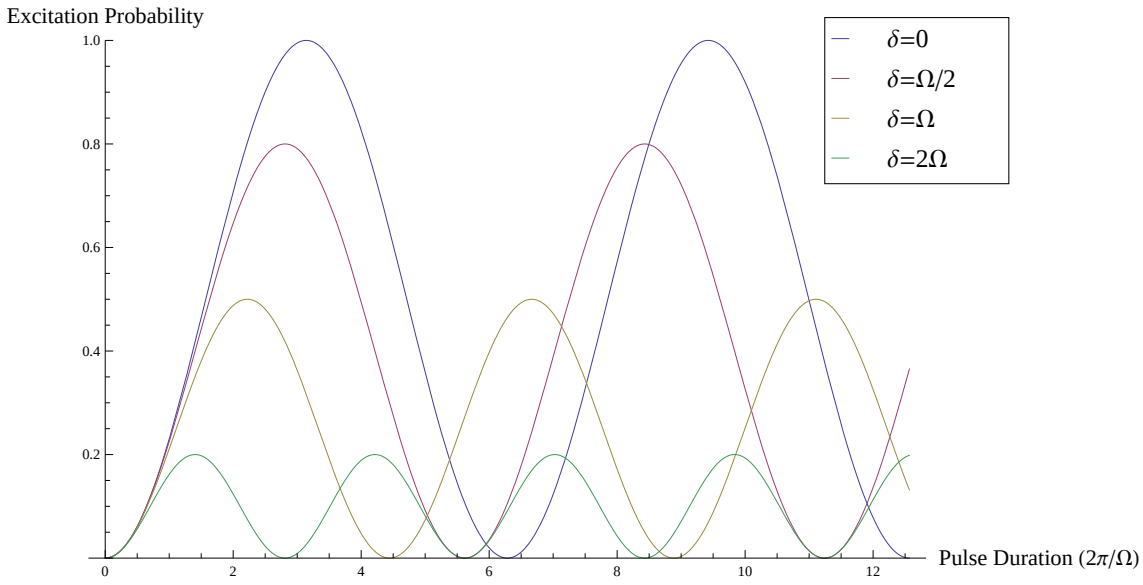

Figure 2.2: Probability of excitation to an excited quantum state as a function of interaction time for a variety of frequency detunings.

resonance away from the laser frequency, and frequency instabilities in the laser cause the laser to drift off of the atomic resonance. All of these decoherence processes, and many more, combine to damp the oscillations seen in figure 2.2. After the ion and the laser lose their phase relationship the population of the excited state levels off at 50%.

To capture this behavior we modify eq. 2.18 by making use of the trigonometric identity $\sin^2(x) = \frac{1}{2}(1-\cos(2x))$ and damping the oscillatory term with a decaying exponential with a time constant τ. A plot of this function is shown in figure 2.3.

$$\begin{aligned} |c_2(t)|^2 &= \frac{\Omega^2}{2W^2}\left(1 - e^{-\frac{t}{\tau}}\cos\left(Wt\right)\right) \\ &= \frac{\Omega^2}{2(\Omega^2+\delta^2)}\left(1 - e^{-\frac{t}{\tau}}\cos\left(\sqrt{\Omega^2+\delta^2}t\right)\right) \end{aligned} \tag{2.19}$$

If we choose exposure times t that are short compared to the decoherence time of the laser/ion system (τ) and plot $|c_2(t)|^2$ as a function of δ (equivalent to plotting as a function of laser frequency) we have the spectra shown in figure 2.4

2.3 Driving Electric and Magnetic Multipole Transitions with Plane Wave Radiation

In the previous section we expressed the population of an excited state in terms of a matrix element

$$\left\langle 1\right| \left(\vec{p}\cdot\hat{n}\right) e^{i\vec{k}\cdot\vec{r}} \left|2\right\rangle$$

For atomic length scales the position of the electrons r is on the order of the Bohr radius a_0 while the wavelength of the radiation used to drive an atomic transition is typically much larger.

$$kr \sim \frac{a_0}{\lambda} \ll 1$$

This allows us to Taylor expand the exponential in eq. 2.16 about the origin. Furthermore let an externally applied magnetic field pointing in the $+\hat{z}$ direction provide a quantization axis for the atom.

Suppose the atomic states $|1\rangle$ and $|2\rangle$ have angular momenta L and L' with magnetic

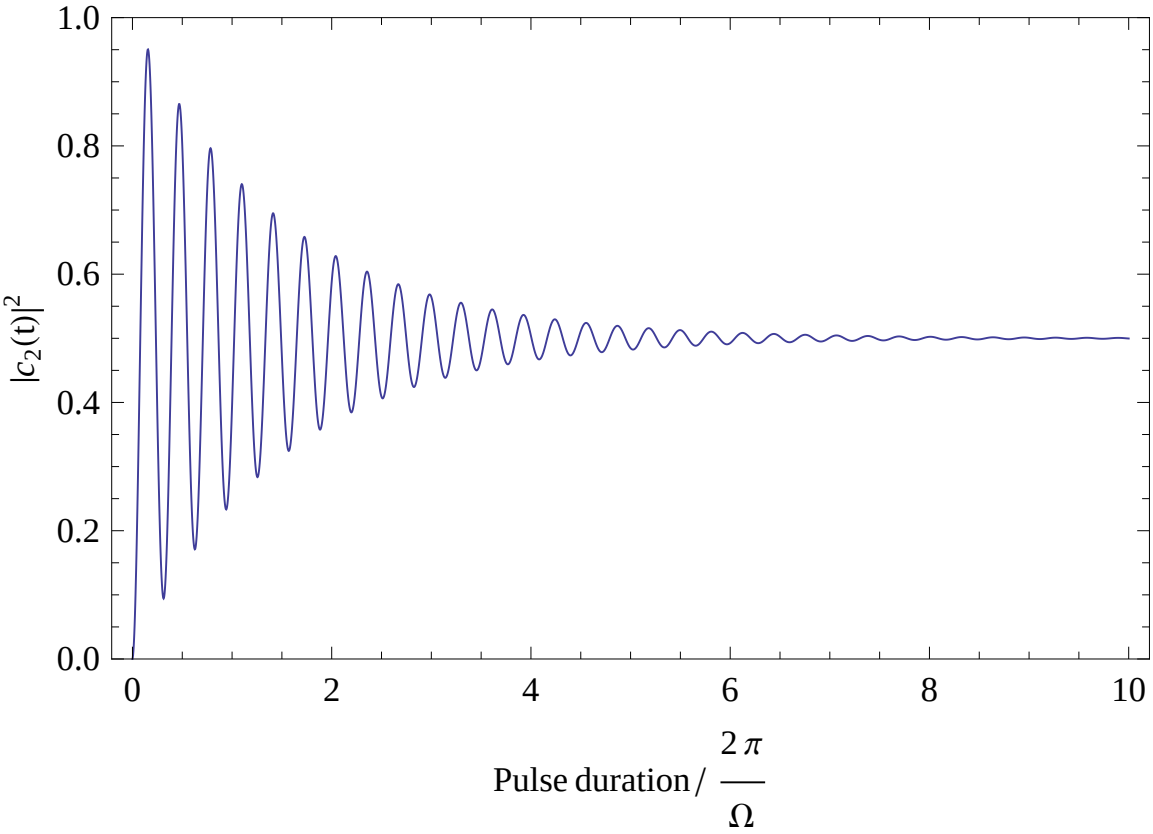

Figure 2.3: Decoherence processes limit the number of oscillations in state population that can be observed.

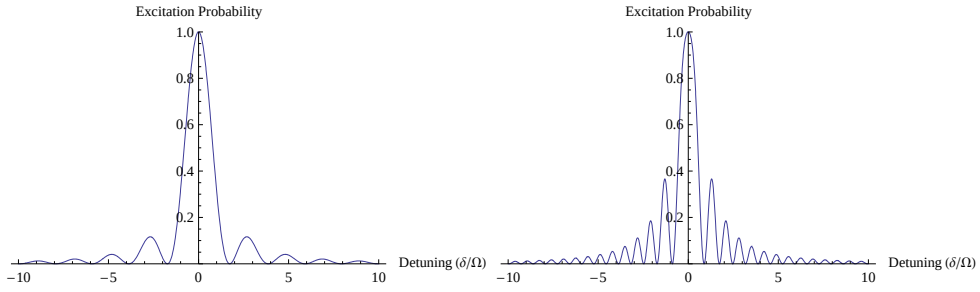

(a) $t = \frac{\pi}{\Omega}$, $\tau = \infty$ (b) $t = \frac{3\pi}{\Omega}$, $\tau = \infty$

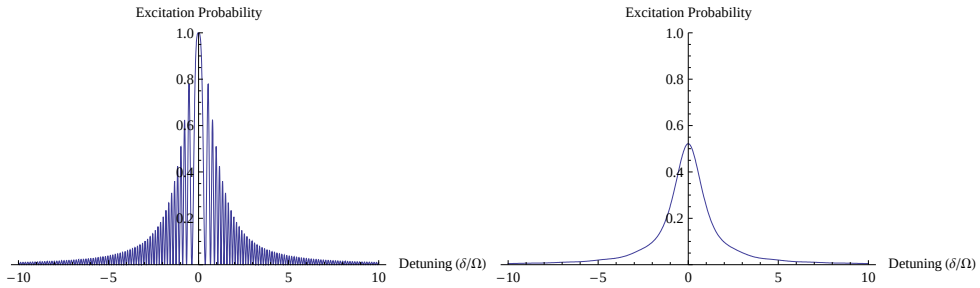

(c) $t = \frac{15\pi}{\Omega}$, $\tau = \infty$ (d) $t = \frac{\pi}{\Omega}$, $\tau = \pi$

Figure 2.4: For a given interaction time a scan of laser frequency over an atomic resonance produces different spectral lineshapes. Longer interaction times lead to sharper features in frequency space.

quantum numbers m and m' all other quantum numbers are represented by γ and γ'.

$$\begin{aligned}\Omega &= \frac{eA_0}{\hbar m_e}\left\langle \gamma' L' m' \right| (\vec{p}\cdot\hat{n})\left(1 + i\vec{k}\cdot\vec{r} + \cdots\right)\left|\gamma L m\right\rangle \\ &= \frac{eA_0}{\hbar m_e}\left\langle \gamma' L' m' \right| (\vec{p}\cdot\hat{n})\left|\gamma L m\right\rangle + \frac{ieA_0}{\hbar m_e}\left\langle \gamma' L' m' \right| (\vec{p}\cdot\hat{n})\left(\vec{k}\cdot\vec{r}\right)\left|\gamma L m\right\rangle + \cdots \end{aligned} \tag{2.20}$$

The first term in this expansion leads to a matrix element

$$\begin{aligned}\Omega_{E1} &= \frac{eA_0}{\hbar m_e}\left\langle \gamma' L' m' \right| \vec{p}\cdot\hat{n}\left|\gamma L m\right\rangle \\ &= \frac{eA_0}{\hbar m_e}\left\langle \gamma L' m' \right| \frac{-im_e}{\hbar}[H_0, r]\cdot\hat{n}\left|\gamma L m\right\rangle \\ &= -\frac{ie}{\hbar}\vec{E}\cdot\left\langle \gamma' L' m' \right| \vec{r}\left|\gamma L m\right\rangle \end{aligned} \tag{2.21}$$

where we have made the assumption that the frequency of the plane wave radiation ω is tuned to the center of the atomic transition allowing us to identify the electric field vector $\vec{E} = A_0\omega_{12}\hat{n}$. The vectors $\vec{E}$ and $\vec{r}$ in this expression can be written as a rank-1 spherical tensor using the following transformation for a vector $\vec{V} = (V_x, V_y, V_z)$

$$\begin{aligned} V_{+1}^{(1)} &= -\frac{V_x - iV_y}{\sqrt{2}} \\ V_{-1}^{(1)} &= \frac{V_x + iV_y}{\sqrt{2}} \\ V_0^{(1)} &= V_z \end{aligned}$$

The position operator contained in the matrix element in eq. 2.21 therefore connects states that differ in angular momentum by one ($|L - L'| = 1$). Unless this matrix element is equal to zero it will be the dominant contribution to the Rabi frequency. If this first term is equal to zero the transition may still occur but it will do so as a result of a higher order term in eq. 2.20.

Let us now consider the second term in eq. 2.20 which we can rewrite using the Einstein summation convention.

$$\frac{ieA_0}{\hbar m_e}\left\langle L' m' \right| (\vec{p}\cdot\hat{n})\left(\vec{k}\cdot\vec{r}\right)\left|L m\right\rangle = \frac{ieA_0}{\hbar m_e} n_i k_j \left\langle L' m' \right| p_i r_j \left|L m\right\rangle \tag{2.22}$$

We make use of the following decomposition of the outer product formed by two Cartesian

tensors [52].

$$U_iV_j = \underbrace{\frac{\vec{U}\cdot\vec{V}}{3}\delta_{ij}}_{\text{scalar}} + \underbrace{\frac{U_iV_j - U_jV_i}{2}}_{\text{vector}} + \underbrace{\left(\frac{U_iV_j + U_jV_i}{2} - \frac{\vec{U}\cdot\vec{V}}{3}\delta_{ij}\right)}_{\text{rank-2 tensor}} \tag{2.23}$$

The dyadics n_ik_j and p_ir_j can each be decomposed into components that transform like a scalar, a vector, and a rank-2 spherical tensor. In the gauge we have chosen, the vector potential is perpendicular to the wave vector ($\vec{n}\cdot\vec{k} = 0$) so the scalar component of the n_ik_j dyadic vanishes.

$$n_ik_j = \cancelto{0}{\frac{\vec{n}\cdot\vec{k}}{3}\delta_{ij}} + \underbrace{\frac{n_ik_j - n_jk_i}{2}}_{\vec{n}\times\vec{k}=\frac{\vec{B}}{A_0}} + \left(\frac{n_ik_j + n_jk_i}{2} - \cancelto{0}{\frac{\vec{n}\cdot\vec{k}}{3}\delta_{ij}}\right) \tag{2.24}$$

After performing the same decomposition on the p_ir_j dyadic we can identify the vector component as the orbital angular momentum operator.

$$p_ir_j = \frac{\vec{p}\cdot\vec{r}}{3}\delta_{ij} + \underbrace{\frac{p_ir_j - p_jr_i}{2}}_{\vec{p}\times\vec{r}=-\vec{L}} + \left(\frac{p_ir_j + p_jr_i}{2} - \frac{\vec{p}\cdot\vec{r}}{3}\delta_{ij}\right) \tag{2.25}$$

The product of equations 2.24 and 2.25 summed over i and j leads to two non-vanishing terms; a product rank-1 terms which have the form of a magnetic dipole interaction, and a product of the rank-2 terms which have the form of an electric quadrupole interaction. We can write the second term in eq. 2.20 as

$$\frac{ieA_0}{\hbar m_e}n_ik_j \left\langle j'm'\right| p_ir_j \left|jm\right\rangle = \frac{ie}{2\hbar m_e}B_i \left\langle j'm'\right| L_i \left|jm\right\rangle + \frac{e}{2\hbar}E_{ij} \left\langle j'm'\right| Q_{ij} \left|jm\right\rangle \tag{2.26}$$

where $Q_{ij} = r_ir_j - \frac{r^2}{3}\delta_{ij}$ is the quadrupole moment operator and $E_{ij} = E_0\left(\frac{n_ik_j+n_jk_i}{2}\right)$ is a symmetric rank-2 tensor describing the gradient of the electric field. If we write the tensors in this expression in the spherical basis and combine it with eq. 2.21 we can write the expansion of the Rabi frequency to second order in $\vec{k}\cdot\vec{r}$ as the sum of an electric dipole contribution, a magnetic dipole contribution, and an electric quadrupole contribution.

$$\Omega = -\frac{ie}{\hbar}E_q^{(1)}\left\langle j'm'\right| r_q^{(1)}\left|jm\right\rangle + \frac{e}{4\hbar m_e}B^{(1)}\left\langle j'm'\right| J_q^{(1)}\left|jm\right\rangle - \frac{ie}{\hbar}E_q^{(2)}\left\langle j'm'\right| Q_q^{(2)}\left|jm\right\rangle + \cdots \tag{2.27}$$

The angular dependence of each of these terms can be isolated using the Wigner-Eckart theorem.

$$\left\langle j'm' \right| T_q^{(k)} \left| jm \right\rangle = \left\langle jk, mq \right| j'm' \rangle \frac{\left\langle j \left\| T^{(k)} \right\| j' \right\rangle}{\sqrt{2j+1}} \tag{2.28}$$

The double barred matrix elements are known as reduced matrix elements.

$$\begin{aligned} \Omega = -\frac{ie}{\hbar} \left\langle j' \left\| r^{(1)} \right\| j \right\rangle \sum_{q=-1}^{1} \left\langle j1, mq \right| j'm' \rangle E_q^{(1)} \\ + \frac{e}{4\hbar m_e} B^{(1)} \left\langle j' \left\| J^{(1)} \right\| j \right\rangle \sum_{q=-1}^{1} \left\langle j1, mq \right| j'm' \rangle B_q^{(1)} \\ - \frac{ie}{\hbar} \left\langle j' \left\| Q^{(2)} \right\| j \right\rangle \sum_{q=-2}^{2} \left\langle j2, mq \right| j'm' \rangle E_q^{(2)} + \cdots \end{aligned} \tag{2.29}$$

Now all of the angular dependence in the problem is contained in the field tensors $E^{(1)}$, $B^{(1)}$, and $E^{(2)}$. To make the spatial dependence of the Rabi frequency more explicit, let us assume that the wavevector for the laser beam makes angle ϕ with the quantization axis and has zero projection on the y-axis. The vector potential (which in this case is parallel to the electric field) must be perpendicular to the wavevector but it forms an angle γ to with the quantization axis as illustrated in figure 2.5.

$$\begin{aligned} \vec{B} &= B(0, 0, 1) \\ \vec{k} &= k(\sin\phi, 0, \cos\phi) \\ \hat{n} &= (\cos\gamma\cos\phi, \sin\gamma, -\cos\gamma\sin\phi) \end{aligned} \tag{2.30}$$

The strength of a transition scales with the square of the Rabi frequency so let us make two dimensional plots in the ϕ-γ parameter space of the transition strength of the types of transition used in this work (electric dipole, magnetic dipole, and electric quadrupole) for each of the allowed changes in magnetic quantum number. We will refer to these plots shown in figures 2.6, 2.7, and 2.8 repeatedly when discussing the alignment of laser beams.

2.4 The Zeeman Effect

The quantization of angular momentum allows the component of an atom's angular momentum vector parallel to the quantization axis to take on 2J+1 different values. In the

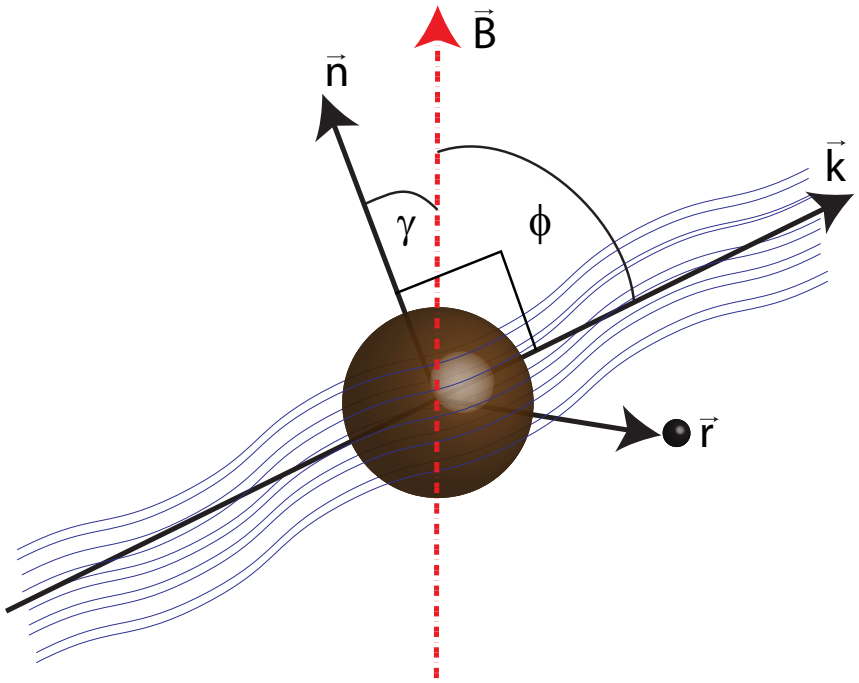

Figure 2.5: An 'artistic' representation of monochromatic radiation incident on an ion. The incident beam makes an angle ϕ with the quantization axis. The electric field vector makes an angle γ with the quantization axis.

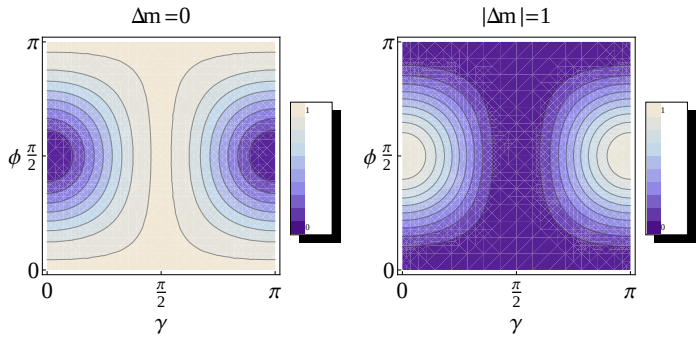

(a) (b)

Figure 2.6: Angular dependence of an electric dipole matrix element with the conventions defined in the text.

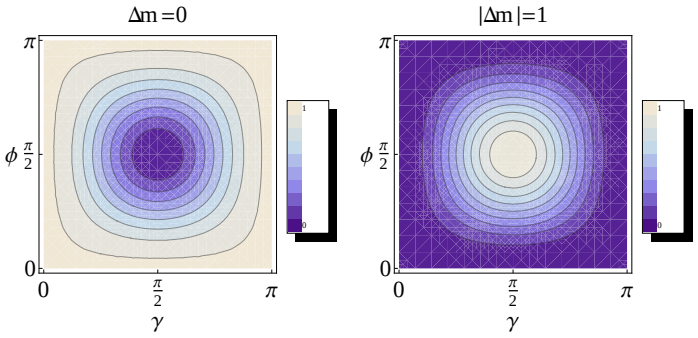

(a) (b)

Figure 2.7: Angular dependence of a magnetic dipole matrix element with the conventions defined in the text.

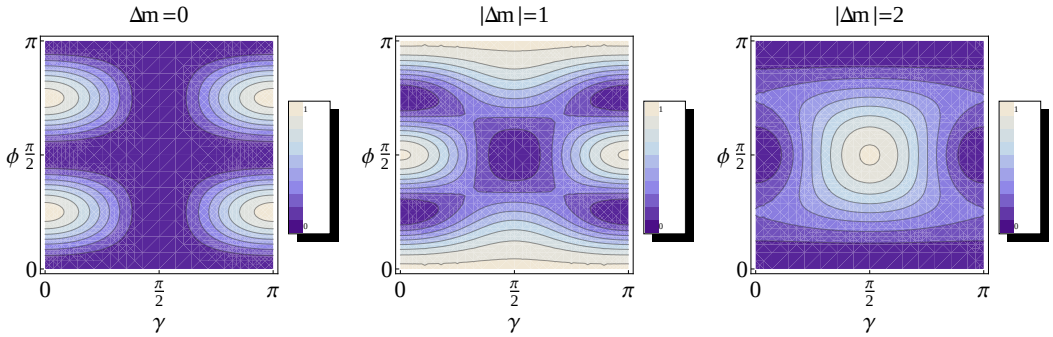

(a) (b) (c)

Figure 2.8: Angular dependence of an electric quadrupole matrix element with the conventions defined in the text.

absence of any preferred direction the 2J+1 states corresponding to different angular momentum orientations are degenerate in energy. An externally applied magnetic field breaks this degeneracy. The magnetic dipole moment of an atom (assuming no nuclear spin) is

$$\vec{\mu} = -\mu_B \vec{L} - g_s \mu_B \vec{S}$$

This dipole moment couples to the external magnetic field which we will take to point in the $\hat{z}$ direction and perturbs the states $|LSJm_J\rangle$. The first order correction to the energy of a state with magnetic quantum number m_J in the presence of an external magnetic field can be shown to be [68]

$$\begin{aligned} E_{ZE} &= \left\langle LSJm_J \right| \vec{\mu} \cdot \vec{B} \left| LSJm_J \right\rangle \\ &= g_J \mu_B B m_J \end{aligned} \tag{2.31}$$

where

$$g_J = \frac{J(J+1) + J(J+1) - S(S+1)}{2J(J+1)} + g_s \frac{J(J+1) - L(L+1) + S(S+1)}{2J(2J+1)} \tag{2.32}$$

The electron g-factor g_s has been measured to with extremely high precision [31] to be

$$g_s = 2.00231930436146(56)$$

The other relevant g-factors for barium can be found in [26] [36]

$$g_J(6S_{1/2}) = 2.0024922(10)$$
$$g_J(5D_{3/2}) = 0.7993278(3)$$
$$g_I(^{137}\mathrm{Ba}) = 0.623876(3)$$

Since the fine-structure energy scale is much greater than the magnitude of the Zeeman shifts higher order perturbative corrections are suppressed by a large energy denominator. Plots of the energy shifts resulting from the Zeeman effect in the $6S_{1/2}$ and $5D_{3/2}$ levels of $^{138}Ba^{+}$ are shown in figure 2.9.

The first order Zeeman shift to an electron state in an atom with nuclear spin is

$$E'_Z = g_F \mu_B B m_F \tag{2.33}$$

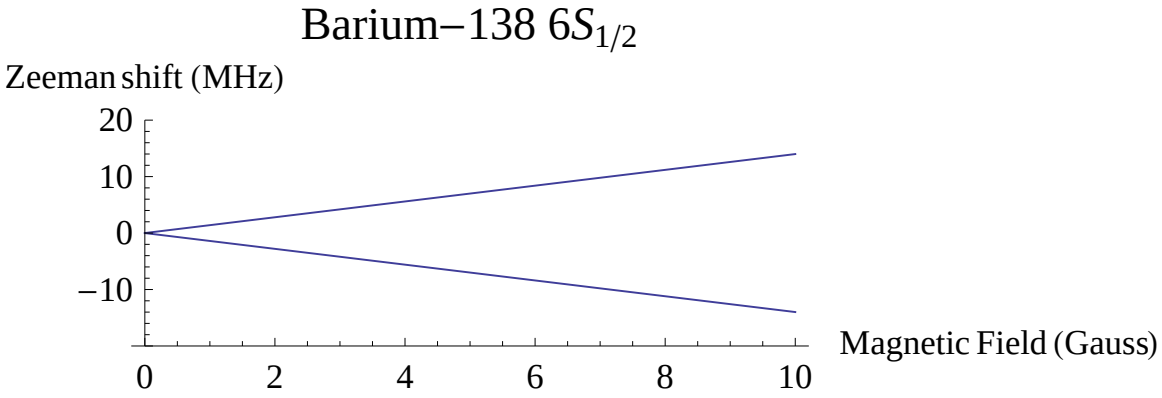

(a)

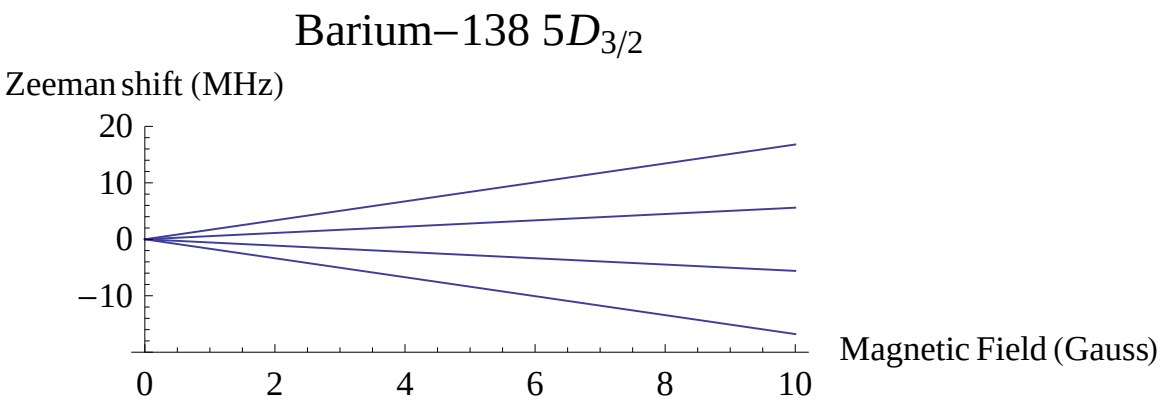

(b)

Figure 2.9: Zeeman shifts to the $6S_{1/2}$ and $5_{3/2}$ levels in ^{138}Ba as a function of magnetic field.

The g-factor for a hyperfine sublevel with angular momentum F is

$$g_F = g_J \frac{F(F+1) + J(J+1) - I(I+1)}{2F(F+1)} - g'_I \frac{F(F+1) - J(J+1) + I(I+1)}{2F(F+1)} \tag{2.34}$$

where $g'_I = g_I \frac{\mu_N}{\mu_B}$. Since the Bohr magneton μ_B is three orders of magnitude larger than the nuclear magneton μ_N the second term in eq. 2.34 can be ignored.

Hyperfine structure is a factor of $\frac{\mu_N}{\mu_B} \approx \frac{1}{1000}$ smaller than fine-structure. As a result there can be significant coupling between states with the same magnetic quantum number m but different values for F. Second order corrections must be taken into account.

$$E''_Z = \sum_{F'} \frac{|\langle JIFm_F| \, g_J \mu_B B J_z \, |JIF'm_F\rangle|^2}{E_F - E_{F'}} \tag{2.35}$$

The precision experiments we plan to carry out with our 2051 nm laser system rely on the fact that, to first order, states with $m_F = 0$ are insensitive to magnetic field fluctuations. It is important to account for the effect of second order Zeeman shifts as they can be a source of systematic error. For a discussion of the effect of second-order Zeeman shifts on a measurement of $5D_{3/2}$ hyperfine structure see section 6.4.2. Plots of the energy shifts resulting from the Zeeman effect in the $6S_{1/2}$ and $5D_{3/2}$ levels of $^{137}Ba^+$ are shown in figures 2.11.

2.5 Optical Pumping

Optical pumping is the process of forcing a quantum system into a well defined quantum state through the use of electro-magnetic radiation. In ^{138}Ba the $6S_{1/2}$ level splits into two Zeeman sub-levels with magnetic quantum numbers -1/2 and +1/2. Optically pumping into either of these states can be achieved by addressing the ion with circularly polarized 493 nm light traveling parallel to the quantization axis. Light with this polarization and alignment relative to the quantization axis is sometimes referred to as 'σ-light' since it only drives 'σ-transitions' (i.e. transitions with $\Delta m = \pm 1$). Similarly, a beam whose wavevector makes a 90 degree angle with the quantization axis and whose polarization vector is parallel to the the quantization axis is sometimes referred to as 'π-light'. Figures 2.12(a) and 2.12(c) illustrate the effect of σ and π light on a ^{138}Ba ion.

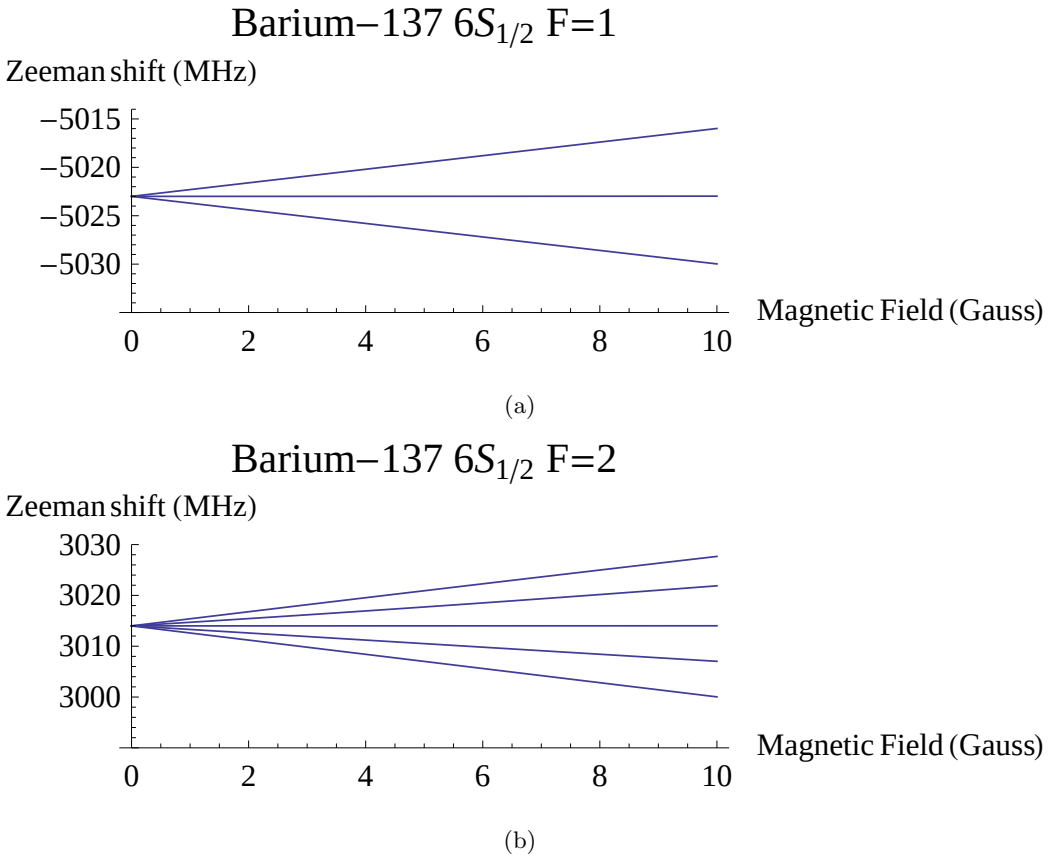

Figure 2.10: Zeeman shifts to the $6S_{1/2}$ level in ^{137}Ba as a function of magnetic field.

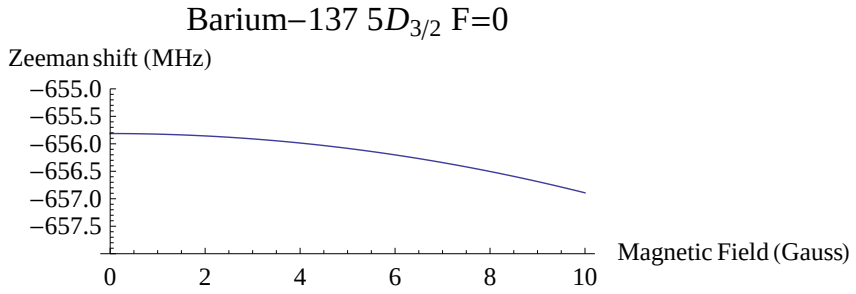

(a)

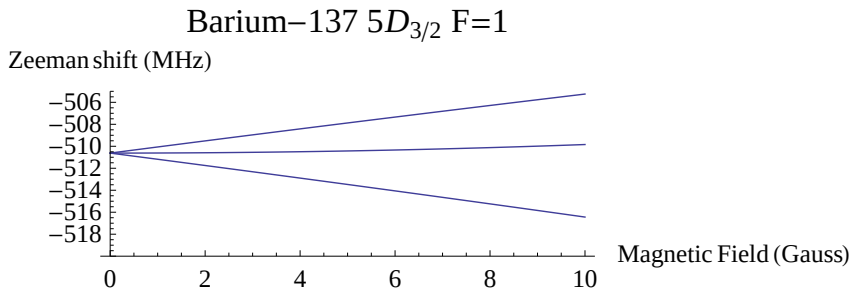

(b)

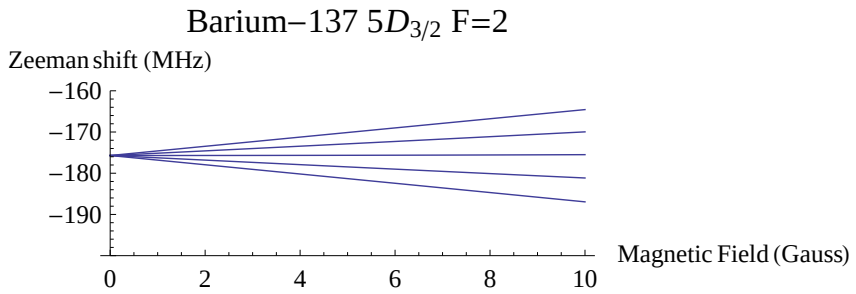

(c)

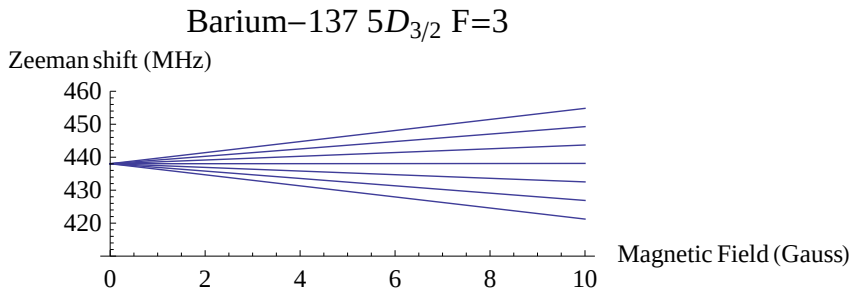

(d)

Figure 2.11: Zeeman shifts to the $5D_{3/2}$ level in $^{137}Ba^{+}$ as a function of magnetic field.

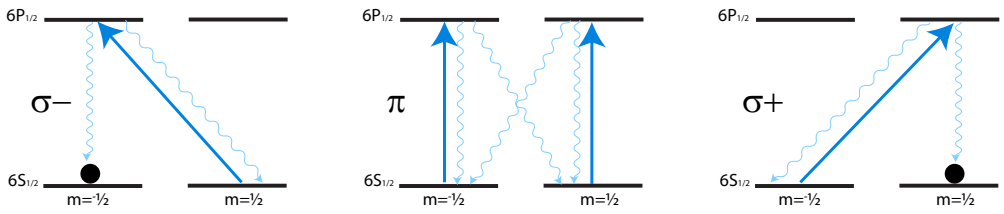

(a) σ_- light (b) π light (c) σ_+ light

Figure 2.12: Optical pumping in $^{138}Ba^+$. σ_+, and σ_- light each optically to a different $6S_{1/2}$ Zeeman level. The ion stays bright when exposed to π light.

We can optically pump a ^{137}Ba ion into a well defined $6S_{1/2}$ state with σ^+ or σ^- light as illustrated in figures 2.13(a) and 2.13(c). We are also able to optically pump to the $F = 2$ $m = 0$ state in the $6S_{1/2}$ level of $^{137}Ba^+$ by addressing the ion with π-light. That π-light should optically pump is not obvious. It relies on the fact that the Clebsch-Gordan coefficient $\langle Jm_Jk0|\ Jm_J\rangle = 0$. For an interesting discussion of this selection rule see [12].

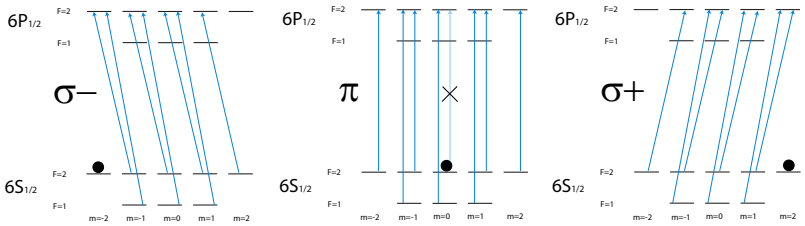

(a) σ_- light (b) π light (c) σ_+ light

Figure 2.13: In a ^{137}Ba ion optical pumping on the 493 nm $6S_{1/2}$ to $6P_{1/2}$ transition can be achieved with σ_+, σ_-, or π light.

2.6 Isotope Shift

The preceding discussion has assumed that the nucleus was an infinitely massive point charge. Including the finite mass and volume of the nucleus in our model of an atom

introduces energy level shifts that depend on the number of neutrons in the nucleus [24]. The presence of isotope shifts have practical implications in our experiment in that lasers must be re-tuned significantly in order to laser cool the different isotopes of barium. We therefore review the two types of isotope shifts, the mass shift and the volume shift, in order to get a sense of the size of these shifts in barium.

2.6.1 Mass Shift

In the Bohr model of a single-electron atom the energy of a transition between two atomic orbitals is proportional to the reduced mass of the nucleus and the electrons

$$E = E_\infty \frac{M_N}{m_e + M_N}$$

where E_∞ is the theoretical energy of the transition in an atom with an infinitely massive nucleus. Assuming that the mass of a neutron is the same as the mass of a proton it can be shown that the mass shift of a transition in an isotope with A nucleons relative to the same transition in an isotope with A' nucleons is approximately

$$\Delta\nu_{mass} \approx \frac{m_e}{M_P}\frac{\Delta A}{AA'}\nu_\infty$$

where M_p is the mass of the proton and ν_∞ is the theoretical frequency of the same level if the nucleus were infinitely heavy.

2.6.2 Volume Shift

The wavefunction of electrons in s-orbitals do not go to zero at the origin. These electrons are sensitive to small changes in volume of the nucleus. When one level of an atomic transition is an s-orbital the energy of the transition depends on the volume of the nucleus. The frequency difference between a transition in an isotope with A nucleons and an isotope with A' resulting from the volume shift can be shown to be approximately

$$\Delta\nu_{vol} \approx \frac{\langle r_N^2 \rangle}{a_0^2}\frac{\Delta A}{A}\frac{Z^2}{(n^*)^3}\nu_\infty$$

where n^* is the effective principal quantum number of the orbital which accounts for the fact that electrons in s-orbitals with a large principal quantum numbers are less likely to be

found at the origin. Z is the number of protons in the nucleus, a_0 is the Bohr radius, and r_N radius of the nucleus. Electron orbitals with non-zero angular momentum also experience a volume shift but the effect is much smaller. The sign of this shift depends on whether the s-orbital is the upper or lower energy level in the transition.

The measured isotope shifts for relevant transitions between $^{137}Ba^{+}$ and $^{138}Ba^{+}$ are listed in table 2.1. As expected the isotope shifts for transitions containing an s state have significantly higher values.

Transition	λ (nm)	$\delta^{137-138}$ (MHz)	Reference
$6S_{1/2} \leftrightarrow 6P_{1/2}$	493.4	271.1(1.7)	[67]
$6S_{1/2} \leftrightarrow 6P_{3/2}$	455.4	279.0(2.6)	[67]
$5D_{3/2} \leftrightarrow 6P_{1/2}$	649.7	13.0(0.4)	[66]
$5D_{3/2} \leftrightarrow 6P_{3/2}$	585.4	5.3(0.5)	[66]
$5D_{5/2} \leftrightarrow 6P_{3/2}$	614.2	2.3(0.4)	[66]

Table 2.1: Measured isotope shifts between $^{137}Ba^{+}$ and $^{138}Ba^{+}$.

Chapter 3

ION TRAPPING

For this work we used a linear Paul trap to confine a single barium ion. In this chapter we review the theory underlying the operation of this type of trap [6].

A linear Paul trap consists of four rod electrodes and two needle electrodes as shown in figure 3.1. An oscillating RF voltage is applied to one pair of opposing rod electrodes while the other pair is grounded. Together, the rod electrodes create an oscillating electric quadrupole potential in the x-y plane along the trap axis:

$$V(x,y,t) = V_0 \left(1 + \frac{x^2 - y^2}{R^2}\right) \cos(\Omega t) \tag{3.1}$$

where R is the distance between the trap axis and one of the rod electrodes and Ω is the frequency of the oscillating voltage applied to the trap electrodes. A DC voltage is applied to the needle electrodes to provide confinement in the $\hat{z}$ direction. At the trap center the DC potential can be approximated as

$$U(x,y,z) = \frac{\kappa U_0}{Z_0^2} \left(z^2 - \frac{1}{2}\left(x^2 - y^2\right)\right) \tag{3.2}$$

where Z_0 is the distance from the tip of one needle electrode to the trap center and κ is a geometrical factor. Taking the gradient of the sum of these potentials we find that the electric field at the trap center is

$$\begin{aligned} \vec{E}(x,y,z,t) &= -\nabla \left[U(x,y,z) + V(x,y,t)\right] \\ &= -V_0 \frac{x\hat{x} - y\hat{y}}{R^2} \cos(\Omega t) - \frac{\kappa U_0}{Z_0^2} \left(2z\hat{z} - x\hat{x} - y\hat{y}\right) \end{aligned} \tag{3.3}$$

The equations of motion for a particle with charge Q in this electric field is determined by the following differential equations.

$$\ddot{u}_i + \left[a_i - 2q_i \cos(\Omega t)\right] \frac{\Omega^2}{4} u_i = 0 \tag{3.4}$$

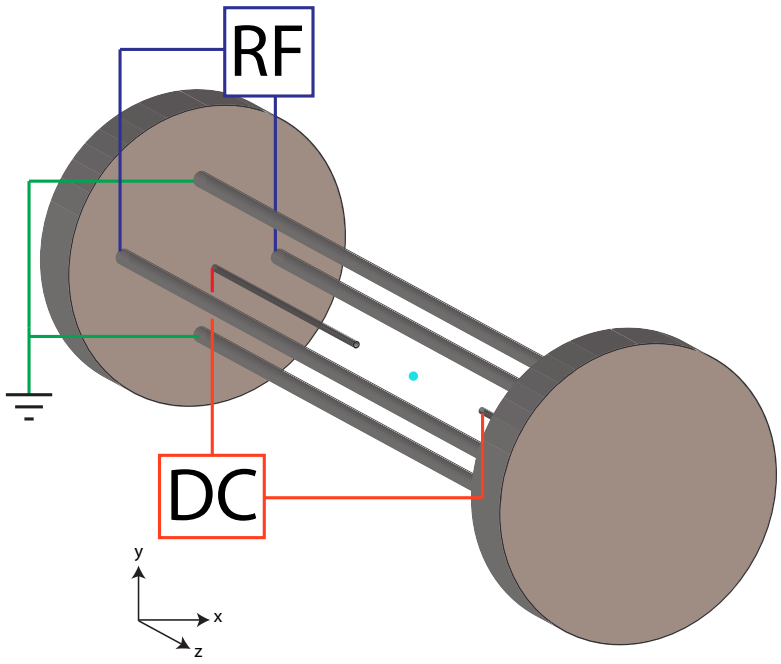

Figure 3.1: A schematic of the electrical connections to a linear Paul trap.

where i=x, y, or z and

$$a_x = a_y = -\frac{1}{2}a_z = \frac{4Q\kappa U_0}{mZ_0^2\Omega^2}$$

and

$$q_x = -q_y = \frac{2QV_0}{mR^2\Omega^2}$$

$$q_z = 0$$

Floquet's theorem states that a differential equation of this form has a complex solution of the form [23]

$$F(a, w, \tau) = e^{i\tau\mu}P(a, q, \tau) \tag{3.5}$$

where P is a complex π periodic function and μ is known as the 'characteristic Mathieu exponent'. For any Floquet solution $F(a_x, q_x, \tau)$ we can form two real valued functions

$$C(a, q, x) = \frac{F(a, q, x) + F(a, q, -x)}{2F(a, q, 0)}$$

$$S(a, q, x) = \frac{F(a, q, x) - F(a, q, -x)}{2F(a, q, 0)}$$

which describe the motion of the the trapped ion in the $\hat{x}$ direction. We can find similar solutions in the $\hat{y}$ direction. When we set the DC end cap voltage, RF amplitude, and frequency applied to the trap electrodes we determine the values for $a_{x,y}$ and $q_{x,y}$. However only values of $a_{x,y}$ and $q_{x,y}$ that lead to real values for μ in the equations of motion in both the $\hat{x}$ and $\hat{y}$ directions will produce stable ion trajectories. Figures 3.2(a) and 3.2(b) show the regions of the $a_{x,y}$-$q_{x,y}$ parameter space that produce real values for μ.

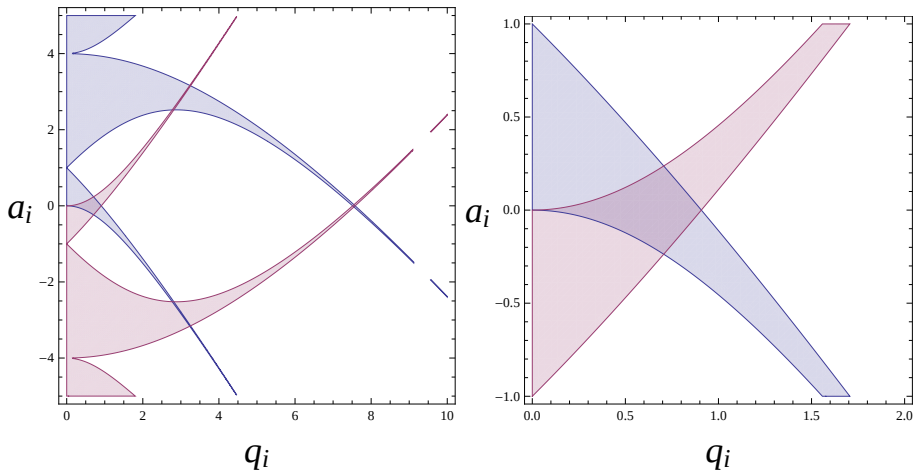

Figure 3.2: A plot of the region in the two dimensional a-q parameter space that allows for stable ion trajectories in both the x and y dimensions. Stable ion trajectories result from setting the RF frequency and amplitude and DC end cap voltages so that a_x, a_y, q_x, and q_y lie in the region of overlap.

If we choose values for U_0, V_0, and Ω that place a_x and q_x, a_y, and q_y in the region shown in 3.2(b) and plot the ion's trajectory in the x-y plane by numerically solving equation 3.4 we see that while the ion is not motionless, it does indeed follow a stable trajectory (figure 3.3).

The ion's motion is comprised of two components.

(a) Harmonic motion at the resonant frequency of the harmonic well created by the oscillating voltage on the trap electrodes. This is known as secular motion.

(b) Driven oscillatory motion at the frequency of the oscillating voltage Ω applied to the

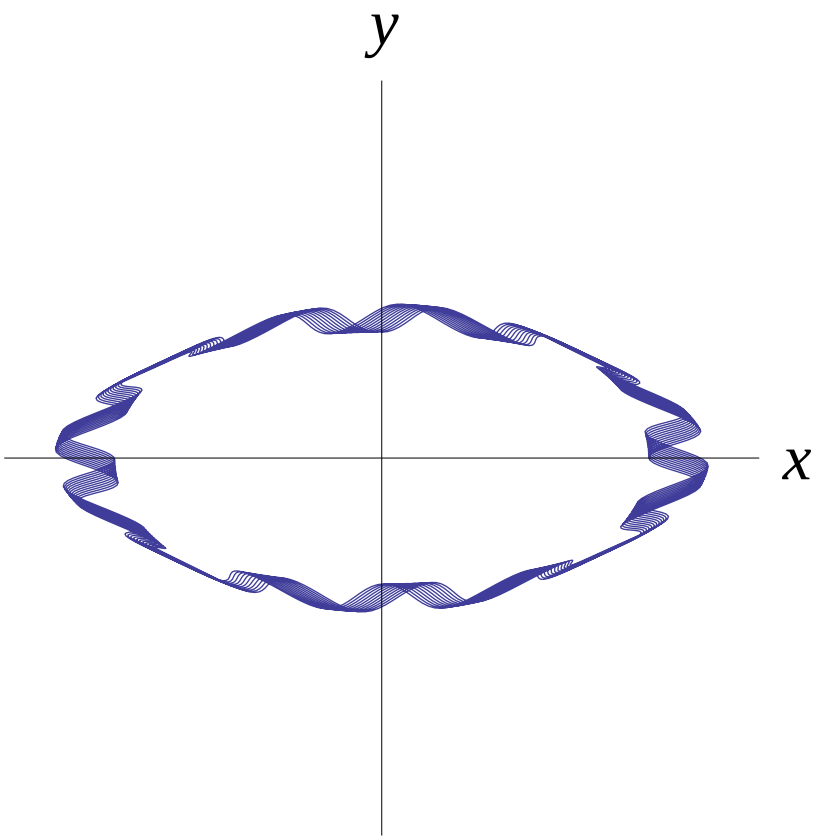

Figure 3.3: A plot of a stable ion trajectory for a particular choice of trap parameters. Secular motion and micromotion can be seen.

trap electrodes. This is typically at a much higher frequency compared to the secular frequency and is known as micromotion.

The secular component of this motion can be reduced through laser cooling (see section 4.2). Micromotion results from the interaction between the ion and a non-zero oscillating electric field in the trapping region. In an ideal trap the electric field at the trap center goes to zero. However even in an ideal trap an ion cooled to its motional ground state would still exhibit some amount of micromotion. The reason is that even in its motional ground state the ion still makes small excursions away from the trap center and into regions where the oscillating electric field is non-zero. If the ion is not cooled to the motional ground state the effect of micromotion will be much greater.

Stray DC electric fields present in the trapping region shift the ion away from the trap center where the oscillating field vanishes. Such stray fields can dramatically increase the micromotion of an ion. We can model the effect of such fields with the addition of another term to eq. 3.4.

$$\ddot{u}_i + \left[a_i - 2q_i \cos\left(\Omega t\right)\right] \frac{\Omega^2}{4} u_i = \frac{e\vec{E}_{DC} \cdot u_i}{m} \tag{3.6}$$

The effect of this additional term can be seen clearly if we choose a reasonable value for $\vec{E}_{DC}$ and solve this equation numerically. A plot of the resulting ion motion under these conditions is shown in figure 3.4.

Micromotion introduced as a result of stray DC electric fields is known as excess micromotion to distinguish it from micromotion that can be reduced through better laser cooling. Excess micromotion can be a serious systematic problem for precision measurements on a trapped ion. In section 4.6 we demonstrate our implementation of a method for canceling stray DC fields inside a quadrupole ion trap.

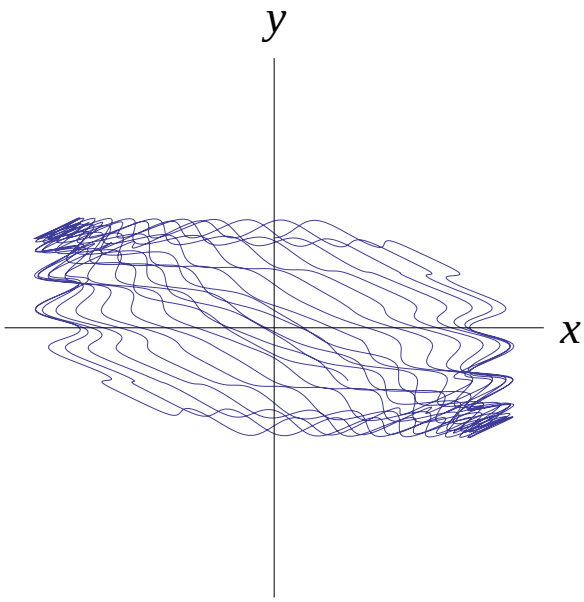

Figure 3.4: Stray electric fields can increase the micromotion of a trapped ion dramatically. Compare to figure 3.3.

Chapter 4

APPARATUS

Atomic physics experiments are often described as 'table top'. However, that term may understate the scale of the apparatus necessary for this type of research. The equipment used for the work described in this thesis is spread out over several 4 foot by 10 foot optics tables in three different rooms in the basement of the Physics and Astronomy Building at the University of Washington. Here we described the important components of the apparatus.

4.1 Linear Quadrupole Ion Trap and Vacuum System

The ion trap and vacuum system used for this work was constructed by Gang Shu as part of his thesis work [60]. It incorporates a spherical mirror which allows for the efficient capture of ion florescence, although this feature was not used for the work described here.

The trap is enclosed in a vacuum chamber with eight 1-1/3 inch side access viewports and one 4 inch viewport on the top. Four of the side ports are used for electrical feedthroughs. The bottom port is blanked off. The remaining four side ports and the larger top port are sealed with fused silica viewports which provide optical access.

The chamber is held under vacuum by a 20 liter per second ion pump and a titanium sublimation pump. An ion gauge is used to monitor the pressure of the entire vacuum system. Except during loading, we are able to maintain pressures of approximately 1×10^{-10} torr.

Our trap RF is generated by an RF oscillator operating at 22 MHz. We send this signal through a variable attenuator for convenient amplitude control then amplify it to 3-5 W. The signal is then fed into a quarter-wave copper helical resonator with a Q factor of several hundred. The resonator is connected to one set of opposing trap rods. The other set is held at ground potential. The needle end cap electrodes are held at a constant DC voltage typically on the order of 10-50 V. We have the ability to apply an independent biasing DC

voltage to each of the trap rods as well as discussed in section 4.6.

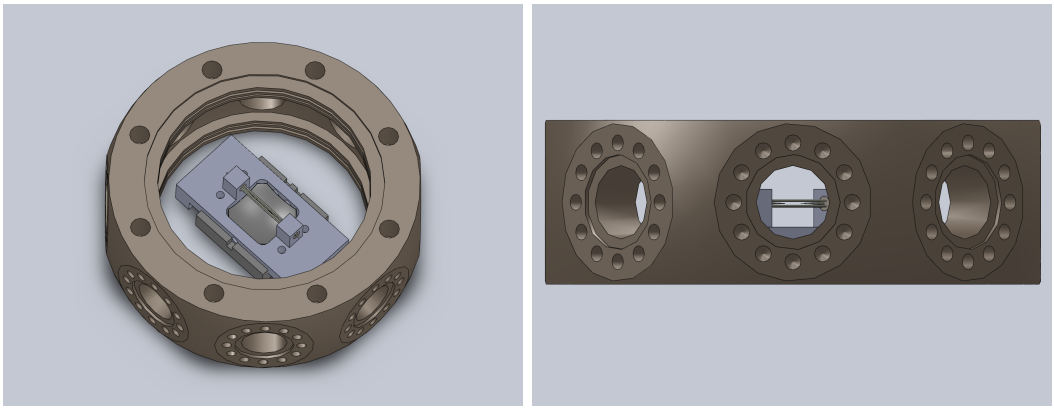

(a) perspective (b) side

Figure 4.1: Drawings of the vacuum chamber and linear quadrupole ion trap. The chamber is evacuated and maintained at a pressure of 10^{-10} torr.

To load barium ions into the trap we run about one amp of current through an oven consisting of a ceramic tube wrapped with a length of tungsten wire. The tube contains a small sample of barium metal and is aligned with the trap center. When the oven gets hot individual barium atoms are emitted toward the trapping region.

A UV lamp positioned outside the vacuum chamber is pulsed at approximately 10 Hz. It is not clear whether the ionization occurs through direct photo-ionization or whether the UV light is creating photoelectrons (perhaps from the trap rods) which then ionize the barium atoms after collision [63]. In any case it rarely takes longer to than ten minutes for us to load a single ^{138}Ba ion.

A pair of coils approximately three inches in diameter generate a magnetic field which serves as a quantization axis for the ion. Running 2.4 amps through the coils generates a magnetic field of approximately 3 gauss. A secondary 'trim' coil is used to cancel the vertical component of the Earth's magnetic field. We set the current in this coil by observing the ion fluorescence from a ^{138}Ba ion cooled with circularly polarized 493 nm light traveling roughly parallel to the axis of quantization. When the laboratory field is perfectly aligned with the laser beam the ion is optically pumped into a single Zeeman state and the photon

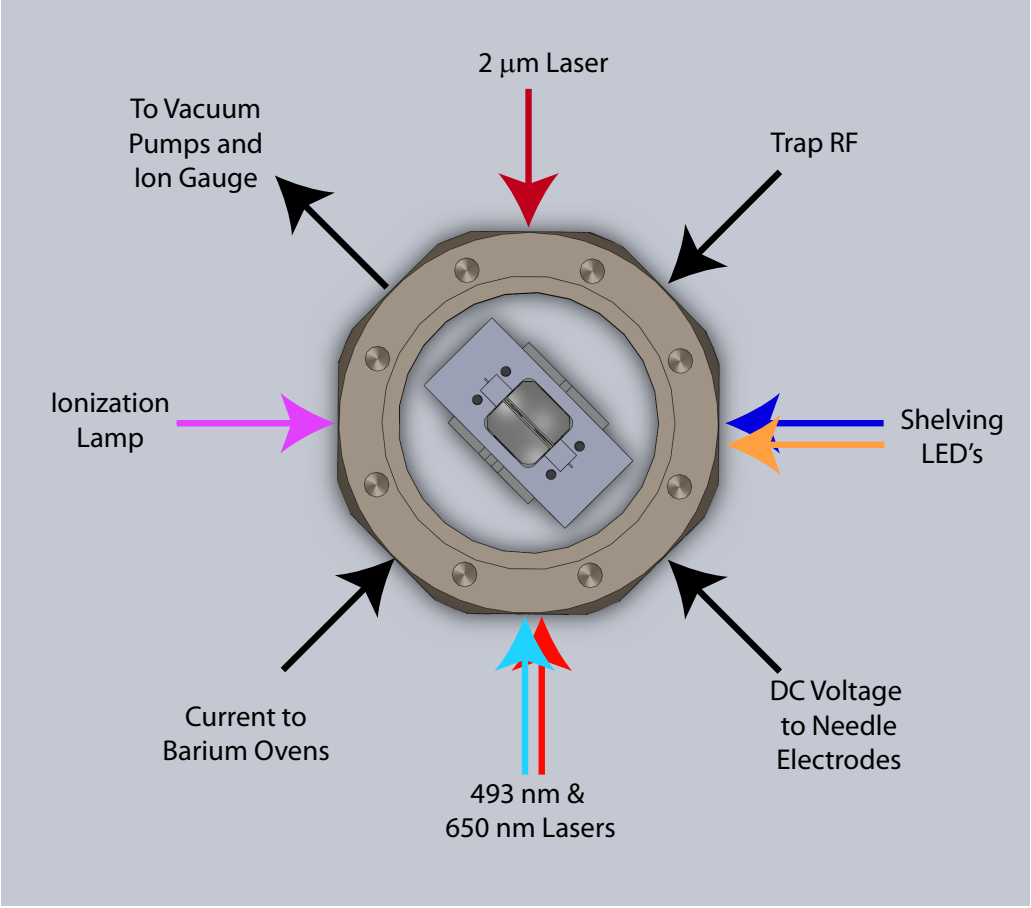

Figure 4.2: Optical access to the ion trap is available via four side view ports and one larger top view port. Three of the remaining four side ports are used for electrical feedthroughs. The last port is connected to the vacuum pumps.

counts detected by the PMT go to zero.

4.2 The Cooling Lasers

Figure 4.3 shows a schematic of system used to deliver 493 nm and 650 nm laser light to the ion. An ECDL generates about 5 mW of 650 nm light which is passed through a AOM with a center frequency of 80 MHz to allow for fast shuttering of the beam. Generating 493 nm laser light is significantly more complicated. The 493 nm light used in our experiment originates from a 20 mW, 986 nm ECDL DL-Pro manufactured by Toptica. The output of this laser is used to seed a tapered amplifier which provides us with ∼200 mW of 986 nm light. The beam from the tapered amplifier is shaped using two lenses and coupled into a bow-tie enhancement cavity formed by two flat mirrors and two curved mirrors. One of the flat mirrors is an input coupler with a reflectivity of ∼95% the other mirrors are coated for high reflectivity at 986 nm.

Once inside the cavity the beam comes to a waist at two different locations; a larger waist located halfway between the flat mirrors and a tight waist located halfway between the curved mirrors. At this tighter waist we place a Brewster cut potassium niobate crystal mounted inside a copper block whose temperature is controlled with a thermo-electric cooler. The temperature of the crystal is chosen to achieve non-critical phase matching for SHG at 986 nm. The position of one of the flat mirrors (not the input coupler) is controlled using a piezo-electric transducer (PZT). The cavity is locked using the Hansch-Couillaud polarization scheme [32]. With this setup we are able to generate several milliwatts of 493 nm light.

The combination of the 493 nm and 650 nm lasers causes a trapped barium ion to rapidly oscillate between the $6S_{1/2}$, $6P_{1/2}$, and $5D_{3/2}$ levels. When the ion spontaneously decays from the $6P_{1/2}$ to the $6S_{1/2}$ level it emits a 493 nm photon in a random direction. With the cooling lasers on this occurs quite frequently as the natural lifetime of the $6P_{3/2}$ level is on the order of 8 ns which much faster than the rate at which we can drive the 493 nm and 650 nm transitions.

The motion of a trapped barium ion can be greatly reduced by detuning the 493 nm and 650 nm lasers approximately ten megahertz from the center frequency of their respective

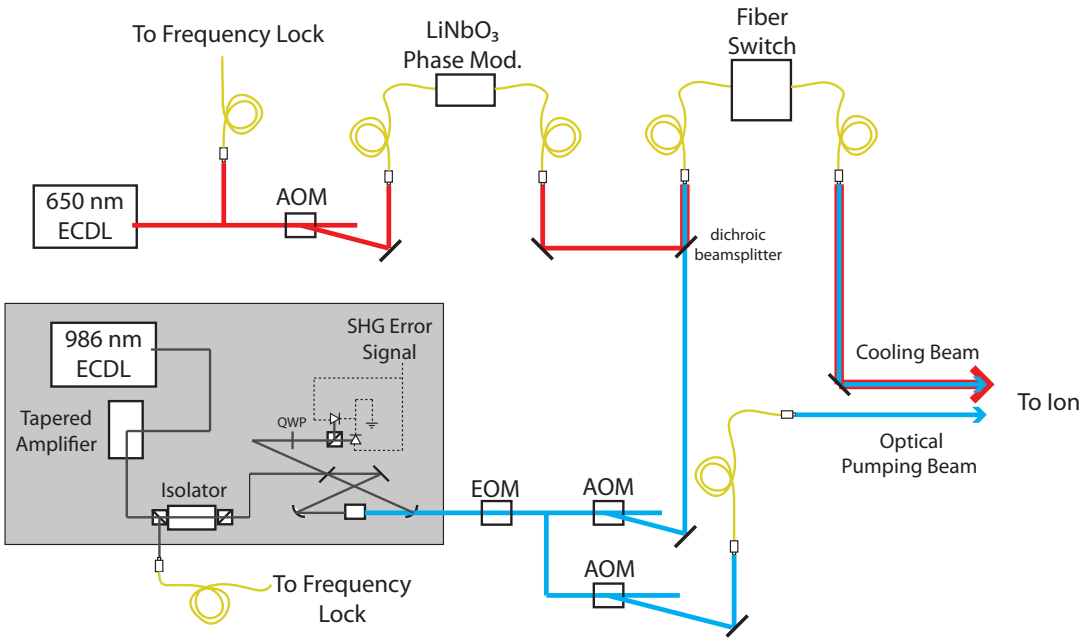

Figure 4.3: A schematic of the 493 nm and 650 nm laser systems. Light from a 986 nm ECDL is frequency doubled and combined with the light from a 650 nm ECDL then focused on a trapped barium ion. A small amount of the 493 nm beam is split off. Its polarization is set to allow of optical pumping into the $6S_{1/2}$ level.

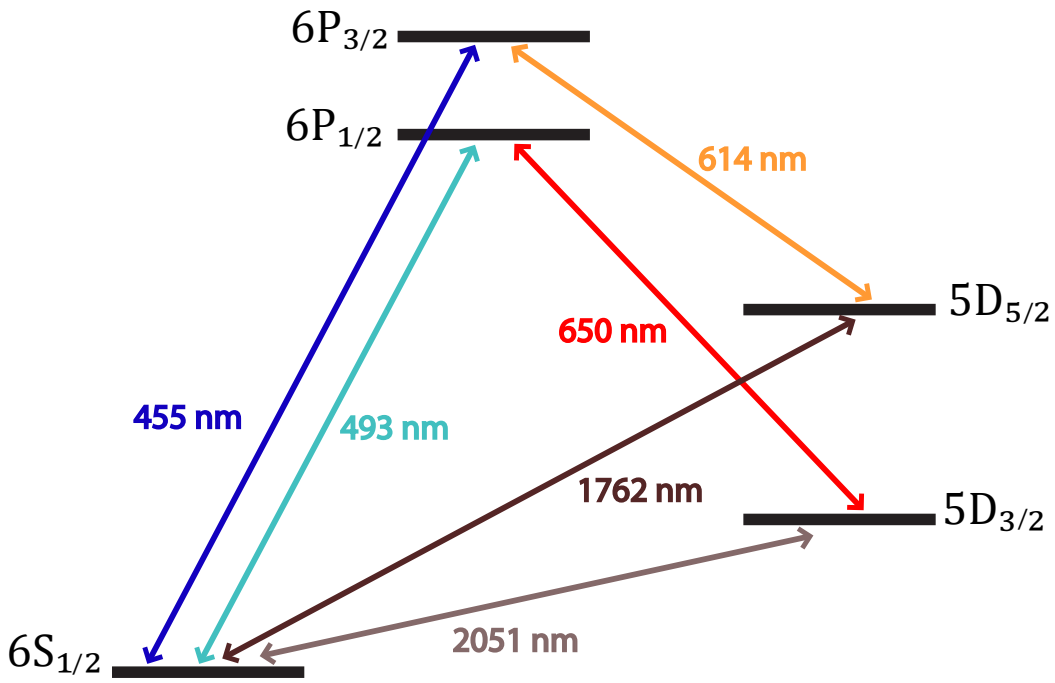

Figure 4.4: A diagram of the the energy levels in ^{138}Ba with the atomic transitions used in this work labeled.

transitions. If a laser is tuned to the red of an atomic transition an atom at rest in the lab frame will not interact strongly with the laser. However if the atoms velocity vector has a component that is anti-parallel to the laser beam, in the atom's frame of reference, the laser beam will appear Doppler shifted to a higher frequency. This shifts the frequency of the detuned laser closer to the center frequency of the atomic transition. It is therefore more likely for the ion to absorb a photon when it is moving in a direction opposite direction of propagation of the laser beam than when it is traveling parallel to the beam. The momentum transfered to the ion by the absorbed photons tends to reduce the motion of the ion. Of course when the atom transitions from the excited state back to the lower energy level it will emit a photon with the same energy and momentum. However this photon will be emitted in a random direction and after many such transitions the effect of these photons will average to zero.

The cooling lasers also provide our primary means of detecting a trapped barium ion. A high numerical aperture microscope objective (NA=.28) located outside the vacuum chamber is positioned approximately 30 mm from the center of the trap. The collected light is refocused, spatially filtered with a pinhole, then spectrally filtered using an interference filter that passes 493 nm light and blocks 650 nm light. We use a motorized flipper mirror to divert the collected light to either a photo-multiplier tube or a CCD camera. Images of a single ion and a pair of taken with the CCD camera are shown in figure 4.5.

Before reaching the ion the 493 nm light and the 650 nm light each pass through an AOM to allow for fast shuttering. During the course of this work we discovered that a small amount of light ($\sim$1 nW) was leaking through these AOM's while they were in the 'off' state. This leakage light would randomize the state of the ion and completely wash out the spectroscopic features of interest. The solution we settled on was to pass both the 493 nm light and the 650 nm light through a fiber switch. The switch allows us to attenuate the AOM leakage light by an additional 30 dB. This proved sufficient for our purposes.

(a) A single ^{138}Ba ion (b) Two ^{138}Ba ions

Figure 4.5: Trapped ions are imaged using a CCD camera. The imaging system provides enough resolution to clearly resolve individual ions.

4.2.1 Frequency Stabilization

The 986 nm laser and the 650 nm laser are frequency stabilized using nearly identical schemes. A small amount of power from each laser is picked off and fiber coupled to a separate optics table. The light is shifted by a double-passed AOM then coupled into a Fabry-Perot reference cavity consisting of two curved mirrors HR coated for the appropriate wavelength. The finesse of the 650 nm cavity was measured to be approximately 150 while the finesse of the 986 nm cavity is approximately 1000. In each cavity the mirrors are separated by a Zerodur spacer which gives a free spectral range of approximately 500 MHz. We found that the Zerodur spacers had sufficient temperature stability to not require additional stabilization. The AOM's used to shift the frequency have a tuning range of about 100 MHz which was sufficient to allow for continuous tuning over the necessary frequencies. Photodetectors monitor the transmission of light through the Fabry-Perot cavities and a side of the fringe locking scheme is employed to feedback to the tuning piezos in the laser heads. A locking circuit designed and built by previous graduate students for locking enhancement cavities was used to integrate and amplify the error signal. A diagram of this

circuit is shown in Appendix B.

Because the 986 nm cavity has such narrow transmission lines we found it difficult to achieve a robust frequency lock to the cavity when sending the feedback signal exclusively to the tuning PZT inside the laser head. Evidently the laser frequency fluctuates significantly at frequencies beyond the 5-10 kHz bandwidth typical of tuning PZT's. These uncorrected fluctuations were enough to jerk the laser away from the frequency of the cavity mode. However by sending the voltage output of the photodetector through a variable resistor and into the laser diode current modulation input on the laser head we were able to greatly enhance the bandwidth of our frequency lock. This provided us with a second feedback channel to control the laser frequency. Since this channel does not pass through an integrator nor driving a capacitive load, the bandwidth of this channel extends well into the megahertz range. The combination low bandwidth integrated feedback sent to the PZT combined with high bandwidth feedback sent used to modulate the laser diode current allowed for a solid lock.

4.2.2 Electro-Optic Modulators for Laser Cooling ^{137}Ba

As shown in section 2.1.3 the hyperfine interaction splits the fine structure levels into hyperfine sublevels. The ^{137}Ba nucleus possesses angular momentum I=3/2. Creating a cycling transition in ^{137}Ba that is suitable for laser cooling requires simultaneously addressing all the hyperfine sublevels in the $6S_{1/2}$ and $5D_{3/2}$ states. However the separation of these sublevels is much greater than the linewidth of our 493 nm or 650 nm lasers. By passing the 493 nm and 650 nm beams through electro-optic phase modulators before sending them to the ion we can add sidebands to the spectrum of frequencies contained in the laser beams. We can set the modulation frequencies such that the combination of the 493 nm and 650 nm carrier frequencies and their respective sidebands address all the necessary hyperfine sublevels.

Calculated spectra of both the 493 nm and 650 nm transitions are shown in figure 4.6. We have assumed a Lorentzian lineshape for each transition with a linewidth determined by the $\sim 8ns$ lifetime of the $6P_{1/2}$ level. The amplitudes of the peaks are proportional to

the square of the electric dipole matrix element connecting the two states which can be calculated using a formula in [43] that gives the E1 matrix element in terms of two 6-J symbols and Clebsch-Gordan coefficients.

$$\begin{aligned}\left\langle L'S'J'IF'm'_f\right| er \left|LS'JIFm_f\right\rangle = e(-1)^{1+L'+S+J+J'+I-m'_F} \left\langle \alpha'L'\right| |r| \left|\alpha L\right\rangle \\ \times \sqrt{(2J+1)(2J'+1)(2F+1)(2F'+1)} \\ \times \left\{ \begin{array}{ccc} L' & J' & S \\ J & L & 1 \end{array} \right\} \left\{ \begin{array}{ccc} J' & F' & I \\ F & J & 1 \end{array} \right\} \left(\begin{array}{ccc} F & I & F' \\ m_F & q & -m'_F \end{array} \right) \end{aligned} \quad (4.1)$$

We use a resonant phase modulator operating at 4.025 GHz to place sidebands on our 493 nm laser beam. This allows us to address either the $F = 1 \leftrightarrow F = 1$ and $F = 1 \leftrightarrow F = 2$ transitions or the $F = 2 \leftrightarrow F = 1$ and $F = 2 \leftrightarrow F = 2$ transitions. We use the latter set of transitions for two reason. First we wish to avoid the $F = 1 \leftrightarrow F = 1$ transition which is 1/5 the strength of the other three transitions. Second, this set of sidebands allows us to optically pump into the $F = 2$ $m_F = 0$ which is the lower level of our proposed clock transition.

Since we are using a modulation frequency that is half of the frequency interval separating the states we are addressing the carrier frequency is not resonant with any atomic transition. In fact the closest transition lies over 2 GHz away. This can be used to our advantage. Turning off the modulation RF with an RF switch effectively shutters the 493 nm beam to the ion and provides additional attenuation to the light driving the the 493 nm transition when needed.

Addressing the four hyperfine sublevels of the $5D_{3/2}$ state requires a more complicated sideband scheme. The spectrum of the $5D_{3/2} \leftrightarrow 6P_{1/2}$ transition is shown in figure 4.6(b). We use a fiber coupled lithium niobate phase modulator to place multiple sidebands on our 650 nm beam. There is significant overlap among the transition lines so the choice of the modulation frequencies is not critical for this transition. In a sense this is unfortunate. If we were able to address the $F = 1$, $F = 2$, and $F = 3$ levels but not the $F = 0$ sublevel we would be able to optically pump into a well defined state in the $5D_{3/2}$ level ($F = 0$, $m_F = 0$) without the need for an separate optical pumping beam. Furthermore the $F = 0$, $m_F = 0$ state happens to be the upper level of our proposed clock transition. We could the

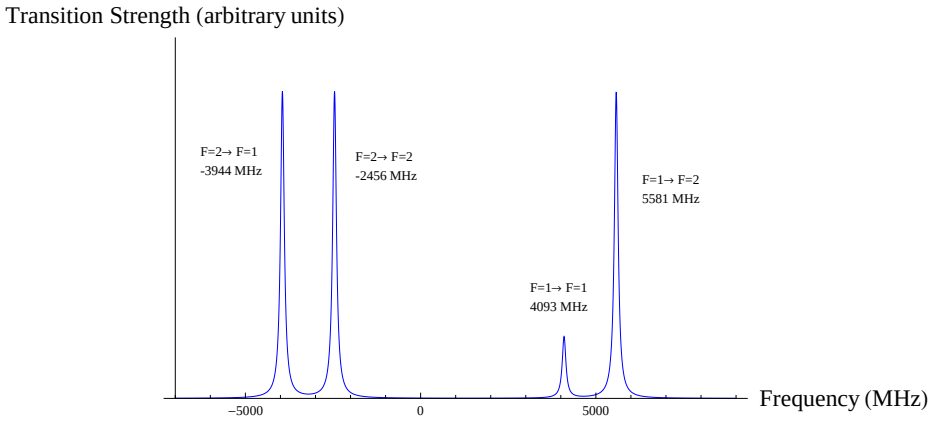

(a) Blue

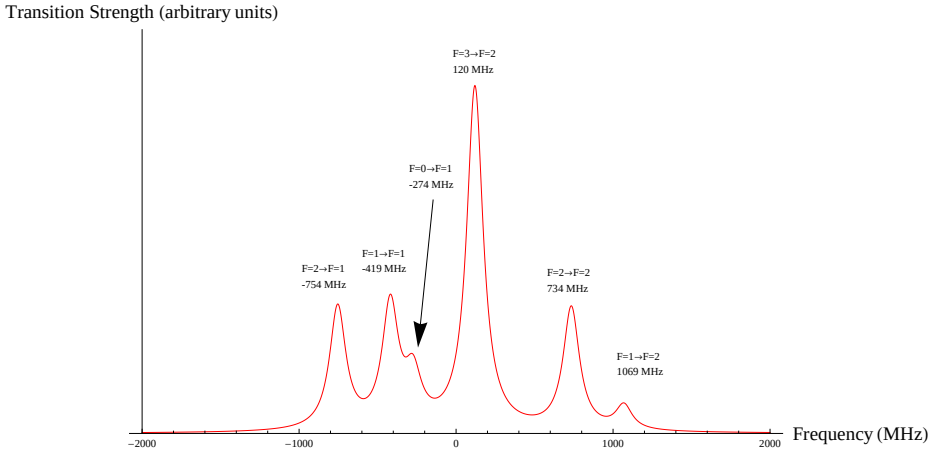

(b) Red

Figure 4.6: Calculated Lorentzian lineshapes for the spectrum of a ^{137}Ba ion in the 493 nm and 650 nm wavelength regions. Hyperfine splittings intervals are taken from the literature [17]. A lifetime of 8 ns was assumed for the $6P_{1/2}$ level.

drive the clock transition from the $5D_{3/2}$ to the $6S_{1/2}$ level.

4.2.3 Optical Pumping System

In order to consistently drive the $6S_{1/2} \leftrightarrow 5D_{3/2}$ transition it is necessary to initialize the ion into a well defined state in the $6S_{1/2}$ level. To achieve this we set up a second 493 nm beam whose polarization and alignment are chosen so that the beam will address all but one Zeeman state in the $6S_{1/2}$ level. A small amount of 493 nm light is picked off from the cooling beam after the 4 GHz phase modulator and sent through an AOM that operates at the same frequency as the AOM on the cooling beam. An AOM is used as a shutter to switch on and off the optical pumping beam. After the AOM the deflected light is coupled into a polarization maintaining fiber to decouple the upstream beam alignment from the alignment with the ion. After exiting the fiber the beam passes through a calcite polarizer to produce linearly polarized light. A quarter waveplate can be placed after the polarizer to produce circularly polarized light an the optical pumping beam can be aligned parallel or perpendicular to the quantization axis. This optical pumping beam combined with the 650 nm laser allows us to realize all of the optical pumping schemes shown in figures 2.12 and 2.13.

4.3 2051 nm Laser System

To drive the 2051 nm $6S_{1/2}$ to 5D1/2 transition in Ba^+ we use a commercially manufactured diode pumped solid state Tm,Ho:YLF laser . A laser diode with a center wavelength of 780 nm pumps a yttrium lithium fluoride (YLF) crystal doped with thulium and holmium atoms. When a thulium atom absorbs a photon from the pump laser it is excited to the $^3F_4$ orbital. Through a 'cross-relaxation' process the excited thulium atom decays to the $^3H_4$ while simultaneously exciting a second thulium to the $^3H_4$ state. The excited thulium atoms interact with holmium atoms and excite them to the $^5I_7$ orbital. Finally lasing occurs on the $^5I_7$ to $^5I_8$ transition in Ho [22]. This process is illustrated in figure 4.7.

Coarse tuning of the laser is achieved by adjusting the temperature of the crystal resonator. Fine tuning is achieved by adjusting the length of the lasing cavity by controlling the voltage on a PZT. The manufacturer specifies the free running linewidth of this laser

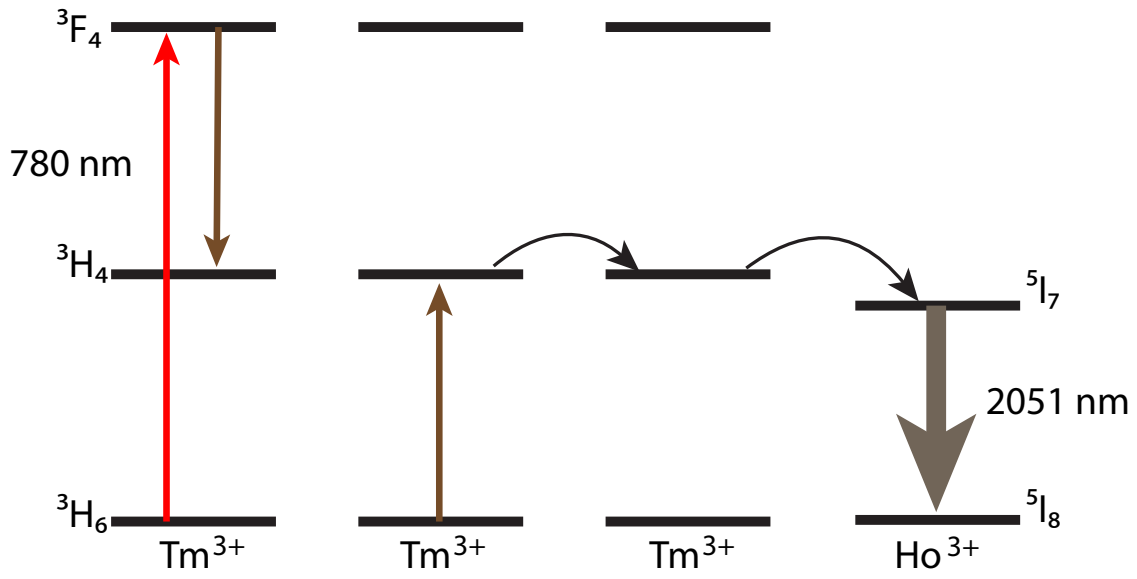

Figure 4.7: The energy levels in a Tm,Ho:YLF crystal involved in the generation of 2051 nm laser light. Reproduced from [22].

to be 10 kHz with a longterm drift rate of less than 1 GHz per twenty-four hour period. A frequency standard referenced to the $6S_{1/2} \leftrightarrow 5D_{3/2}$ transition in barium would require a 2051 nm laser with a sub-hertz linewidth to be competitive with state of the art atomic clocks. To achieve this level of stability it is necessary to reference the frequency of the 2051 nm laser to a stable reference cavity with a narrow linewidth. While reference cavities designed for use at shorter wavelengths routinely have finesses greater than 10^5, optical coating technology limited the finesse of a 2051 nm cavity to around 20,000. The decision was made to frequency double a portion of our 2051 nm light to 1025 nm and implement a frequency stabilization scheme at 1025 nm.

4.3.1 Frequency Doubling 2051 nm Light

Second harmonic generation (SHG) of 1025 um light using a bulk, periodically poled lithium niobate (PPLN) crystal in single pass configuration has been previously demonstrated with

an efficiency of 10% W^{-1} [28]. It was initially assumed that a single pass through a PPLN crystal would generate 10-100 μW of 1025 nm light which would be be enough to lock to the ULE cavity. Frequency doubling light at 2051 nm proved to be more difficult than anticipated. However in single pass configuration we were only able to produce 10's of μW of 1025 nm light. This was deemed insufficient to accomodate losses from a frequency shifting AOM on the 1025 nm beam and still achieve a robust frequency lock.

To boost the conversion efficiency we constructed an enhancement cavity around the crystal. Our PPLN crystal is 4 cm long with nine parallel channels with various poling periods. We use a channel with a poling period of 30.25 μm. The crystal is held inside an oven which maintains a temperature of 108 °C for optimum phase matching. The enhancement cavity consists of two flat mirrors and two curved mirrors each with a radius of curvature of 250 mm arranged in a bow-tie configuration. The curved mirrors are separated by 325 mm and the PPLN crystal is placed at the midpoint where the beam comes to a 153 μm waist. The enhancement cavity is locked to the wavelength of the 2051 nm laser using the Hansch-Couillaud polarization scheme (see section A.1 for a discussion of this method).

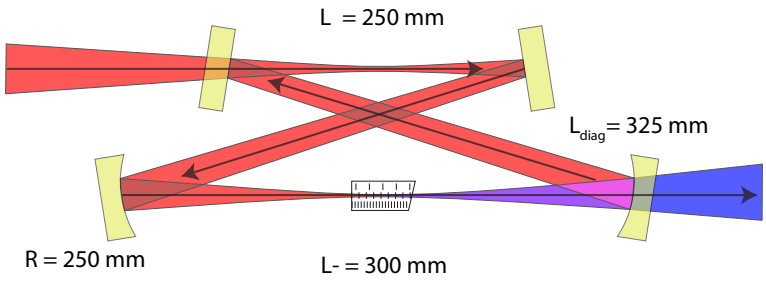

Figure 4.8: A schematic diagram of the enhancement cavity used to increase the efficiency of the 2051 nm to 1025 nm SHG process.

One unusual feature of this enhancement cavity system is that although we are using the Hansch-Couillaud polarization scheme to generate an error signal, the cavity does not contain any polarization dependent elements to ruin the finesse for light of the 'wrong'

linear polarization. Both linear polarizations of 2051 nm are supported in the cavity but due to birefringence in the PPLN, the same cavity mode has a different frequency for each polarization. This leads to a second error signal of opposite sign at the frequency of the other polarization mode shown in figure 4.9.

The PPLN crystal only converts light with vertical polarization so observing the transmission of the cavity with a silicon photodiode shows a single peak. In practice there is a small amount of 2051 nm light at the frequency indicated by the other error signal due to light leaking through the output coupler. However this light has a low intensity and a wavelength that is completely invisible to the silicon photodetectors down stream.

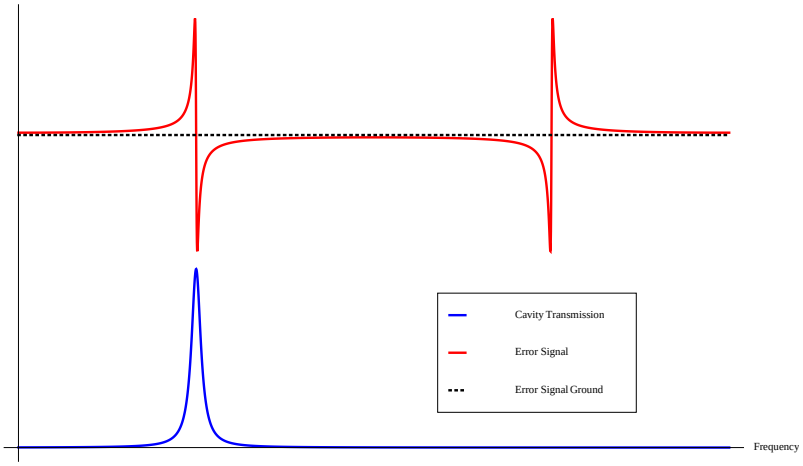

Figure 4.9: A drawing of the unconventional error signal used to lock the 2051 nm enhancement cavity resulting from the absence of any intracavity polarization dependent elements

By choosing suitable mode-matching lenses we were able to achieve cavity coupling efficiencies of 75%. Sending all of the available power from the 2051 nm laser (about 40 mW) directly to the enhancement cavity allowed us to generate 3 mW of 1025 light.

The original PPLN crystal we purchased for 2051 nm SHG was a stock part and the AR coatings on the front and back faces of the crystal were not optimized for 2051 nm wavelength light. When this crystal was placed inside the enhancement cavity these reflections became significant. The crystal acted like an intra-cavity etalon and when the frequency of the

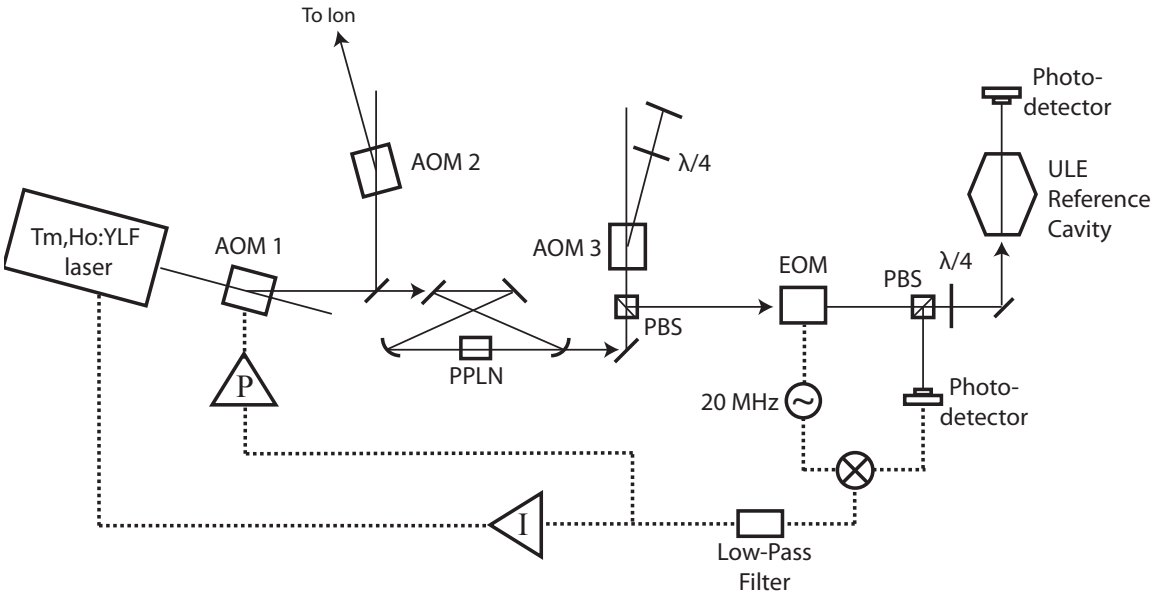

Figure 4.10: A schematic of the frequency stabilized 2051 nm laser system

2051 nm laser was scanned the conversion efficiency fluctuated by 50%. To rememedy this problem we purchased a custom made PPLN crystal AR coated specifically for 2051 nm. In addition the output face of the crystal was polished to be one degree off of parallel. We have not seen any signs of etalon behavoir with the custom PPLN crystal.

After frequency doubling the 1025 nm light is sent through a double passed AOM to allow us to shift the frequency of the 1025 nm light. The beam then passes through an electro-optic phase modulator with a resonant frequency of 20 MHz to generate the frequency sidebands necessary for the Pound-Drever-Hall frequency stabilization scheme (see section 4.3.4).

4.3.2 Ultra-High Finesse Optical Cavity at 1025 nm

The ULE reference cavity is similar of a design developed at JILA [46]. The input mirror of the ULE cavity is flat and the output mirror has a radius of curvature of 500 mm. The mirrors are fixed 77.5 mm apart by a spacer made from ultra-low expansion (ULE) glass. The cavity is mounted vertically to reduce vibrations and is supported by three Teflon posts

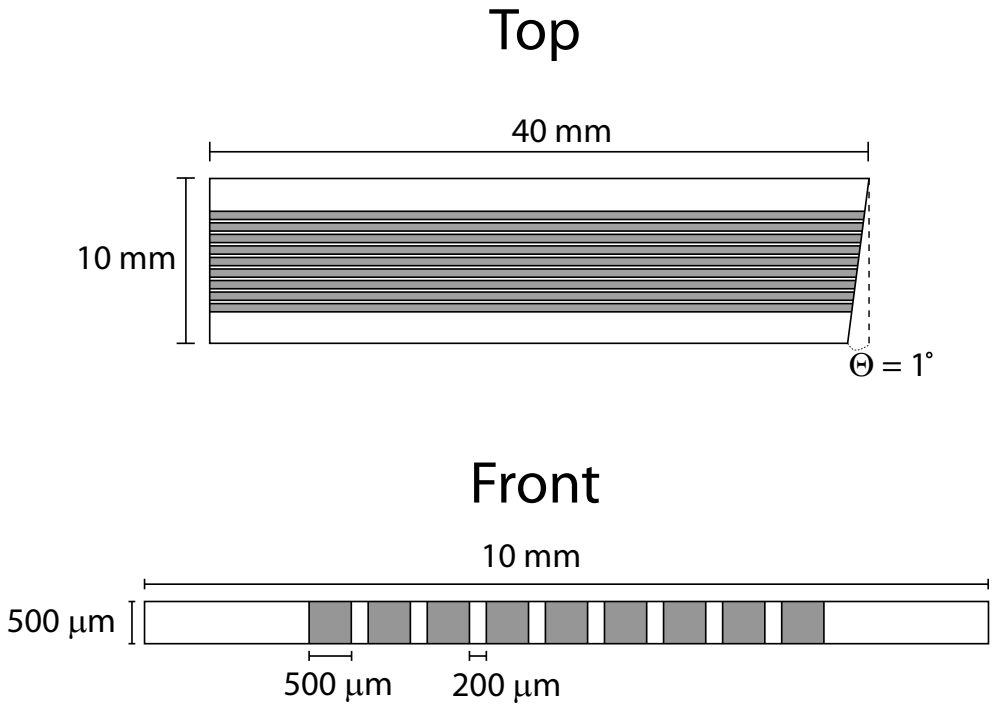

Figure 4.11: A drawing of the poling structure in the PPLN crystal. Scales of top and bottom figure are different.

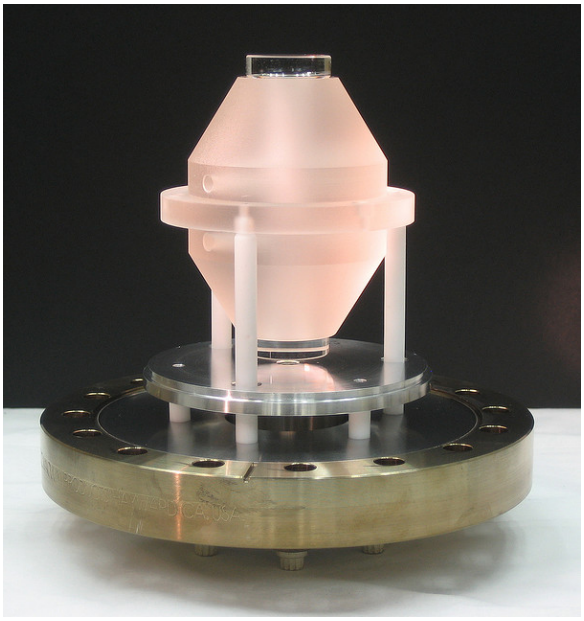

Figure 4.12: A photo of the ULE reference cavity. Cavity finesse has been measured to be 300,000 or greater. Photo credit Jeff Sherman

to minimize thermal conductivity. The mounted cavity is placed in a vacuum chamber which is held at a pressure of 10^{-8} Torr. The the entire system is enclosed inside a temperature stabilized box to further reduce cavity length variations.

Using a formula from [37] we can calculate the mode spectrum for a linear cavity with the mirror separation d, and radi of curvature R_1 and R_2.

$$\frac{\nu}{\nu_0} = (q+1) + \frac{1}{\pi}(m+n+1)\arccos\sqrt{(1+d/R_1)1+d/R_2)} \tag{4.2}$$

where $\nu_0 = \frac{c}{2L}$ is the free spectral range of the cavity (which in our case is 1.935 GH), q denotes a particular longitudinal mode number, and m and n specify the transverse mode. The frequency interval between two transverse modes is approximately 257 MHz. Notice that the modes are m+n+1 fold degenerate. A plot of the predicted spectrum is shown in figure 4.13.

While it is possible to lock the 2051 laser to any of these modes we prefer to lock to a TEM00 mode for two reasons. First, it is significantly easier to mode-match into a TEM00 mode than a higher order transverse mode. We are only able to couple 10% as much light

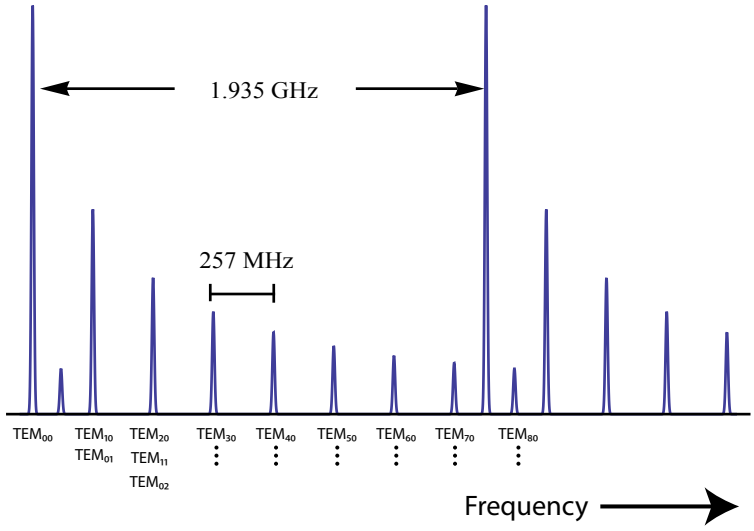

Figure 4.13: The transmission spectrum of the ULE cavity mode calculated from the manufacturer specified mirror curvatures and spacings.

into the TEM10 mode. As a result locking to the TEM00 mode leads to a more robust error signal and greater flexibility when tuning the feedback loop. Second, the higher order transverse modes are not perfectly degenerate. A small frequency splitting among nearly degenerate cavity modes would effectively broaden the linewidth of the cavity mode and lead to a less effective laser frequency lock.

It is necessary to be able to shift the frequency of the light going to the ULE cavity independent of the tuning of the 2051 nm light going to the ion. Ideally one would like to be able to frequency shift the frequency of the beam by the FSR of the reference cavity which is nearly 2 GHz in our case. A similar ULE cavity lock setup at the University of Washington used for an indium ion experiment [64] accomplished this by coupling the light going to the cavity into a waveguide EOM with a 10 GHz modulation bandwidth. The coupling was done in free space to avoid noise added by optical fibers. One of the modulation sidebands was then locked to a TEM00 mode. However free-space coupling into a waveguide modulator is an inefficient process and would be challenging with the 1025 nm

power levels available to us.

The frequency shifting solution we adopted relies on a combination of three frequency shifts to cover the FSR of the ULE cavity.

(a) The double-passed AOM can be driven at frequencies between 150 and 250 MHz. In double-pass configuration this allows us to shift the frequency of the 1025 nm beam by 300-500 MHz.

(b) A 55 MHz AOM used to shutter the 2051 nm light going to the ion can be changed from up-shifting to down-shifting the frequency of the 2051 nm beam adding an additional 200 MHz (at the 1025 nm wavelength) to our available frequency shift.

(c) By increasing the temperature of the ULE cavity from room temperature up to 80 degrees Celsius we are able to shift the frequency of a TEM00 by up to 600 MHz. A plot of the temperature dependence of the frequency of one TEM00 ULE cavity mode is shown in figure 4.14.

The combination of these shifts allows us to cover approximately 1.8 GHz out of the 1.935 GHz cavity FSR. This scheme has allowed us to lock the 2051 nm at all of the frequencies we have required so far but the scheme is less than ideal. Modifications may be required for future experiments.

4.3.3 Diagnosing Poor Cavity Performance

When the cavity was delivered to us from the manufacturer our initial attempts at coupling the 2051 nm laser to the ULE reference cavity were only marginally successful. Despite our best efforts at matching the spatial mode of the input beam to the lowest order cavity mode we were only able to observe a transmitted signal that was approximately .02% the intensity of the incident light. This resulted in an error signal that was only barely resolved above the noise floor and a very touchy lock. Here we recount the saga of how we diagnosed this poor performance.

Cavity ring down measurements are a simple way of characterizing the performance of an optical resonator. To perform this type of measurement resonant light is coupled

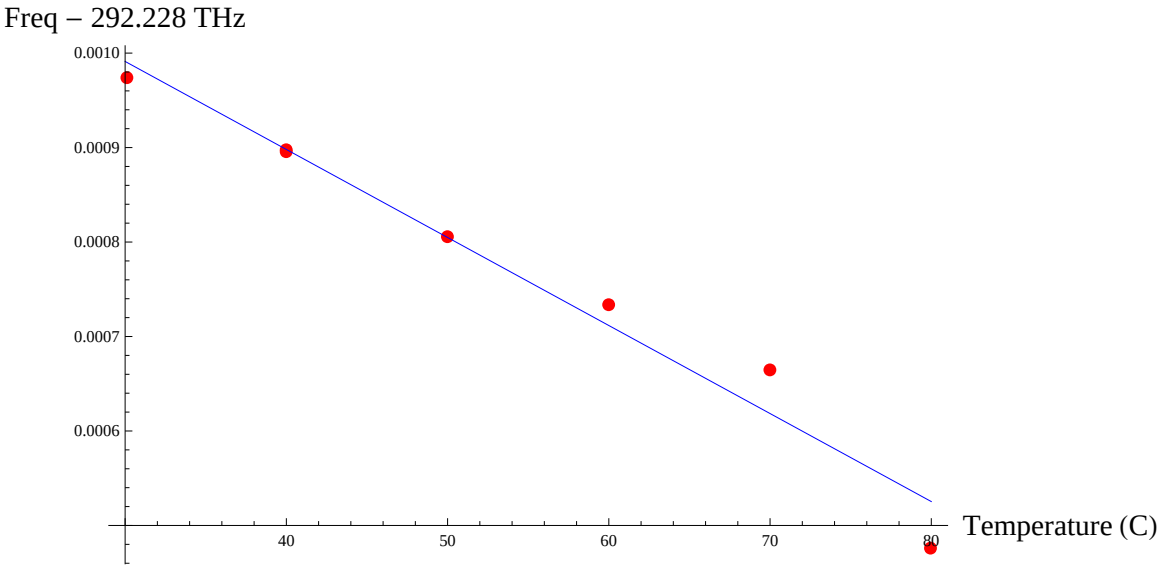

Figure 4.14: A plot of the frequency of a TEM00 mode of the ULE cavity as a function of temperature. Changing the temperature of the ULE cavity allows for broad tuning of the frequency stabilized 2051 nm laser.

into an optical cavity and the transmission through the cavity is monitored with a fast photodetector. The light is then switched off abruptly and the transmitted signal decays exponentially as the light built up in the cavity leaks out. The intensity of the light leaving the cavity is given by

$$I = I_0 e^{-t/\tau}$$

with a time constant

$$\tau = \frac{1}{c}\frac{l}{1-R}$$

where l is the cavity length, and R is the cavity mirror reflectivity.

It was necessary to perform a ring down measurement in order to diagnose to cause of our poor coupling into the ULE. However with approximately 2 mW of 1025 nm light at our disposal it was difficult to find a photodetector that had the bandwidth necessary to see the ∼2 microsecond decay of the transmitted light as well as enough gain to resolve the signal above the noise floor. To solve this problem we used the light from the 2051 nm to 1025 nm doubling cavity to injection lock a 1025 nm Fabry-Perot laser diode. This provided

us with approximately 30 mW of 1025 nm light. We directed this absurdly large amount of optical power at the ULE cavity and carried the carried out the ring down measurement. We used an AOM to shutter the amplified 1025 nm beam and we captured the decay of the cavity transmission signal using a fast photo-detector and a digitizing oscilloscope. The data along with the best fit exponential are shown in figure 4.3.3.

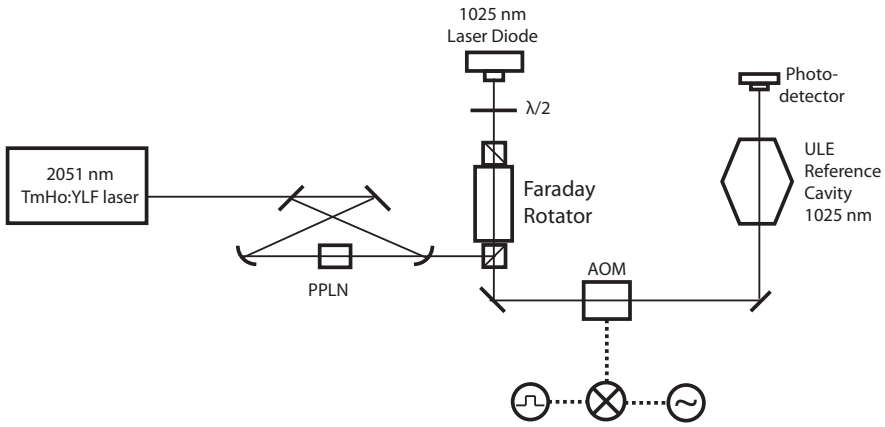

Figure 4.15: A schematic of the setup used to perform a ring down measurement of the ULE cavity. The injection locked diode was necessary to compensate for extremely poor cavity transmission. The cavity has since been cleaned and the amplifier is no longer necessary

The time constant of the decaying exponential fit to this data is 2.5 μs. This implies that the cavity had a finesse of 60,000. By most standards this would be a very good optical resonator however the manufacturer specified that this cavity would have a finesse greater than 300,000. We suspected that perhaps some contaminant on the surface of the cavity mirrors was both ruining the finesse of the cavity and absorbing light much of the light that was being coupled into the cavity. We sent the cavity back to the manufacturer and they reported that the cavity mirrors were covered in some sort of grease. The source of this grease is unknown. After the cavity was cleaned by the manufacturer we repeated this measurement. We were able to couple approximately 25% of the incident light into the lowest order cavity mode. This was enough for us to forgo the amplifier. This time a ring down measurement indicated a cavity finesse of approximately 300,000.

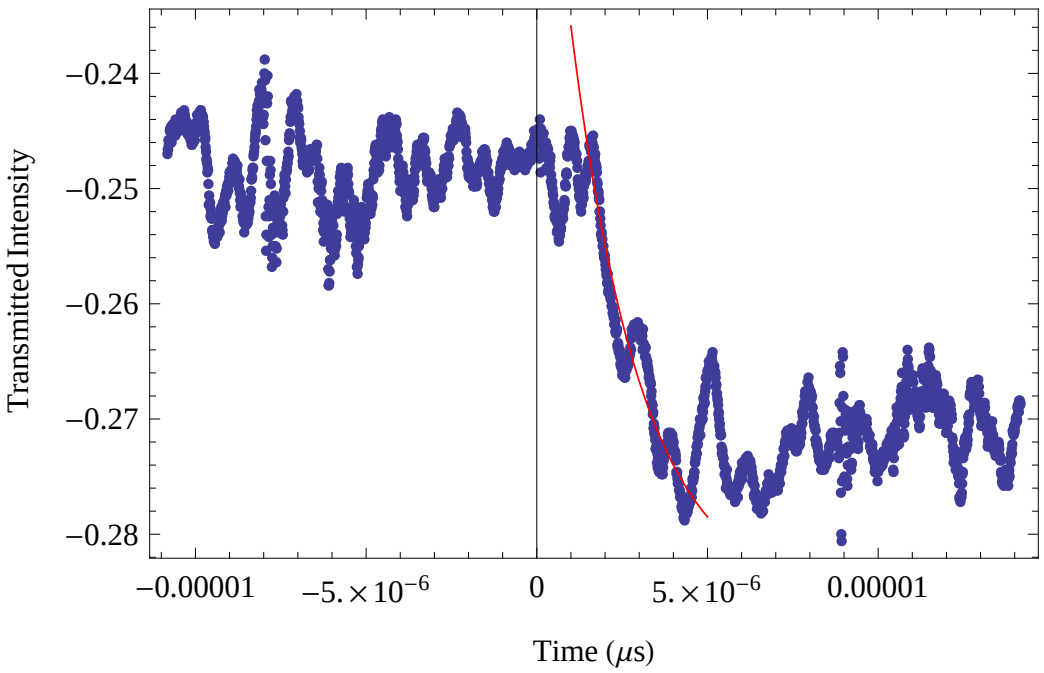

Figure 4.16: A plot of the exponential decay of light transmitted through the ULE reference cavity after the incident beam is shuttered. This data indicates a cavity finesse of 60,000 far below what the manufacturer specified. After having the cavity cleaned the finesse was measured to be greater than 300,000.

4.3.4 Frequency Stabilization of the 2051 nm Laser

The Pound-Drever-Hall frequency stabilization technique [20] has become the standard way to achieve narrow laser linewidths. For a review of this method see Appendix A

The 1025 nm light passes through a calcite polarizer to ensure that the light is horizontally polarized, then through a lithium niobate EOM phase modulator. The modulator has a built-in network of inductors and capacitors that impedance matches the device to 50 Ω when it is driven at a modulation frequency $\Omega = 20$ MHz. This device places 20 MHz sidebands on the the 1025 nm beam. Finally the 1025 nm beam then passes through a polarizing beam splitter (PBS) then a quarter wave plate (QWP) before being coupled into the ULE cavity.

The 1025 nm beam rejected from the ULE cavity is separated from the incident beam using a QWP and a PBS. After passing through the QWP a second time the beam is diverted to a high bandwidth photodetector. We found it helpful to amplify the AC coupled output of the photodetector with a low noise RF amplifier capable of 20 dB of gain. Before extracting the 20 MHz frequency component of the signal with a double balanced mixer. A low pass filter with a corner frequency of 1.9 MHz blocks out the non-DC components which have frequencies of 20, 40, 60 MHz leaving us with a PDH error signal.

The PDH error signal is split into a two channels; one responsible for servoing out slow frequency deviations from DC up to approximately 10 kHz, the other responsible for correcting fast fluctuations up to 2 MHz. The error signal in the slow feedback channel passes through a custom built double-integrator analog circuit designed to provide high gain feedback at low frequencies and less than unity gain below the resonance frequency of the tuning PZT inside the laser head. Additional circuitry allows for the laser to automatically relock to the ULE cavity in the event that the laser falls out of lock. A schematic of this rather complicated circuit is shown in Appendix B.

The error signal in the fast feedback channel is amplified then sent to the control input of a VCO with a modulation bandwidth of 2 MHz. The VCO is used to drive an AOM that also has a modulation bandwidth of 2 MHz. Fast fluctuations in laser frequency that get averaged out by the integrators in the slow channel are tracked by the circuitry in fast

channel. The frequency of the diffracted beam coming out of the AOM is corrected for these fluctuations and we the resulting lock to the ULE cavity is stable.

4.3.5 Intensity Noise on the 2051 nm Laser

It is a well known property of diode pumped solid state lasers that a spectrum of their intensity noise shows a peak at the frequency of the spontaneous decay rate of the excitations in the crystal oscillator. In the case of a Tm,Ho:YLF laser this is the decay rate of the $^5I_7$ orbital to the $^5I_8$ orbital in holmium. The intensity noise spectrum of a laser is typically given in units of relative intensity noise per hertz. Or rather the fractional depth of the modulation (expressed in decibels) in a one hertz bandwidth. Monitoring the intensity of our laser with a photodetector then performing a fast-Fourier transform using a USB oscilloscope we see a resonance in the intensity spectrum at 400 kHz.

The 2051 nm laser frequency stabilization scheme described in previous sections has the unfortunate side effect of increasing the intensity noise on the laser beam. When the frequency stabilization feedback loop is closed the error signal modulates the frequency of the VCO in order to keep the laser laser well tuned to the ULE cavity mode. However the amplitude of the VCO output varies with frequency. Furthermore if the VCO's frequency deviates from 55 MHz (the center frequency of the AOM) by a significant fraction of the AOM's 2 MHz modulation bandwidth the diffraction efficiency of the AOM decreases and intensity of the downstream beam fluctuates. The cumulative effect of these fluctuations can be seen in figure 4.17. Notice that the 35 kHz peak in the locked spectrum is added by the frequency stabilization lock.

4.3.6 An AOM for Fast Shuttering of the 2051 nm Beam and Adiabatic Rapid Passage Sweeps

A second 55 MHz AOM is placed in the path of the 2051 nm beam that is sent to the ion. This AOM is driven by the amplified output of a frequency synthesizer. The RF signal from the synthesizer passes through an RF switch that allows us to switch the diffracted beam created by the AOM on and off in approximately 100 ns. A DC coupled frequency

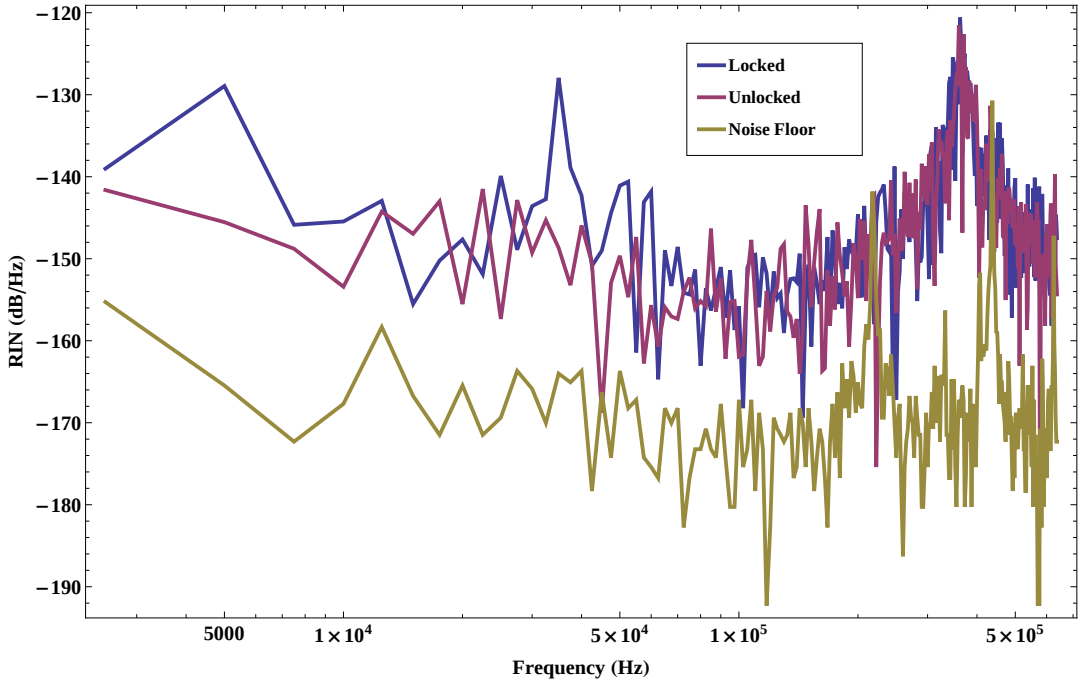

Figure 4.17: a plot of the intensity noise spectrum of the 2051 nm laser when the laser is locked to the ULE cavity and when the laser is free running. The peak at 400 kHz in both spectra is due to spontaneous decay of holmium atoms in the TM,Ho:YLF crystal. The system used to stabilized the frequency of the introduces a small amount of intensity noise on the 2051 nm laser beam. The peak at 35 kHz in the intensity noise spectrum of the locked laser results from frequency noise at the same frequency.

modulation input on the RF synthesizer allows us to change the frequency of the 2051 nm beam going to the ion without disturbing the ULE cavity lock.

4.3.7 Optical Access for the 2051 nm Beam - A Potential Problem

It seems unlikely that we will be able to use the trap used for the work described in this thesis for work on an optical frequency standard using the 2051 nm transition or the measurement of parity non-conservation proposed in [25]. This trap has four viewports for optical access which are arranged at the 12, 3, 6, and 9 o'clock positions (see figure 4.2). The proposed barium ion optical frequency standard as well as the proposed parity non-conservation measurement require driving the 2051 nm electric quadrupole $\Delta m = 0$ transition. To do so the wavevector of the laser beam should make a 45 degree angle with the external magnetic field (see figure 2.8(a)). Since both the frequency standard and the parity measurement require optical pumping, the magnetic field must be either parallel or perpendicular to one of the viewports (depending on which optical pumping scheme we use. See section 2.5.) Meeting all these requirements is not possible with the optical access currently available to us. Constructing a new trap or modifying the current trap to allow for optical access at 45 degrees would solve this problem.

4.4 Shelving and Deshelving Lights

In the course of a measurement the only information we receive from the ion is the fluorescence signal recorded by the PMT. Collecting data from a trapped ion basically amounts to exposing the ion to a sequence of pulses of radiation then recording whether the ion fluoresces when the cooling lasers are turned on. It is therefore necessary to have the ability to transfer the ion to a state in which it will not interact with the cooling lasers.

There are two practical ways to accomplish this. A barium ion in the ground state exposed to 1762 nm radiation will be excited to the $5D_{5/2}$ level via an electric quadrupole transition. It will remain in the $5D_{5/2}$ level for approximately 30 seconds. This is an eternity on the time scale of an atomic physics experiment and gives us plenty of time to turn on the cooling lasers and observe whether the ion is bright or dark. The process of removing the ion from the cooling cycle by transferring it to the $5D_{5/2}$ state is known as 'shelving' [45].

Shelving barium ions via the 1762 nm electric dipole transition was first studied by Dehmelt [45] and later has recently been used as the basis for quantum information experiments [19].

While shelving via the 1762 nm transition is the most direct way of removing the ion from the cooling cycle it poses certain challenges. The 1762 nm transition is an electric quadrupole transition with an extremely narrow natural linewidth. Finding such narrow lines in an atomic spectrum is not trivial. Furthermore one must prevent the ion from being transfered to the $5D_{5/2}$ state then back again via the same transition. This means either using a technique such as adiabatic rapid passage [41] or creating well timed 'π-pulses' of 1762 nm light.

Instead we opted to use a different shelving method. An ion in the $6S_{1/2}$ level can be transfered to the $6P_{3/2}$ level via a 455 nm electric dipole transition. We generate this light using a 1 W LED with a center wavelength of 455 nm. From the $6P_{3/2}$ level it will quickly decay following one of three decay channels (see figure 4.18) [38]. 75.6% of the time the ion will simply return to the ground state. However by making the pulse of 455 nm radiation sufficiently long we can effectively eliminate this possibility. With the ground state decay channel eliminated the ion will decay to the $5D_{5/2}$ state with a probability of 88% where it will remain shelved allowing for state detection. The remaining 12% of the time the ion falls into the $5D_{3/2}$ level. When this happens the ion remains in the cooling cycle and it will appear as if the shelving attempt failed when the cooling lasers are turned back on. As we will see in chapter 5 spectroscopic features observed using this shelving method appear on top of a $\sim$12% background. A shelved ion can be returned to the cooling cycle with a pulse from a similar LED with a center wavelength of 614 nm.

While a direct shelving scheme using the 1762 nm transition would be more efficient, our LED scheme does not require any laser stabilization and we need not worry about 'finding the transition'. The primary drawback to this method is that the LED pulses must be long in order to achieve efficient population transfer. There are two reasons for this. First, the spectrum of the light emitted by both the 455 nm and the 614 nm diodes is approximately 20 nm broad. Only a small fraction of the power emitted by the diodes is in the 100 MHz bandwidth that will drive the 455 nm or 614 nm transitions. Second the LED light has a great deal of structure and cannot be well columnated. It has proved impossible to focus

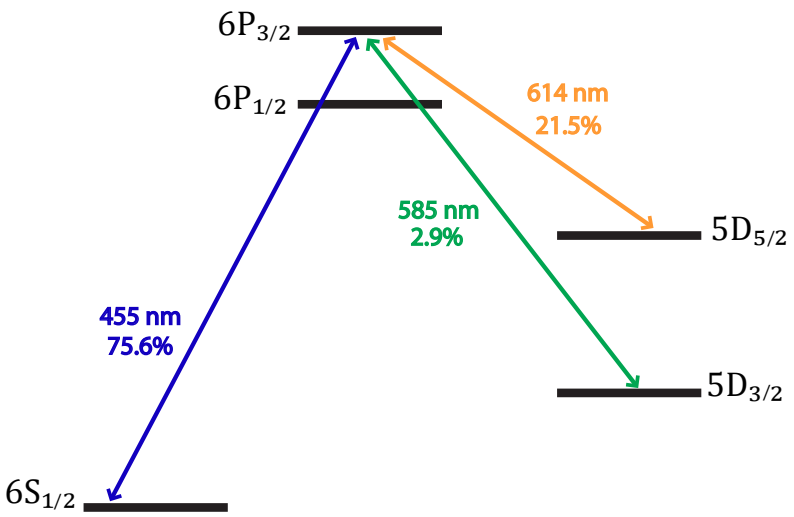

Figure 4.18: Branching ratios of the $6P_{3/2}$ level in Ba^{+}.

the light from these LED's to a spot smaller than several millimeters. As a result we must use 200-300 ms LED pulses. The duration of these pulses currently limits the repetition rate of our experiments.

The ideal way for us to drive the 455 nm shelving transition would be with a 455 nm laser. 455 nm laser diodes have recently become available however they currently are somewhat difficult to obtain and quite expensive. An alternative would be to frequency double light from a 910 nm laser diode which are readily available. We are currently investigating the possibility of converting a 920 nm external cavity diode laser (previously used for a trapped indium ion experiment) into a 910 laser. A crystal and enhancement cavity suitable for this purpose are already in place. If we were to replace our 455 nm LED with a laser but keep the 614 nm diode for deshelving we would increase the repetition rate of the experiment by approximately a factor of two. Fortunately we have access to 614 nm laser light generated by a 1228 nm ECDL frequency doubled by a fiber coupled PPLN crystal. We have successfully demonstrated the ability to deshelve using this light

4.5 Radio Frequency Radiation for Magnetic Dipole Transitions

A precision measurement of hyperfine structure requires the ability to drive magnetic dipole transitions at RF frequencies. This can be realized by simply running an oscillating current through one of the grounded trap rods. This will generate electro-magnetic radiation at the frequency of the oscillating current. At the center of the trap the orientation of the magnetic field vector as well as the wavevector of the radiation will both make an angle of 45 degrees with the quantization axis. Referring to figure 2.7(a) we see while the orientation of the wavevector and magnetic field vectors are not ideal for driving magnetic dipole transitions, the strength of the transition (i.e. the square of the Rabi frequency) will be reduced by a factor of 4/3. If needed we can always increase the Rabi frequency by increasing the oscillating current.

Although this feat has not been demonstrated on this apparatus it has been used with great success in a measurement of the AC Stark shift of the $6S_{1/2}$ and $5D_{3/2}$ levels due to off resonant light [57] as well as a the means of performing single qubit operations in a quantum information experiment [19]. It should be straight forward to add this capability to our setup.

4.6 Micromotion Compensation

We conclude our discussion of the apparatus with by presenting the results of a preliminary attempt to minimize the micromotion of trapped barium ions in our trap as defined in Chapter 3.

Excess micromotion can create serious systematic errors in precision measurements performed on trapped ions. A more robust and permanent scheme will have to be implemented if we are to carry out the proposed PNC measurement [25] or construct a competitive optical frequency standard. By applying DC voltage offsets to the rod electrodes one can in principle cancel any stray DC electric fields [6].

Micromotion has a definite phase relationship to the RF trap voltage. When the trap voltage causes the ion to move in a direction that has a component (anti-)parallel to the laser beams wavevector, the frequency of the laser as seen by the ion is Doppler shifted to

the (blue)red. If we detune the laser to the red of the atomic transition the frequency of the laser as seen by the moving electron is Doppler shifted towards the frequency of the atomic transition when the ion is moving in a direction anti parallel to the laser beam causing the transition rate to increase. On the $6S_{1/2} \leftrightarrow 5D_{3/2}$ transition this can be observed as an increase in ion fluorescence. Micromotion perpendicular to the laser beam has no effect. Micromotion can therefore be detected as a correlation between the ion fluorescence and the phase of the trap voltage.

We were able to observe this correlation using a Time to Amplitude Converter (TAC) and a pulse height analyzer (PHA). We connected the output of our PMT to the START input on the TAC. The function generator used to generate trap RF at 22.8 MHz has a TTL output that pulsed high at the beginning of each RF cycle. We connected this TTL signal to the STOP input on the TAC. In this way we were able to measure the between each PMT click and the beginning of the next RF cycle. This is equivalent to measuring the RF phase at which each photon count occurred.

The TAC converts these times into pulses with amplitudes proportional to the measured times. These pulses were sent to the PHA which placed each pulse in 1 of 1025 bins according to the pulse height. The PHA then produced a histogram. We adjusted the DC bias on three of the trap rods until the histogram was nearly flat as illustrated in figure 4.19. This indicates that the micromotion parallel to the direction of the laser beam was well compensated.

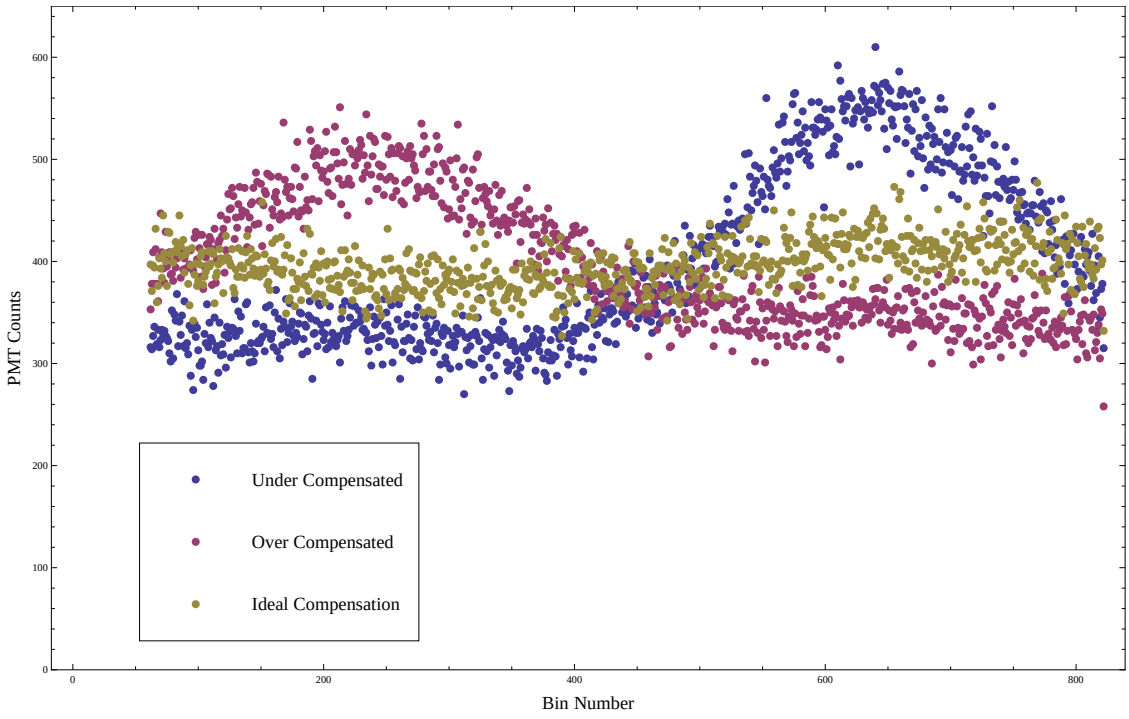

Figure 4.19: A plot of ion florescence as a function of trap RF phase when three different biasing voltages were applied to the trap rods. The data were collected using a TAC and pulse height analyzer as described in [6]. This technique can be used to minimize the micromotion of a trapped ion.

Chapter 5

SPECTROSCOPIC MEASUREMENTS OF THE $6S_{1/2} \leftrightarrow 5D_{3/2}$ TRANSITION

We now describe a series of measurements performed with the 2051 nm laser system. These measurements demonstrate our ability to address the 2051 nm electric quadrupole transition and provide an upper bound on the linewidth of the 2051 nm laser after stabilization.

5.1 Procedure

Spectroscopic measurements of the $6S_{1/2} \leftrightarrow 5D_{3/2}$ 2051 nm electric quadrupole transition in a barium ion are complicated by the fact that both the upper and lower levels connected by this transition are part of the cooling cycle. Consider first the procedure for performing spectroscopic measurement of the $6S_{1/2} \leftrightarrow 5D_{5/2}$ 1762 nm transition (see [69] for example). The appropriate sequence of operations can be summarized as follows:

(a) Initialize the ion into a well defined state in the $6S_{1/2}$ level

(b) Turn off 493 nm and 650 nm lasers

(c) Attempt to drive the 1762 nm transition

(d) Turn on 493 nm and 650 nm lasers

(e) Is the ion bright? No - the transition occurred. Yes - the transition did not occur.

(f) Deshelve if necessary

(g) Re-tune the 1762 nm laser.

(h) Repeat and accumulate statistics.

The same procedure would not work for performing spectroscopy on the 2051 nm transition. The 2051 nm transition does not remove the ion from the cooling cycle so the ion would always fluoresce whenever the 493 nm and 650 nm lasers are turned on and nothing would be learned. Our solution is to insert a shelving pulse of 455 nm light before turning on the cooling lasers to check whether the ion is bright. If the 2051 nm transition did not occur the ion will be in the ground state and the shelving pulse will transfer the ion population to the $5D_{5/2}$ level. The ion will be not fluoresce when the cooling lasers are turned on. If the 2051 nm transition did occur the ion will be in the $5D_{3/2}$ level and will fluoresce. The operations we we use to do 2051 nm spectroscopy on a ^{138}Ba ion can be summarized as follows

(a) Optically pump to a ground-state Zeeman level

(b) Turn off 493 nm and 650 nm light

(c) Apply 2051 nm laser pulse pulse

(d) Pulse the 455 nm shelving LED

(e) Turn on 493 nm and 650 nm lasers

(f) Detect ion fluorescence (if any)

(g) Deshelve if necessary

(h) Re-tune the 2051 nm laser.

(i) Repeat and accumulate statistics.

By repeating this pulse sequence many times at different laser tunings we can create histograms of the number of times we detected a dark ion as a function of frequency (remember that the ion is dark when the 2051 nm transition occurs).

5.2 Observed Line Shapes

Ideally these histograms would look like the plots in figures 2.4 and 2.2. However several steps in this sequence are less than 100% efficient and as a result the lineshapes we observe are slightly distorted. If the ion does not begin the pulse sequence in the correct Zeeman level it will not be able to absorb the 2051 nm radiation even if the 2051 nm laser is tuned correctly. Also our method of shelving the ion does not transfer an ion in the ground state to the $5D_{5/2}$ state with 100% efficiency as discussed in section 4.4. The combined effect of these inefficiencies is illustrated in figure 5.1. The probability of observing a dark ion can be shown to be

$$P_{dark} = S(1 - PT) \tag{5.1}$$

where S is the shelving efficiency, P is the optical pumping efficiency, and T is the efficiency of driving the 2051 nm transition. Equation 2.18 is an expression for the probability that an atomic transition occurred. If we us this expression to replace T in eq. 5.1 we have the following.

$$P_{dark} = S\left(1 - P\frac{\Omega^2}{2(\Omega^2+\delta^2)}\left(1 - e^{-\frac{t}{\tau}}\cos\left(\sqrt{\Omega^2+\delta^2}t\right)\right)\right) \tag{5.2}$$

5.3 Finding the 2051 nm Transition

We used a wavemeter to measure the wavelength of the frequency doubled 1025 nm beam. We then coarse tuned the 2051 nm laser by adjusting the temperature of the crystal resonator until the frequency at which we expected to find the 2051 nm transition was within the tuning range of the laser's PZT. We then performed scans of the laser frequency using the procedure described earlier in this chapter except for the fact that for these preliminary scans the laser was not locked to the ULE cavity. Instead we controlled the laser's PZT directly with our data acquisition software. After optically pumping the ion into the ground state the 2051 nm laser was exposed to the ion and the control program initiated a .25 second sweep of the several tens of megahertz in laser frequency. Histograms of the shelving efficiency made from these scans showed a well resolved peak. Although the peak was many

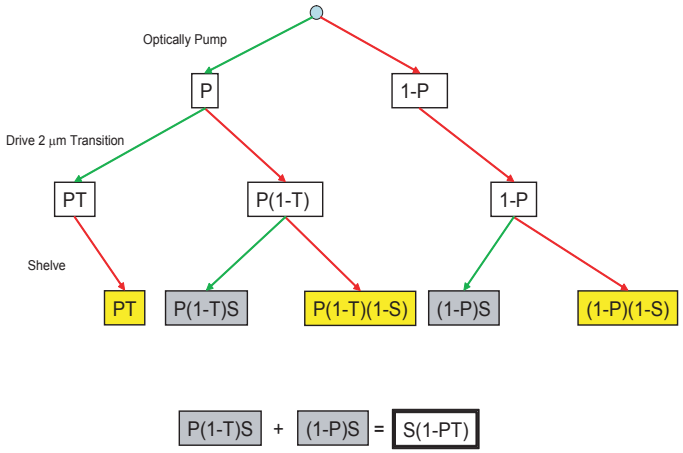

Figure 5.1: A graphical representation of the effect of optical-pumping efficiency (P), 2051 nm transition efficiency (T), and shelving efficiency (S) on the probability of observing a bright ion after a standard 2051 nm spectroscopy pulse sequence. When a step succeeds it is represented by a green arrow. When a step fails it is represented by a red arrow. Final outcomes that result in the detection of a bright ion are highlighted in yellow. The probability of observing a dark (i.e. shelved) ion is $S(1 - PT)$

orders of magnitude broader than the natural linewidth of the 2051 nm transition it was proof that we were successfully driving the $6S_{1/2}$ to $5D_{3/2}$ transition.

For the work described in this thesis the 2051 nm laser was linearly polarized and its wave vector was parallel to the ion's quantization axis. This means that only $|\Delta m| = 1$ transitions were allowed (see figures 2.8(a), 2.8(b), and 2.8(c)). Given that we are optically pumping into the $m = +1/2$ state we expect to see two lines in this spectrum; one corresponding to the transition to the $5D_{3/2}$ $m = -1/2$ state and one to the $5D_{3/2}$ $m = +3/2$ state. The peak that we observed by ramping the voltage going to the laser's PZT was much broader than the frequency interval separating these two lines that one would expect from the first order Zeeman effect. We therefore knew that both $|\Delta m| = 1$ transitions were in the region spanned by broad peak. We locked the laser to the ULE cavity and narrowed our search.

5.4 Narrow Spectroscopy and Rabi Flops on the 2051 nm Transition

Using the sequence of operations described in the beginning of this chapter we found the two transitions. We first performed a number of narrow scans on the higher frequency

line. Through trial and error we determined the optimal 2051 nm laser pulse duration for transferring ion population to the $5D_{3/2}$ level to be approximately 250 μs when sending all of the available 2051 nm light to the ion. Using this pulse time we scanned the laser frequency and recorded the shelving efficiency. The result is shown in figure 5.2. By fitting a Gaussian function to these data we determined this peak to be 3.1 kHz broad (FWHM). The Fourier transform of a square pulse of duration 250 μs resembles a sinc function with a linewidth of approximately 4 kHz FWHM. We can therefore say that the linewidth of this peak is not limited by laser noise or magnetic field noise but rather the finite interaction time between the ion and the laser.

We then tuned the laser to the center frequency of this peak and measured the shelving probability as a function of 2051 nm exposure time. A plot of these data shown in figure 5.3 show well resolved oscillations in the population of the $5D_{3/2}$ level as a function of pulse duration demonstrating coherent laser-ion interactions. They are known colloquially as 'Rabi flops'. By fitting the free parameters in eq. 5.2 (with $\delta = 0$) to the data we determined the shelving efficiency S, the optical pumping efficiency P, the frequency of oscillation Ω, and the exponential decay time constant τ.

$$S = .80$$

$$P = .96$$

$$\Omega = 12.4 \text{ kHz}$$

$$\tau = 2 \text{ ms}$$

Evidently we are able to use the 2051 nm laser to coherently interact with the ion for approximately 2 ms; much longer than the 250 μs used for the previous frequency scan. We decreased the intensity of the 2051 nm light and varied the 2051 nm laser pulse duration. The data are shown in figure 5.4. By fitting the same damped oscillatory function (eq. 5.2) to these data we determined the optimal pulse for population transfer to be approximately 500 μs. We performed another frequency scan using this pulse time. The data from this scan are shown in figure 5.5. The observed peak has a linewidth of approximately 700 Hz. This could be reduced further by using a longer pulse duration but as the pulse duration approaches the 2 ms coherent laser-ion interaction time, the height of the observed peaks

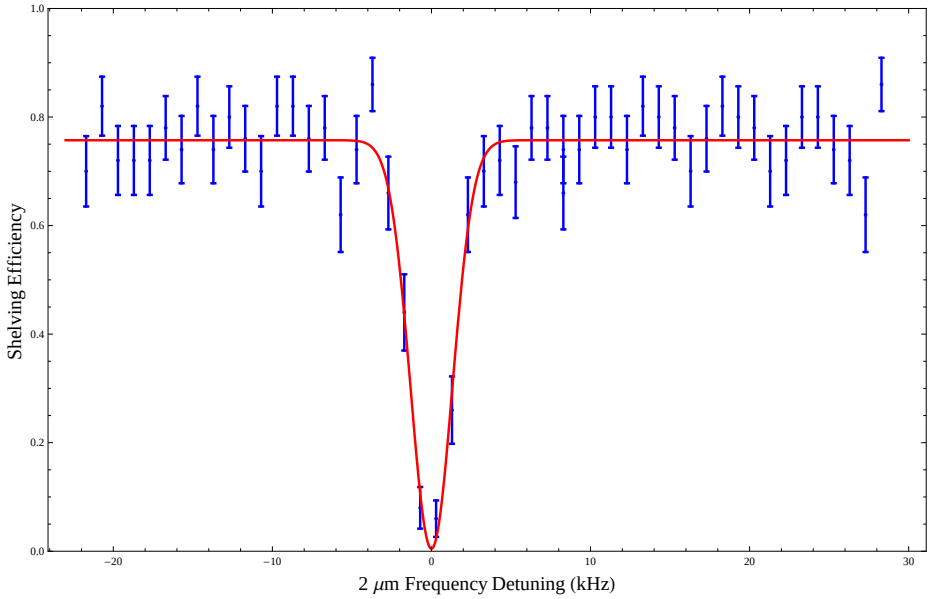

Figure 5.2: A plot of shelving efficiency as a function of Tm,Ho:YLF laser frequency. The dip in shelving efficiency is due to the $6S_{1/2}$, m=1/2 to $5D_{3/2}$ m=3/2 transition in ^{138}Ba. The laser was exposed to the ion for 250 μs.

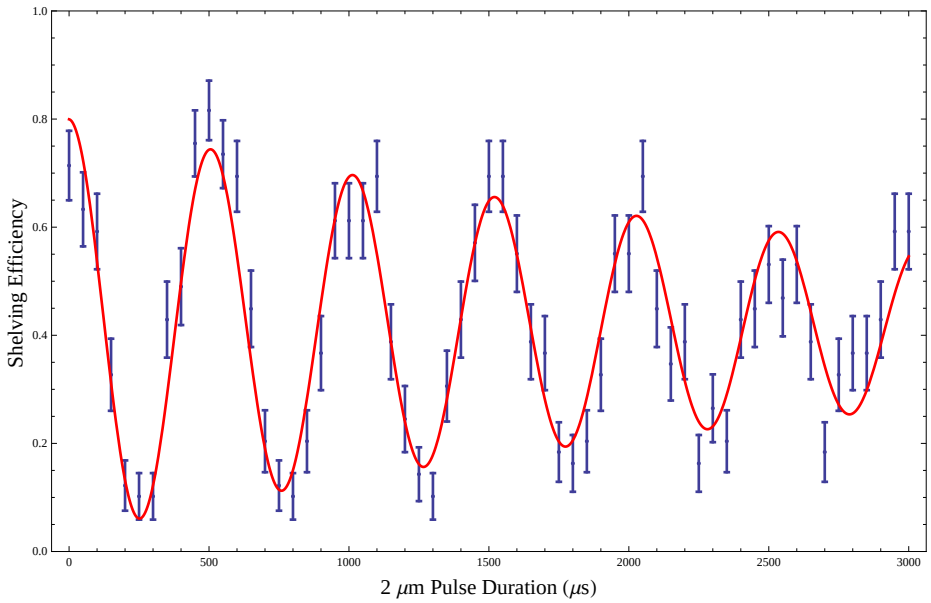

Figure 5.3: A plot of shelving efficiency as a function of laser pulse duration with the Tm,Ho:YLF laser tuned to the $6S_{1/2}$, m=1/2 to $5D_{3/2}$ m=3/2 transition in ^{138}Ba.

will be reduced. When we varied the duration of the 2051 nm laser exposure time while

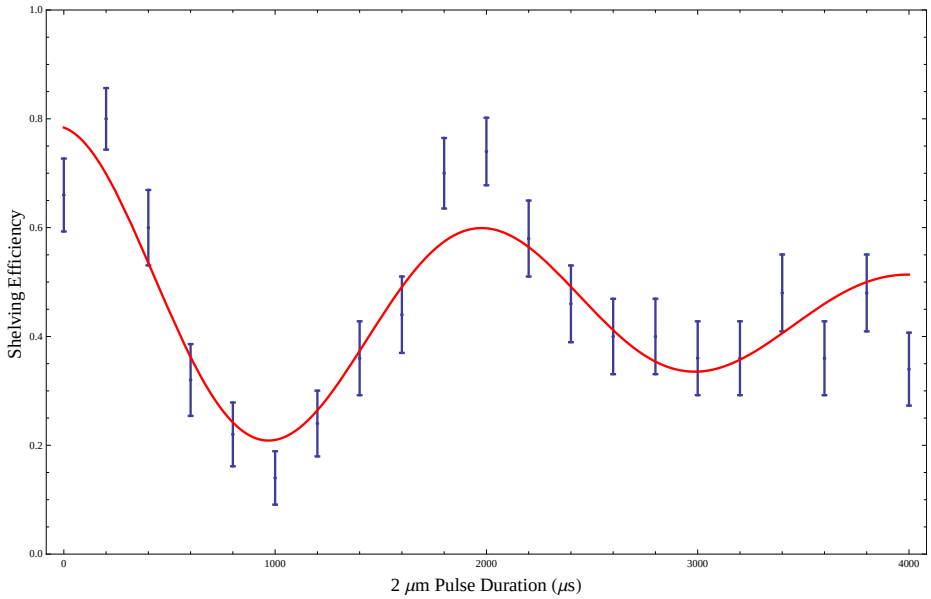

Figure 5.4: A plot of shelving efficiency as a function of laser pulse duration with the Tm,Ho:YLF laser tuned to the $6S_{1/2}$, m=1/2 to $5D_{3/2}$ m=3/2 transition in ^{138}Ba. A reduced laser intensity was used.

tuned to the lower frequency $m = \frac{1}{2}$ to $m = -\frac{1}{2}$ line we saw a similar Rabi flops but the frequency of oscillation in the population of the excited state was lower. A plot of these data is shown in figure 5.6.

5.5 Magnetic Field Dependence of 2051 nm Transition Frequency

As stated in section 2.4, the value for the Lande g factor for the ground state is very close to $g = 2$ and for the $5D_{3/2}$ level it is nearly $g = \frac{4}{5}$. From this we can calculate how the two $\Delta m = \pm 1$ transitions should respond to changes in the magnetic field. If the magnitude of the magnetic field changes by an amount ΔB, a particular Zeeman state with magnetic quantum number m will experience an energy shift $\Delta E = \mu_B \Delta B g m$. The two $\Delta m = 1$

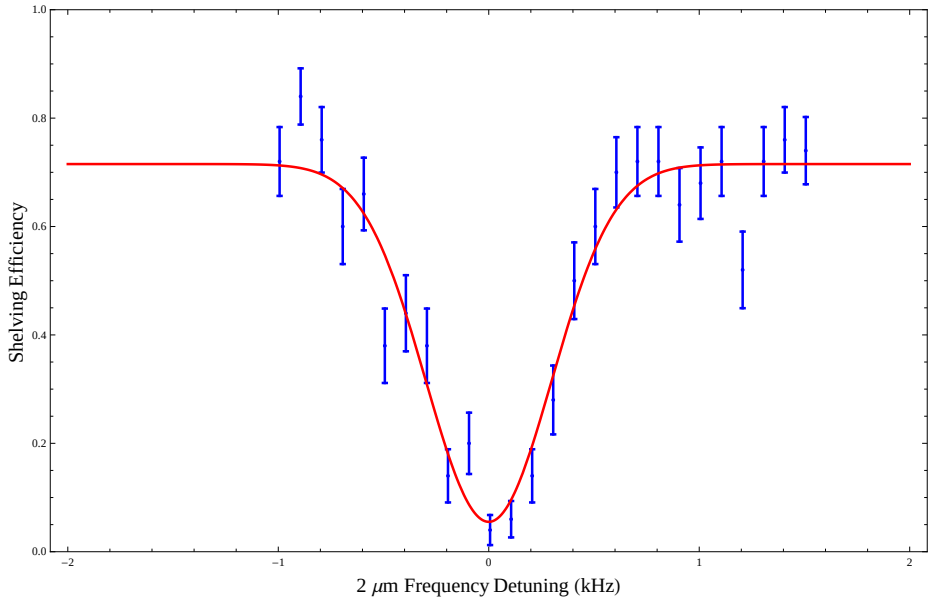

Figure 5.5: A plot of shelving efficiency as a function of Tm,Ho:YLF laser frequency. The dip in shelving efficiency is due to the $6S_{1/2}$, m=1/2 to $5D_{3/2}$ m=3/2 transition in ^{138}Ba. The laser was exposed to the ion for 1 ms.

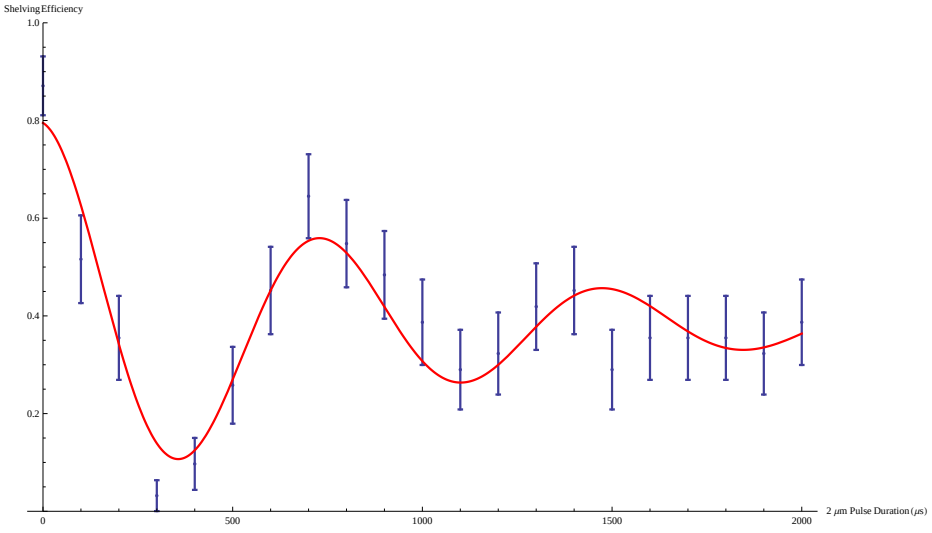

Figure 5.6: A plot of shelving efficiency as a function of laser pulse duration with the Tm,Ho:YLF laser tuned to the $6S_{1/2}$, m=1/2 to $5D_{3/2}$ m=-1/2 transition in ^{138}Ba. A reduced laser intensity was used.

transitions in a ^{138}Ba ion will be shifted in the following way.

$$\Delta E = \mu_B \Delta B \left(g_u m_u - g_l m_l\right)$$

$$\Delta E = \mu_B \Delta B \left(\frac{4}{5} \times \frac{3}{2} - 2 \times \frac{1}{2}\right) = \frac{1}{5}\mu_B \Delta B \tag{5.3}$$

$$\Delta E = \mu_B \Delta B \left(\frac{4}{5}\left(-\frac{1}{2}\right) - 2 \times \frac{1}{2}\right) = -\frac{7}{5}\mu_B \Delta B \tag{5.4}$$

The energy difference between these two levels should scale with the magnetic field as $\Delta E = \frac{8}{5}\mu_B B$. With the magnetic field used for the scans described in the previous section these two lines were separated by 7.35 MHz. This implies that the magnetic field seen by the ion is

$$B = \frac{7.35\text{MHz} \times h}{\frac{8}{5}\mu_B}$$

$$\approx 3.4 \text{ Gauss}$$

When we changed the magnetic field by a small amount we observed that the higher frequency line moved by .017 MHz while the lower frequency moved by .125 MHz. Since the upper level shift was approximately a factor of seven smaller than the lower level shift we can conclude that the upper line is the $m = \frac{1}{2}$ to $m = \frac{3}{2}$ transition and the lower line is the $m = \frac{1}{2}$ to $m = -\frac{1}{2}$ transition. Spectroscopy of these lines at a number of different magnetic field values would constitute a measurement of the Lande g factor for the $5D_{3/2}$ level. A precision measurement of this g factor carried out in 1996 [36] measured $g_{3/2}$ to seven decimal places. Improving on their impressive level of precision would be challenging yet may be possible.

We do not yet have the ability to perform a direct measurement of the 2051 nm laser linewidth so we cannot say for certain that laser frequency noise is not limiting the performance of these spectroscopic studies however estimates of the stability provided by our ULE cavity lock suggest that the 2051 nm laser may be quiet enough to allow for much longer coherence times. Enclosing the ion trap in a layer of μ-metal magnetic shielding would improve the laser-ion coherence times if indeed magnetic fluctuations in the external magnetic field seen by the ion is the dominant source of noise.

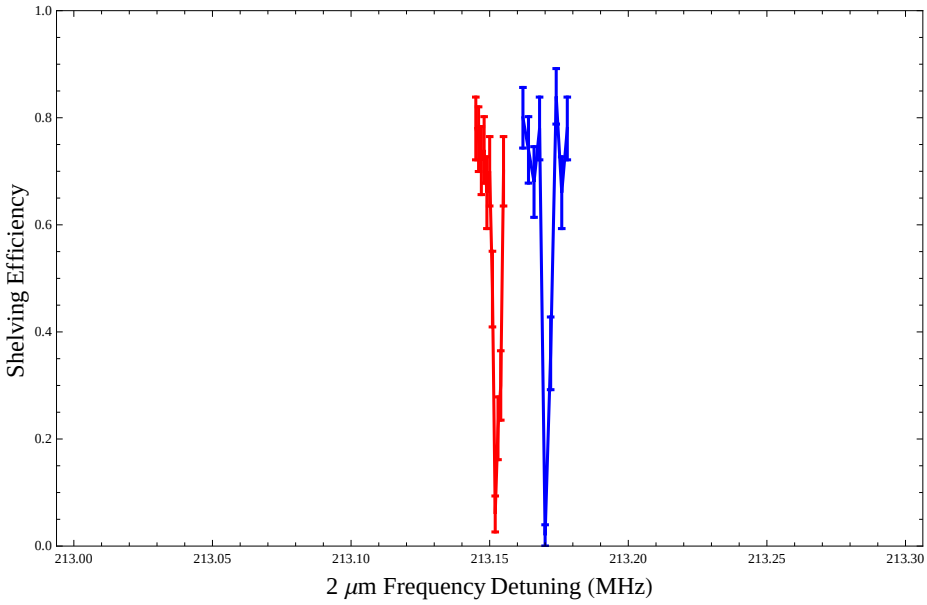

Figure 5.7: one zeeman

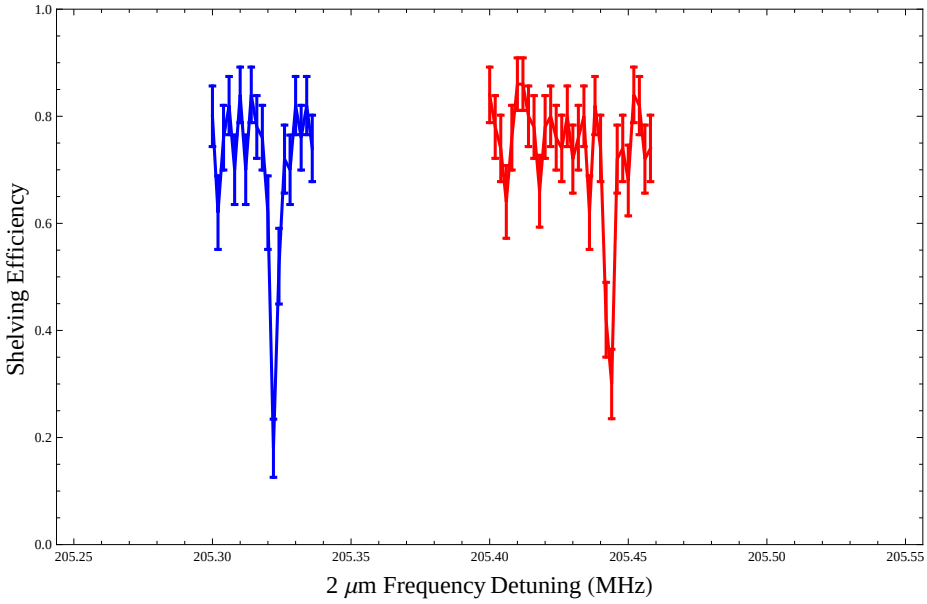

Figure 5.8: The $6S_{1/2}$ m=1/2 to $5D_{3/2}$ m=-1/2 transition in ^{138}Ba at two different external magnetic field strengths. Higher magnetic field shown in blue.

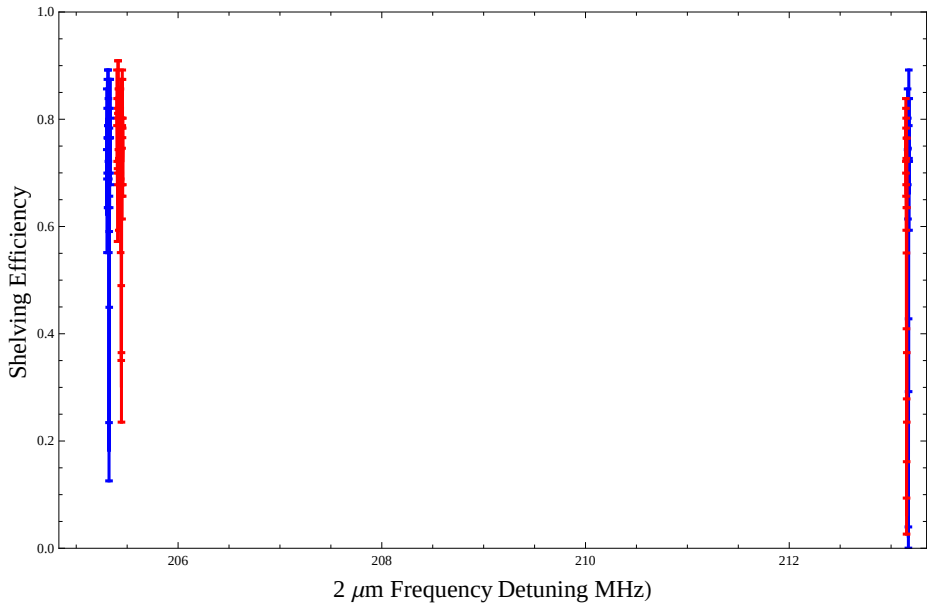

Figure 5.9: The $6S_{1/2}$ m=1/2 to $5D_{3/2}$ m=3/2 and m=1/2 to m=-1/2 transitions in ^{138}Ba at two different external magnetic field strengths. Higher magnetic field shown in blue.

Chapter 6

MEASURING THE NUCLEAR MAGNETIC OCTUPOLE MOMENT OF BA-137

Given the large difference in energy between the strong nuclear interactions and electro-magnetic atomic interactions, it is perhaps surprising that the tools of atomic physics would be able to probe nuclear structure. However we have seen in the simple picture of the hyperfine interaction presented in section 2.1.3 that the electro-magnetic field generated by the magnetic dipole moment of a nucleus coupled to the orbiting electrons leads to measurable energy level splittings.

In the simple picture of the hyperfine interaction presented in section 2.1.3 we assumed that the nucleus was a massive point charge that possessed intrinsic spin angular momentum I. In reality an atomic nucleus possesses internal structure and as a result the electric and magnetic fields it creates can not be fully described by a Coulomb potential and a magnetic dipole field. Higher order electric and magnetic multipole moments of the fields created by the protons and neutrons in the nucleus couple to the orbiting electrons and produce higher order corrections to the energies of the hyperfine sub levels we would expect from just a magnetic dipole interaction. We will show that in some cases, precision measurements hyperfine splittings allow one to extract values for the electric and magnetic multipole moments of the nucleus. We will then review a proposed method for performing such a measurement on a trapped ^{137}Ba ion.

6.1 The Nuclear Shell Model

The electrons in the noble gases exist in particularly stable configurations because they completely fill the atomic orbital 'shells' that arise from a quantum mechanical treatment of electronic angular momentum. The fact that nuclei with certain 'magic numbers' of nucleons are particularly stable suggests that a similar shell model might describe nuclear structure. The single particle nuclear shell model is a simple model of the nucleus that

succeeds in capturing the 'magic number' phenomenon. We will use its predictions for the magnitude of the electric and magnetic multipole moments of the ^{137}Ba nucleus to get a sense of the magnitude of the shifts to hyperfine sublevels due to various nuclear moments.

The NSM assumes that each nucleon moves in a spherically symmetric central potential. The Z protons and N neutrons in the nucleus fill up the angular momentum states with lowest energy first. The Pauli exclusion principle allows no more than two nucleons to occupy a single angular momentum state. In the lowest energy configuration the protons and neutrons will pair up with a nucleon of the same type but opposite spin orientation. If the nucleus possesses an odd number of protons or neutrons, there will be one unpaired nucleon. The spin of this nucleon can be either up or down. Coupling between the spin and orbital angular momentum of this nucleon splits the energy level into an L+1/2 and an L-1/2 nuclear angular momentum state. The following expressions for th electric dipole, magnetic quadrupole, and magnetic octupole moment of the nucleus in one of these states can be found in the literature [53].

$$\mu = \mu_N I \begin{cases} g_l + (g_s - g_l)/2I \text{ for } I = l + \frac{1}{2} \\ g_l - (g_s - g_l)/2I \text{ for } I = l - \frac{1}{2} \end{cases} \tag{6.1}$$

$$Q = -\frac{1}{2}\frac{2I-1}{2I+2} e g_l \left\langle r^2 \right\rangle \tag{6.2}$$

$$\Omega = \mu_N \frac{3}{2}\frac{(2I-1)}{(2I+4)(2I+2)} \left\langle r^2 \right\rangle \begin{cases} (I+2)\left[(I-\frac{3}{2})g_l + g_s\right] \text{ for } I = l + \frac{1}{2} \\ (I-1)\left[(I+\frac{5}{2})g_l - g_s\right] \text{ for } I = l - \frac{1}{2} \end{cases} \tag{6.3}$$

$g_l = 1$ and $g_s = 5.58$ for an unpaired proton and $g_l = 0$ and $g_s = -3.83$ for an unpaired neutron. A 2003 measurement [30] of the hyperfine structure of the 6P3/2 level in cesium-133 suggested that its nuclear magnetic octupole moment was 40 times larger than the value predicted by the nuclear shell model. While the shell model is only a rough approximation of nuclear structure the discrepancy is surprising. A barium nucleus contains just one more proton than cesium. It is therefore natural to wonder if the magnetic octupole moment of a barium nucleus differs from the shell model prediction as well. To get a feel for how the predictions of the shell model hold up to experimental data let us compare the shell model predictions for the nuclear moments in ^{133}Cs and ^{137}Ba to the accepted values for

	μ (μ_N)		Q (b)		Ω (b$\times\mu_N$)	
	N.S.M	Experiment	N.S.M*	Experiment	N.S.M*	Experiment
^{137}Ba	1.4894	1.21013	0	+.245	0.21138	-
^{133}Cs	1.71889	2.9277407	-.0770242	-.0043(10)	.0220569	0.820(10)

Table 6.1: *Assuming the radius of the unpaired nucleon is equal to to the r.m.s charge radius $\langle r^2 \rangle^{1/2} = 4.84$ fm [30].

the magnetic dipole and electric quadrupole movements. Quadrupole moments are quoted in units of barns (b).

$$1\text{b} = 10^{-28}\ \text{m}^2$$

The NSM clearly has some problems predicting nuclear multipole moments. One particularly striking shortcoming of this model is that it predicts zero electric quadrupole moment for all nuclei with unpaired neutrons. Nevertheless the fact that the nuclear magnetic octupole moment of ^{133}Cs is 40 times larger than the predictions of the shell model is striking.

6.2 Higher Order Hyperfine Interactions

The hyperfine interaction is the coupling of non-uniform nuclear charge and current distributions to the bound electrons. In order to cast this problem in a more tractable form we make several reasonable assumptions. First, we assume that when the the outermost electron is in the $5D_{3/2}$ level it occupies a region of space far from the nucleus. This allows us to perform a multipole expansion of the scalar and vector potentials generated by the nucleus. We can then write the terms in the expansion as a sum of rank-k tensor operators that act on the nuclear wavefunctions. A similar set of operators that act on the electronic wavefunctions can also be constructed. The Hamiltonian operator describing the hyperfine interaction can finally be written as a sum of products of electronic and nuclear tensor operators.

Second, we assume that the nucleus always remains in its lowest energy state. Nuclear energy scales are orders of magnitude beyond the energies supplied by the optical and RF radiation sources used in this experiment. Third we assume that the nuclear ground state

has a well defined parity. Because of this last requirement it can be shown that rank-k electric nuclear multipole operators of rank-k vanish when k is even and magnetic nuclear multipole operators vanish when k is odd. The hyperfine Hamiltonian can be written as follows

$$H_{hyp} = \sum_{k>0} \underbrace{G^{(k)} \cdot F^{(k)}}_{electric} + \underbrace{M^{(k)} \cdot N^{(k)}}_{magnetic} \tag{6.4}$$

where $G^{(k)}$ and $M^{(k)}$ are rank-k spherical tensor operators that act on the electronic wavefunctions and $F^{(k)}$ and $N^{(k)}$ are rank-k spherical tensor operators that act on the nuclear wavefunctions. For a more detailed derivation of this Hamiltonian the reader see Appendix C

6.3 Perturbation Theory

Our plan now is to calculate the effect of these operators using degenerate perturbation theory. As in the elementary treatment of the hyperfine interaction presented in section 2.1.3 we will use the states $|JIFm_F\rangle$ as our basis.

The electric nuclear operator $D^{(k)}$ has the same parity as the spherical harmonic $Y^{(k)}$ while the magnetic nuclear operator $N^{(k)}$ has the same parity as $Y^{(k-1)}$. Therefore integrals of the form

$$\int \psi'^{*}_{N} D^{(k)}(r_n) \psi_N d\tau$$

vanish for odd values of k and integrals of the form

$$\int \psi'^{*}_{N} N^{(k)}(r_n) \psi_N d\tau$$

vanish for even values of k.

The nuclear wavefunction ψ_N describes a state with angular I. Diagonal matrix elements formed from these states with a rank-k tensor operator $T^{(k)}$ can be thought of as the scalar 'triple product' of three tensors and we can write [59]

$$\left\langle Im_{I'} \middle| T^{(k)}_q \middle| Im_I \right\rangle = -\frac{1}{3} \sum_{m'_I q m_I} \begin{pmatrix} 1 & 1 & 1 \\ -m_{I'} & q & m_I \end{pmatrix} T^{(I)}_{m_{I'}} T^{(I)}_q T^{(I)}_{m_I} \tag{6.5}$$

The three-j symbol in eq. 6.5 will vanish unless k satisfies the triangle inequality

$$|k - I| \leq I \leq k + I$$

$$k \leq 2I$$

The nuclear ground state of ^{137}Ba has angular momentum $I = 3/2$ so we need not consider terms higher than $k = 3$ in the sum 6.4. We can make a similar argument for the electronic angular momentum and show that we must also have

$$|k - J| \leq J \leq k + J$$

$$k \leq 2J$$

6.3.1 First Order Corrections

We wish to show how the hyperfine splittings in an atom depend on the magnitude of the electric and magnetic multipole contributions. The first order correction to the energy of a state $|JIFm_F\rangle$ due to the non-zero terms in eq. 6.4 is

$$\begin{aligned} E'_{IJF} = &\left\langle JIFm_F \right| M^{(1)} \cdot N^{(1)} \left| JIFm_F \right\rangle \\ &+ \left\langle JIFm_F \right| D^{(2)} \cdot F^{(2)} \left| JIFm_F \right\rangle \\ &+ \left\langle JIFm_F \right| M^{(3)} \cdot N^{(3)} \left| JIFm_F \right\rangle \end{aligned} \quad (6.6)$$

The diagonal matrix element of the scalar product of two tensor operators, where one operator acts on nuclear wavefunctions the other operator acts on electronic wavefunctions can be decoupled in the following way.

$$\begin{aligned} \left\langle \gamma IJFm_F \right| T_n^{(k)} \cdot T_e^{(k)} \left| \gamma IJFm_F \right\rangle = &\sum_{\gamma'} (-1)^{I+J+F} \begin{Bmatrix} F & I & J \\ k & J & I \end{Bmatrix} \\ &\times \left\langle \gamma I \left\| T_n^{(k)} \right\| \gamma' I \right\rangle \left\langle \gamma' J \left\| T_e^{(k)} \right\| \gamma J \right\rangle \end{aligned} \quad (6.7)$$

For our purposes we can ignore the sum over γ' which represents any other quantum numbers necessary to define the state such as the principal quantum number n. The Wigner-Eckart

theorem 2.28 can be used to write any reduced matrix elements in terms of the expectation values of the 0^{th} component of the tensor operators in the 'stretched' angular momentum states $|II\rangle$ and $|JJ\rangle$. Eq. 6.6 can be written compactly as

$$E'_F = X_{JIF,1}\left\langle M_0^{(1)}\right\rangle_{JJ}\left\langle N_0^{(1)}\right\rangle_{II} + X_{JIF,2}\left\langle D_0^{(2)}\right\rangle_{JJ}\left\langle F_0^{(2)}\right\rangle_{II} + X_{JIF,3}\left\langle M_0^{(3)}\right\rangle_{JJ}\left\langle N_0^{(3)}\right\rangle_{II} \tag{6.8}$$

where

$$X_{JIF,k} \equiv (-1)^{F+J+I}\frac{\left\{\begin{array}{ccc} F & J & I \\ k & I & J \end{array}\right\}}{\left(\begin{array}{ccc} J & k & J \\ -J & 0 & J \end{array}\right)\left(\begin{array}{ccc} I & k & I \\ -I & 0 & I \end{array}\right)} \tag{6.9}$$

Information about the nuclear and electronic charge and current distributions is contained in the matrix elements and the $X_{JIF,k}$ are geometrical factors describing the angular momentum coupling for a particular state. Let us adopt the standard definition of the nuclear magnetic dipole, electric quadrupole, and magnetic octupole moments.

$$\begin{aligned} \mu &\equiv \left\langle N_0^{(1)}\right\rangle_{II} \\ Q &\equiv 2\left\langle F_0^{(2)}\right\rangle_{II} \\ \Omega &\equiv -\left\langle N_0^{(3)}\right\rangle_{II} \end{aligned}$$

It is also standard practice in the literature to make the following definitions.

$$\begin{aligned} A &\equiv \frac{1}{IJ}\mu\left\langle M_0^{(1)}\right\rangle_{JJ} \\ B &\equiv 2Q\left\langle D_0^{(2)}\right\rangle_{JJ} \\ C &\equiv -\Omega\left\langle M_0^{(3)}\right\rangle_{JJ} \end{aligned} \tag{6.10}$$

Numerical values for A, B, and C calculated from a previous measurement of the hyperfine structure of the $5D_{3/2}$ level in $^{137}Ba^{+}$ [65] are

$$A = 189.7296(9)\text{ MHz}$$

$$B = 44.5408(16)\text{ MHz}$$

$$C = -0.000061(54)\text{ MHz}$$

Note the large relative uncertainty on the octupole coupling constant. A calculation of the electronic wavefunctions for Ba^+ [4] predicts the following value for C in terms of Ω.

$$C(5D_{3/2}) = -0.000585(11)\ \left(\frac{\Omega}{\mu_N \times \mathrm{b}}\right) \mathrm{MHz}$$

Combining this with the NSM prediction for the nuclear magnetic octupole moment in ^{137}Ba yields

$$C^{NSM}(5D_{3/2}) \cong -0.000023 \text{ MHz}$$

The first order correction to the energy of a hyperfine sublevel can be written as

$$E'_{IJF} = AX_{JIF,1}IJ + \frac{1}{4}BX_{JIF,2} + CX_{JIF,3} \tag{6.11}$$

It should be noted that while the factors A, B, and C each depend on I and J they do not depend on the total angular momentum F. Therefore a measurement of three hyperfine intervals in the same fine-structure level (i.e. all the states have the same value for I and J) allows us to solve for the constants A, B, and C. Let us define a frequency interval between adjacent hyperfine sublevels to be.

$$\Delta E_F = E'_{IJF} - E_{IJ(F+1)}$$

For the $5D_{3/2}$ state in $^{137}Ba^+$ we have

$$\begin{aligned}
\Delta E_0 &= -A + B - 56C \\
\Delta E_1 &= -2A + B + 28C \\
\Delta E_2 &= -3A - B - 8C
\end{aligned} \tag{6.12}$$

If we solve this system of equations for the magnetic octupole moment hyperfine constant C we have

$$C(5D_{3/2}) = -\frac{1}{80}\Delta E_0^{(3/2)} + \frac{1}{100}\Delta E_1^{(3/2)} - \frac{1}{400}\Delta E_2^{(3/2)} \tag{6.13}$$

Knowledge of the electronic wavefunctions allows theorists to calculate values for the expectation value of the the electronic tensor operator $\left\langle M_0^{(3)} \right\rangle_{\frac{3}{2}\frac{3}{2}}$ contained in the octupole coupling constant C. If we measure the energy splittings on the right hand side of eq. 6.13

Ω can be extracted. Just to be explicit we can write the following first order expression for the nuclear magnetic octupole moment in ^{137}Ba.

$$\Omega = \frac{-\frac{1}{80}\Delta E_0^{(3/2)} + \frac{1}{100}\Delta E_1^{(3/2)} - \frac{1}{400}\Delta E_2^{(3/2)}}{\left\langle \frac{3}{2}\frac{3}{2} \right| N_0^{(3)} \left| \frac{3}{2}\frac{3}{2} \right\rangle} \tag{6.14}$$

6.3.2 Second Order Corrections

Terms that arise from second order perturbation theory make significant contributions to the theoretically predicted value of C($5D_{3/2}$). We therefore need to consider second order terms that couple the $5D_{3/2}$ hyperfine sublevels to $5D_{5/2}$ hyperfine sublevels with the same angular momentum F as illustrated in figure 6.1.

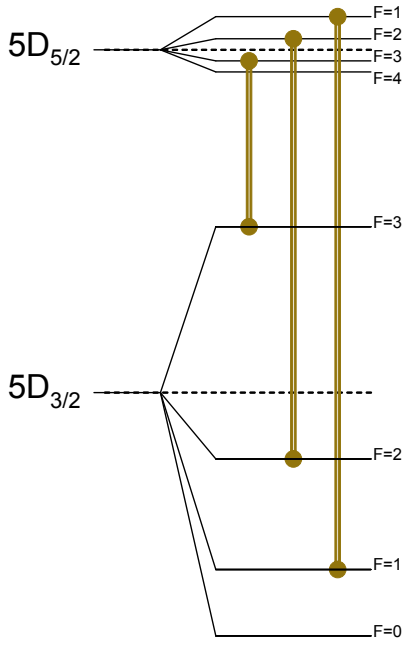

Figure 6.1: Second order perturbative corrections to the hyperfine energy sub-levels mix states with the same F and m_F but different values for J. The most significant mixings in the $5D_{3/2}$ level of $^{137}Ba^+$ are shown.

The most significant second order hyperfine contribution to the octupole coupling constant C($5D_{3/2}$) comes from the dipole-quadrupole interaction. Similar to the definition of

the coupling constants A, B and C, we let ζ be a constant with units of energy that sets the size of the second order hyperfine interaction that mixes the $5D_{3/2}$ level with the $5D_{5/2}$ level (see Appendix D for details). If we assume that the nuclear magnetic octupole moment of ^{137}Ba is of the magnitude predicted by the shell model, atomic theory calculations suggest that $C(5D_{3/2})$ would be approximately 23 Hz while the contribution due to ζ would be on the order of 1 Hz. The ζ contribution to $C(5D_{3/2})$ has been calculated so in principle we could simply correct the best fit value for $C(5D_{3/2})$ that results from our measurement of the $5D_{3/2}$ hyperfine splittings. However calculating ζ requires evaluating off diagonal matrix elements of the $5D_{3/2}$ and $5D_{5/2}$. The uncertainty on these types of calculations tends to be rather large so we would likely be forced to increase the the uncertainty on a final value for Ω. Alternatively, one could measure the hyperfine splittings of the $5D_{5/2}$ level as well to completely eliminate the dependence of $C(5D_{3/2})$ on ζ. The details of this second option can be found in [4].

6.4 Proposed Experimental Method

Here we review a procedure for measuring the hyperfine splittings in the $5D_{3/2}$ level of $^{137}Ba^{+}$. We then estimate the size of statistical and systematic errors.

6.4.1 Procedure

With the stability of the 2051 nm laser that we have demonstrated, it is conceivable that we could perform laser spectroscopy on the $5D_{3/2}$ level in ^{137}Ba with enough precision to determine $C(5D_{3/2})$. However in practice it will be easier to achieve the necessary level of precision by performing RF spectroscopy on the $5D_{3/2}$ levels. The 2051 nm laser still plays an important role in this experiment as it will be used to selectively populate Zeeman states in each of the $5D_{3/2}$ sublevels.

The energies of states with $m \neq 0$ have strong first order dependence on magnetic fields. To avoid these types of shifts we will measure the frequency of radiation required to couple one $m = 0$ state to another $m = 0$ state in an adjacent hyperfine sublevel. As demonstrated in Chapter 5 we can transfer ion population to the $5D_{3/2}$ level with $> 90\%$ efficiency using π pulses of 2051 nm light. The most obvious way to transfer an ion to an $m = 0$ state in

the $5D_{3/2}$ level is to optically pump the ion into the $6S_{1/2}$ $F = 2$ $m = 0$ state by driving the 493 nm $6S_{1/2}$ to $6P_{1/2}$ $\Delta m = 0$ transition as shown in figure 2.13(b) then drive the $6S_{1/2}$ to $5D_{3/2}$ $\Delta m = 0$ transition. This is the transition we have propsed for use as in a barium ion optical frequecny standard. However this transition is not currently available to us because the vacuum chamber that encloses the trap does not have the optical access necessary to both optically pump the ion and drive $\Delta m = 0$ electric quadrupole transitions (see section 4.3.7).

Fortunately there is a second option that should be easy to implement. If we optically pump the ion into the a stretched state of the $6S_{1/2}$ $F = 2$ sublevel (see figures 2.13(a) and 2.13(c))we can drive $6S_{1/2}$ to $5D_{3/2}$ $|\Delta m| = 2$ transitions into the $m = 0$ states of the $5D_{3/2}$ hyperfine sublevels. By aligning the 2051 nm beam perpendicular to the quantization axis and also setting the linear polarization of the beam to be perpendicular to the quantization access we ensure that we will only drive $|\Delta m| = 2$ electric quadrupole transitions. The optical access currently available to us is sufficient for such a scheme.

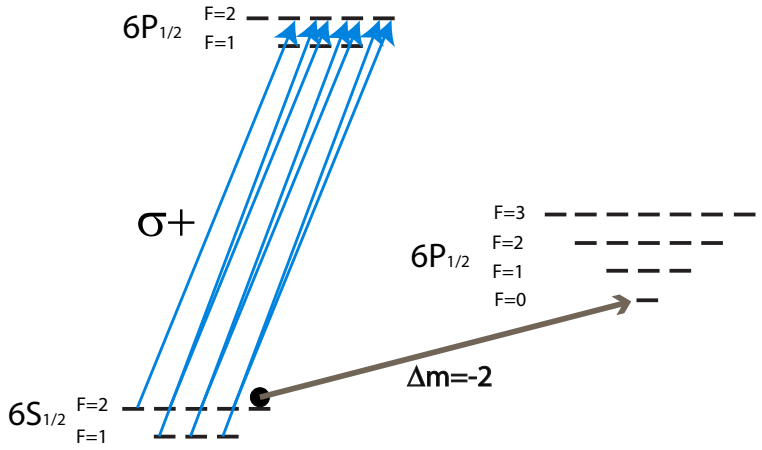

Figure 6.2: Suggested optical pumping and state preparation scheme for the ocutupole measurement.

Once the ion population has been transfered to an $m = 0$ state in the $5D_{3/2}$ level (for example $F = 0$ $m = 0$) we use a magnetic field oscillating at a radio frequency to attempt to transfer the ion population to the $F = 1$ $m = 0$ state via a magnetic dipole transition.

We can detect whether the magnetic dipole transition occurred by applying a π pulse of 2051 nm light, a shelving pulse of 455 nm light, then turning on the 493 nm and 650 nm lasers. If the magnetic dipole transition occurred the ion will be in the $F = 1$ $m = 0$ state 150 MHz away and the π pulse of 2051 nm light will have no effect. The ion will remain in the $5D_{3/2}$ level after the 455 nm shelving pulse and when the 493 nm and 650 nm lasers are turned back on the ion will fluoresce. If the magnetic dipole transition did not occur the ion will remain in the $F = 0$ $m = 0$ state and the π pulse of 2051 nm light will return the ion to the ground state. The shelving pulse will transfer the ion to the $5D_{5/2}$ level and when the 493 nm and 650 nm lasers are turned back on the ion will not fluoresce.

Once the frequency necessary to transfer the ion to one adjacent hyperfine sublevel is known we can adjust the RF pulse duration to drive π pulses. This will allow us the efficiently populate the $m = 0$ state of a different hyperfine sublevel without retuning the 2051 nm laser. The same technique can then be used to measure the next hyperfine frequency interval (e.g. $F = 1$ to $F = 2$) Detecting whether the second magnetic dipole transition occurred requires applying the sequence of pulses necessary to transfer the ion back to the $F = 0$ $m = 0$ state so the 2051 nm laser can return the ion to the ground state for shelving. In this way we can measure all three hyperfine frequency intervals in the $5D_{3/2}$ level.

Although this sequence of pulses may seem rather long and convoluted, each of the steps involved has been demonstrated with very high fidelity [57] [19]. In practice this pulse sequence will likely be easier to implement than retuning the 2051 nm laser to address different hyperfine sublevels.

6.4.2 Systematic Error and Statistical Uncertainty

To first order the energies of $m = 0$ states do not change with an applied magnetic field however they are shifted by the second-order Zeeman effect. Without knowing the magnitude of the applied magnetic field precisely these second order shifts will constitute the primary source of systematic error in our measurement of the $5D_{3/2}$ hyperfine structure. Fortunately the magnitude of these shifts can be determined in a straight forward way.

Equations 2.33 and 2.35 give expressions for the first and second order Zeeman shifts in terms of magnetic field strength (table 6.2 summarizes the magnitudes of these shifts in the $6S_{1/2}$ and $5D_{3/2}$ levels of $^{137}Ba^{+}$). If in addition to measuring $\Delta m = 0$ transitions we also measure $|\Delta m| = 1$ transitions the magnitude of the applied magnetic field can easily be determined as illustrated in figure 6.4. Once the field is known, the frequencies of the $\Delta m = 0$ transitions can be corrected.

State	Second-order shift for $m = 0$ (kHz/G^2)	First-order shift for $m \neq 0$ (kHz/G)
$6S_{1/2}F = 1$	-0.244	-701 m_F
$6S_{1/2}F = 2$	+0.244	702 m_F
$5D_{3/2}F = 0$	-10.789	-
$5D_{3/2}F = 1$	7.800	559 m_F
$5D_{3/2}F = 2$	2.989	559 m_F
$5D_{3/2}F = 3$	.917	559 m_F

Table 6.2: Magnetic field dependence of hyperfine sublevels in $^{137}Ba^{+}$ [55]

In its current configuration the ion trap is not magnetically shielded. It is likely that stray magnetic radiation due to nearby electronics is broadening all the linewidths we observe. Such broadening will increase the statistical error on our octupole measurements in two ways. First it will hinder our ability to fit for the center frequency of the observed RF transitions. Second it will increase the error on the measurements of the $|\Delta m| = 1$ RF transitions necessary to determine the magnitude of the applied magnetic field. In order to be conservative we will have to increase our estimate of the systematic error due to the second order Zeeman shift.

As discussed in chapter 5 to first order, the frequency of this transition depends on the magnitude of the external magnetic field in the following way

$$E' = \frac{1}{5}\mu_B B$$

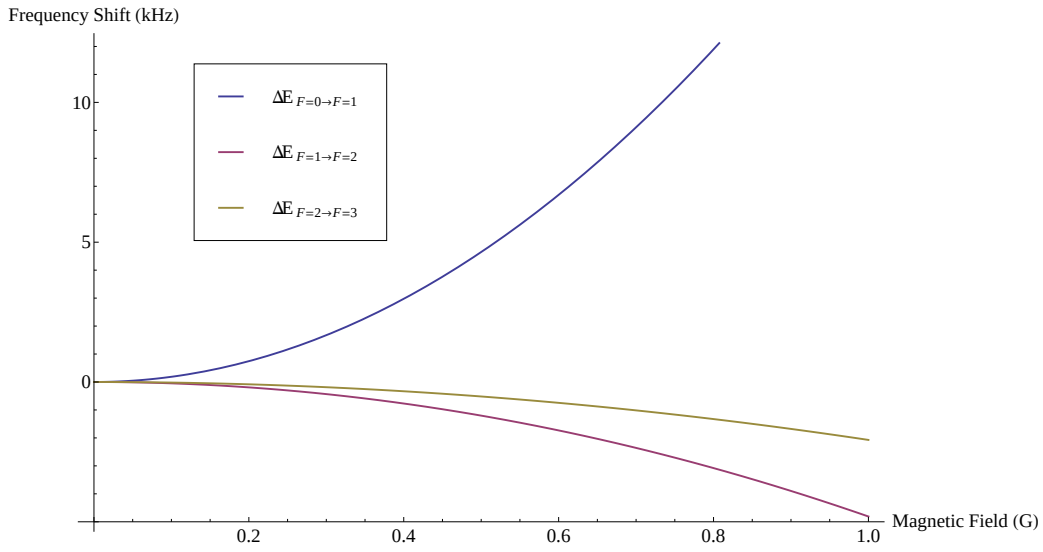

Figure 6.3: Second order Zeeman shifts represent the dominant source of systematic error for the measurement of the nuclear magnetic octupole moment. If one knows the strength of the laboratory field these shifts can be corrected for. The second order Zeeman shift to the three hyperfine splitting intervals in $^{137}Ba^{+}$ are plotted as a function of magnetic field strength.

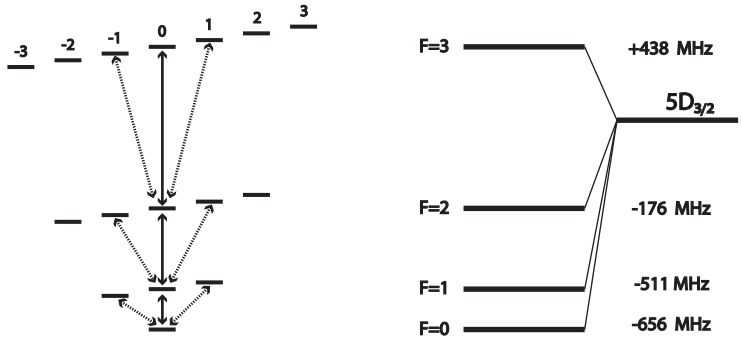

Figure 6.4: A drawing of the hyperfine and Zeeman structure in the $5D_{3/2}$ level of ^{137}Ba. The frequency of the $\Delta m_F = 0$ transitions will be measured to determine the hyperfine coupling constants. The $\Delta m_F = \pm 1$ transitions will be measured to determine the strength of the laboratory magnetic field.

. We can make estimates of the effect of magnetic field noise by assuming that the 700 Hz observed linewidth on the $m = 1/2$ to $m = 3/2$ 2051 nm transition (see figure 5.5) was due entirely to variations in the external magnetic field seen by the ion. The peak-to-peak amplitude of the magnetic field fluctuations that would result in a 700 variation in the center frequency of the 2051 nm transition are approximately 2.5 milligauss. Assuming we use a 1 gauss field to define an axis of quantization the second order Zeeman shift will broaden each of the $\Delta m = 0$ RF transitions to several tens of hertz. Let us take 50 Hz to be a conservative estimate of the $\Delta m = 0$ linewidths we will observe. In a typical one hour scan of an atomic feature we divide the spectrum into 40 bins and collect 50 data points per bin. Such a scan takes approximately one hour. With this amount of data we estimate that the linewidths of the $\Delta m = 0$ transitions would be .8 Hz and the linewidths of the $|\Delta m| = 1$ transitions would be about 25 Hz. This would lead to a combined statistical and systematic uncertainty on the octupole coupling constant of approximately 10 mHz.

Chapter 7

TOWARDS A BARIUM ION OPTICAL FREQUENCY STANDARD

After the completion of the measurement of the nuclear magnetic octupole moment of ^{137}Ba this apparatus will likely be converted into an optical frequency standard. Optical clockwork is an exciting field of research that is progressing very quickly. A the $6S_{1/2} \leftrightarrow 5D_{3/2}$ transition a single trapped ^{137}Ba ion possesses a number of features that make it an excellent candidate for use as the basis of a frequency standard. A thorough analysis of the suitability of $^{137}Ba^{+}$ as a frequency standard can be found in [55]. Here we present an general overview of optical atomic clocks and briefly review the primary advantages and disadvantages of the barium ion clock transition.

7.1 Atomic Clocks

Essentially a clock is a device that marks off regular intervals of time, combined with a means of counting the time intervals. A grandfather clock achieves this by coupling the 1 Hz oscillations of a pendulum to a system of gears that increment the hands on the clock face. Atomic clocks rely on a very different mechanism. A source of electromagnetic radiation is tuned to a frequency known to drive a particular atomic transition. The radiation source is then constantly re-tuned to stay on resonance with chosen transition. The oscillations of the electromagnetic field driving the atomic transition become the 'ticking' of the clock. In a cesium fountain frequency standard these oscillations occur at approximately 9 GHz and can be counted by a typical frequency counter.

It was long ago recognized that one could improve on the performance of the cesium frequency standard by driving a 'clock transition' with a laser rather than an RF source. However the electric field in a laser beam oscillates with a frequency on the order of 10^{15} Hz; much faster than any photodetector can respond. Complicated chains of lasers and RF oscillators were built to mix the an optical frequency down to a more convenient radio

frequency. All of this changed with the invention of the femtosecond frequency comb. Suddenly it was possible to convert an optical frequency into an RF frequency in a single step using equipment that could fit on a table top. Later this year the atomic physics group at the University of Washington will acquire such a frequency comb so let us review how it could be combined with the 2051 nm laser system to form a barium ion optical frequency standard. The system proposed here and illustrated in figure 7.3 is a modification of the mercury ion frequency standard currently in use at NIST [18].

7.2 Femtosecond Frequency Comb

A 'femtosecond frequency comb' is a particularly ingenious application of a mode-locked titanium-sapphire laser. We will not delve into the theory of operation behind these laser or mode locking as the subjects are covered in many books on laser physics ([44] for example). Instead we will simply state that the output of a titanium-sapphire laser is a periodic sequence of pulses. The duration of each pulse can be 100's of femtoseconds or as short as several femtoseconds. In frequency space, the power spectrum consists of many narrow peaks separated in frequency by the pulse repetition rate f_r. This frequency is often on the order of 1 GHz and can be fine tuned by controlling the round trip path length of the lasing cavity with a PZT. A circuit known as a phase locked loop (PLL) can keep the repetition rate locked to a some integer ratio of a frequency provided an different oscillator thus fixing the repetition rate and mode space to a known value.

The regular pattern of modes that one finds in the spectrum of a mode-locked titanium-sapphire laser does not continue all the way down to DC. Typically at wavelengths below 700 nm and above 1100 nm the gain provided by the titanium-sapphire crystal is insufficient for lasing to occur and the power spectrum tapers off. If the modes were were to extend down to zero frequency we would find that the first mode occurs at a frequency that is less than the repetition rate. This frequency is sometimes known as the 'carrier envelope offset' which we will label f_0. While the spacing of the modes in frequency space is fixed by the repetition rate, f_0 is in general unknown and unstabilized.

If the frequencies of the modes in the titanium-sapphire laser span an octave (i.e. the frequency of the highest frequency mode is twice the frequency of one of the lower frequency

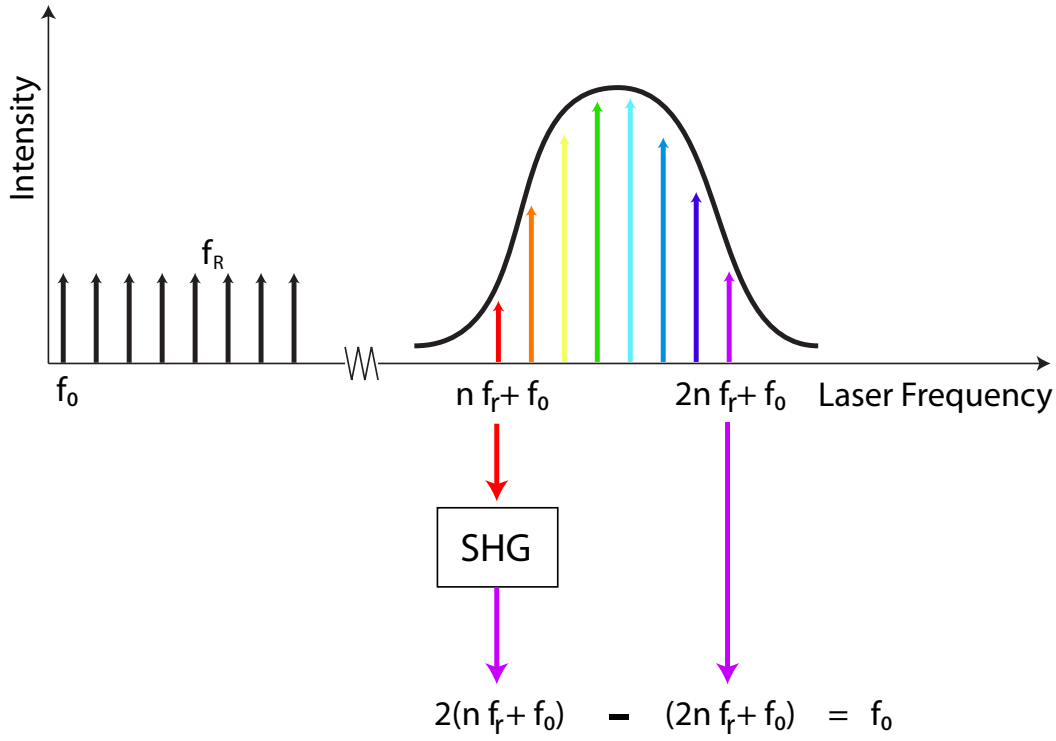

Figure 7.1: The carrier envelope offset f_0 of an octave spanning femtosecond pulse laser can be measured by frequency doubling light at the long wavelength end of the laser spectrum and comparing it to light at the short wave length end of the spectrum.

modes, neglecting the carrier envelope offset) f_0 can be determined using a technique illustrated in figure 7.1. Using a dichroic beam splitter light from the lower end of the titanium-sapphire's spectrum is split off from the output beam and frequency doubled using a non-linear crystal. The doubled light is then mixed back together with the original beam and the resulting interference signal is sent through a low pass filter which passes only the lowest frequency component of the signal. When a mode with frequency

$$f = nf_r + f_0$$

is frequency doubled its frequency becomes

$$2f = 2(nf_r + f_0)$$

. This mode will interfere with a mode with a frequency

$$f' = 2nf_r + f_0$$

the difference between these to signals is f_0. Once the carrier envelope offset f_0 is measured it can be stabilized using a second PLL. A correction signal is typically applied to the power of the laser pumping the titanium-sapphire laser.

Once f_r and f_0 are known and stabilized the frequency of each mode in the laser is known and has the stability of the RF oscillator referencing the PLL's. The frequency comb can then be used for metrology. The frequency of any other laser whose wavelength lies in the range covered by the comb can now be measured precisely. A wavemeter can be used to roughly determine the frequency of the laser to within approximately 100 MHz. This should be sufficient to determine the mode number of the nearest mode in the comb. By observing the beat frequency that results from the interference between the laser to be measured and the output of the comb one determines the remaining component of the frequency. How this process might be used to measure the frequency of the 2051 nm transition in barium is illustrated in figure 7.2.

With a few more modifications this apparatus becomes a frequency standard. With the 2051 nm laser locked to the ULE cavity it should be possible to push the instability in the laser down to one part in 10^{15}. It is possible to design a feedback loop that keeps

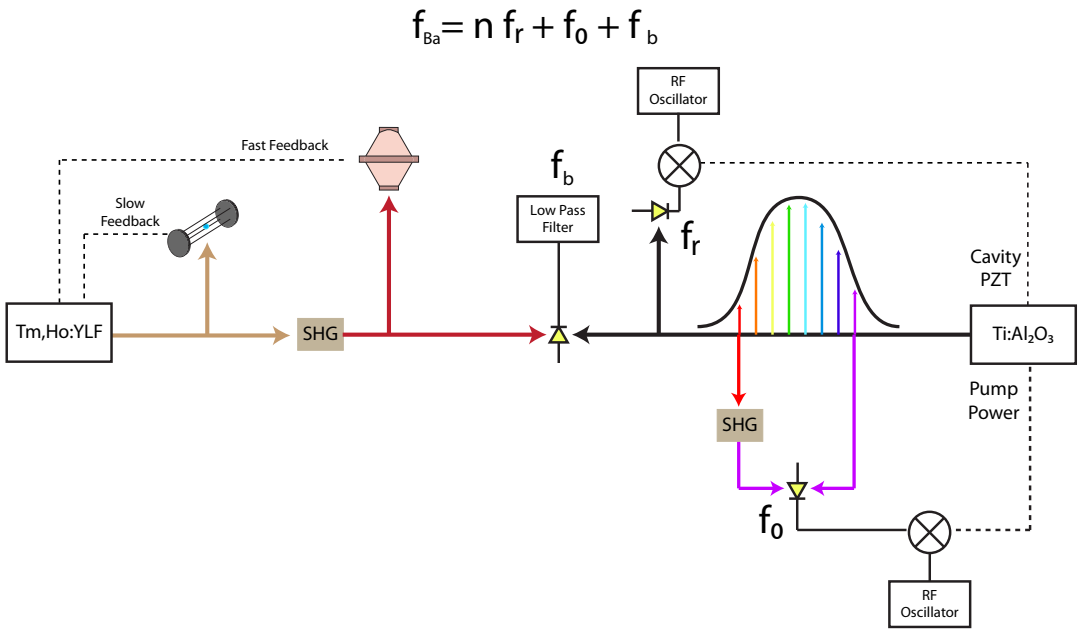

Figure 7.2: The frequency of the 2051 nm laser can be measured using an octave spanning femtosecond frequency comb.

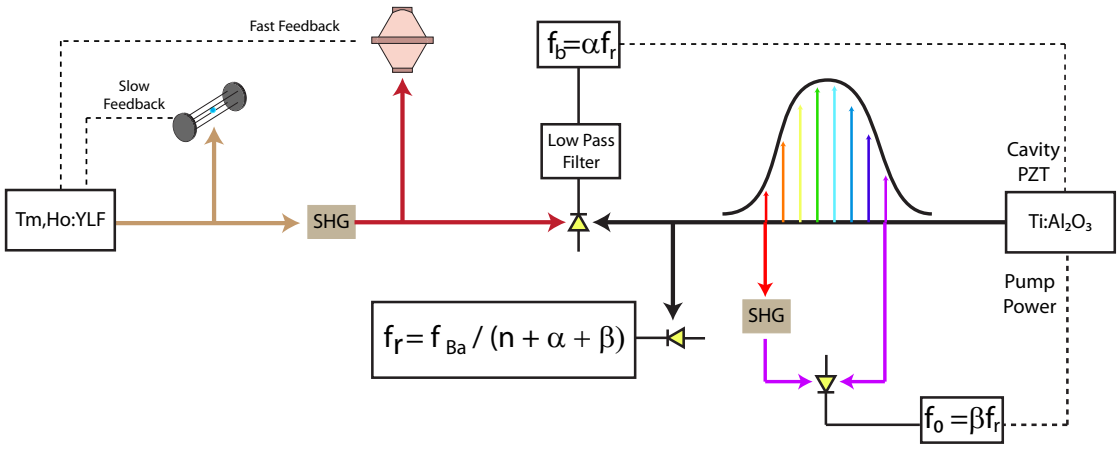

Figure 7.3: A barium ion optical frequency standard can be realized by locking the frequency of the frequency doubled 1025 nm beam to the output of an octave spanning femtosecond frequency comb.

the 2051 nm laser tuned to the center frequency of the $6S_{1/2}$ to $5D_{3/2}$ transition. In this setup the 2051 nm laser would have the short-term stability of the ULE reference cavity and a longterm stability determined by the time that elapses between measurements of the $6S_{1/2} \leftrightarrow 5D_{3/2}$ transition.

A portion of the frequency doubled 1025 nm light is then diverted to the frequency comb (one could use 2051 nm light although the comb would have to be specifically designed to operate at this wavelength). The 1025 nm beam is interfered with the output of the comb in the usual way to produce a beat signal. The crucial difference between this and the previous setup is that the comb is 'self-referenced'.

To self-reference a frequency comb one chooses a convenient frequency for the repetition rate f_r (say 1 GHz). We then use the repetition rate of the comb to stabilize the oscillators that are used to measure the f_0 and the beat note between the comb and the clock laser. Many commercially available RF synthesizers can be referenced to an externally generated 10 MHz signal. If we observe the 1 GHz output from the comb using a fast photodetector we can generate a 10 MHz signal with 1/100 radio frequency divider.

The carrier envelope offset is determined using same method described earlier. In this case however the PLL that servos the pump power is referenced by the 10 MHz signal from the comb. The PLL locks f_0 to an integer fraction β of the repetition rate f_r. A second PLL, also referenced to f_r locks the beat frequency f_b to an integer fraction α of the repetition rate. With both the repetition rate and the carrier envelope offset are referenced to the 2051 nm laser, the stability of the barium clock laser is transfered to each mode in the laser output which can be used to perform other laser metrology measurements. Best of all, the 1 GHz repetition rate f_r possesses all the stability of the clock laser and can be used for timekeeping.

7.3 Barium Ions for Clock Work - Systematic Error and Limits on Clock Instabilities

Optical frequency standards have been improving at a remarkable rate. The standards in operation at NIST have relative instabilities on the order of one part in 10^{-17} and it is expected that this can be improved to 10^{-18}. While barium ions have a number of features

that make them well suited for clock work they also have their own set of challenges.

7.3.1 Quadrupole Stark Shift

While careful nulling of external fields allows for the confinement of a trapped ion in a nearly field free region of space, it is unavoidable that electric field gradients will be present in the trapping region. These gradients will couple to the dipole moment of the atom and shift the energies of levels with sufficient angular momentum. In the mercury ion frequency standard at NIST these shifts enter at the 1 Hz level [33]. By averaging the center frequency of the clock transition in mercury over three orthogonal orientations of the laboratory magnetic field this shift is averaged to zero [33] [47]. Fortunately for us such a complicated scheme will not be necessary. One of the primary advantages of a barium ion frequency standard is that the quadrupole Stark shift is zero. This is because the first order shift of an electric quadrupole operator on a state $|JIFm_F\rangle$ is proportional to a six-J symbol $\left\{ \begin{array}{ccc} J & 2 & J \\ F & I & F \end{array} \right\}$ which evaluates to zero for both the F=0 and the F=2 sublevels of the $5D_{3/2}$ level in $^{137}Ba^{+}$.

7.3.2 Second-Order Black Body Stark Shift

The most troubling systematic effect in a ^{137}Ba ion frequency standard is the second order Stark shift resulting from black body radiation. The dipole Stark effect operator has odd parity and can only connect states with differing parity. Therefore we can take the first order shift from this operator to be zero. To second order it can be shown that this Stark shift can be decomposed into a scalar and a tensor component.

$$E' = -\frac{1}{2}\alpha_{scalar}(\gamma, J)E^2 - \frac{1}{4}\alpha_{tensor}(\gamma, J)\frac{3m_F^2 - F(F+1)}{F(2F-1)}(3E_z^2 - E^2) \tag{7.1}$$

where the scalar polarizability α_{scalar} is given by

$$\alpha_{scalar} = \frac{4\pi\epsilon_0 e^2\hbar^2}{m_e}\sum_{\gamma' J'}\frac{f_{\gamma J\gamma' J'}}{E_{\gamma' J'} - E_{\gamma J}} \tag{7.2}$$

The factors $f_{\gamma J\gamma' J'}$ are the oscillator strengths between the levels $|\gamma J\rangle$ and $|\gamma' J'\rangle$ and are proportional to the square of the matrix element of the electron position operator in between these states $\langle\gamma' J'|\, r\,|\gamma J\rangle$. Using measured values for these matrix elements found in the

literature it was estimated that the magnitude of the second-order Stark shift on the 2051 nm transition in barium would be [55]

$$\Delta E = 9.3E^2 \frac{\text{mHz}}{\left(\frac{\text{V}}{\text{cm}}\right)^2}$$

Fortunately for us the tensor polarizability α_{tensor} proportional to a six-J symbol which evaluates to zero for F=0, 1, 2, and 3 in the $5D_{3/2}$ level of $^{137}Ba^{+}$.

$$\begin{aligned}
\alpha_{tensor} &\sim \left\{ \begin{array}{ccc} F & J & I \\ J & F & 2 \end{array} \right\} \\
&= \left\{ \begin{array}{ccc} F & \frac{3}{2} & \frac{3}{2} \\ \frac{3}{2} & F & 2 \end{array} \right\} \\
&= 0
\end{aligned}$$

The spectral power density of black body radiation as a function of wavelength λ and temperature T has the following form [9].

$$\rho(\lambda, T) = \frac{8\pi hc}{\lambda^5} \frac{1}{e^{\frac{hc}{\lambda kT}} - 1} \tag{7.3}$$

At room temperature the magnitude of the electric field due to black body radiation is 8.319 V/cm which shifts the center frequency of the 2051 nm transition by approximately 640 mHz. A constant shift of the center frequency of a clock's oscillator is not necessarily a problem. However there is uncertainty on the order of 5% in the knowledge of the relavent matrix elements. This uncertainty when included as a source of instability in a barium ion clock limits the instability to approximately 1×10^{-16}. The total emissive power of a black body scales with temperature as T^4. By running the experiment at the temperature of liquid nitrogen the black body limit on clock instability drops to approximately 1×10^{-18}.

BIBLIOGRAPHY

[1] J. Lloyd Armstrong. *Theory of the Hyperfine Structure of Free Atoms.* Willey-Interscience, New York, 1971.

[2] O. H. Arroe. Hyperfine structure and isotope shift in barium. *Phys. Rev.*, 79(5):836–838, Sep 1950.

[3] Claude Audoin and Bernard Guinot. *The Measurement of Time: Time Frequency and the Atomic Clock.* Cambridge University Press, 2001.

[4] K. Beloy, A. Derevianko, V. A. Dzuba, G. T. Howell, B. B. Blinov, and E. N. Fortson. Nuclear magnetic octupole moment and the hyperfine structure of the $5d_{3/2,5/2}$ states of the ba^+ ion. *Phys. Rev. A*, 77(5):052503, May 2008.

[5] K. Beloy, A. Derevianko, and W. R. Johnson. Hyperfine structure of the metastable $^3p_2$ state of alkaline-earth-metal atoms as an accurate probe of nuclear magnetic octupole moments. *Phys. Rev. A*, 77(1):012512, Jan 2008.

[6] D. J. Berkeland, J. D. Miller, J. C. Bergquist, W. M. Itano, and D. J. Wineland. Minimization of ion micromotion in a paul trap. *Journal of Applied Physics*, 83(10):5025–5033, 1998.

[7] R. et. al. Blatt. Realization of the ciraczoller controlled-not quantum gate. *Nature*, 422(22):408–411, March 2003.

[8] Marie-Anne Bouchiat and Claude Bouchiat. Parity violation in atoms. *Reports on Progress in Physics*, 60(11):1351, 1997.

[9] B.H. Bransden and C.J. Joachain. *Quantum Mechanics.* Prentice Hall, 2000.

[10] T. Brenner, S. Bttgenbach, W. Rupprecht, and F. Trber. Nuclear moments of the low abundant natural isotope 176lu and hyperfine anomalies in the lutetium isotopes. *Nuclear Physics A*, 440(3):407 – 423, 1985.

[11] Howard Howland Brown and John G. King. Hyperfine structure and octopole interaction in stable bromine isotopes. *Phys. Rev.*, 142(1):53–59, Feb 1966.

[12] Dmitry Budker, Derek Kimball, and David Demille. *Atomic physics: An exploration through problems and solutions.* OUP Oxford, November 2003.

[13] W. J. Childs. M1, e2, and m3 hyperfine structure and nuclear moment ratios for ^{151,153}eu. *Phys. Rev. A*, 44(3):1523–1530, Aug 1991.

[14] W. J. Childs, O. Poulsen, L. S. Goodman, and H. Crosswhite. Laser-rf double-resonance studies of the hyperfine of ^{51}v. *Phys. Rev. A*, 19(1):168–176, Jan 1979.

[15] C Cohen-Tannoudji and S Reynaud. Dressed-atom description of resonance fluorescence and absorption spectra of a multi-level atom in an intense laser beam. *Journal of Physics B: Atomic and Molecular Physics*, 10(3):345, 1977.

[16] R. T. Daly and J. H. Holloway. Nuclear magnetic octupole moments of the stable gallium isotopes. *Phys. Rev.*, 96(2):539–540, Oct 1954.

[17] Ralph G. DeVoe and Christian Kurtsiefer. Experimental study of anomalous heating and trap instabilities in a microscopic ^{137}ba ion trap. *Phys. Rev. A*, 65(6):063407, Jun 2002.

[18] S. A. Diddams, Th. Udem, J. C. Bergquist, E. A. Curtis, R. E. Drullinger, L. Hollberg, W. M. Itano, W. D. Lee, C. W. Oates, K. R. Vogel, and D. J. Wineland. An optical clock based on a single trapped 199hg+ ion. *Science*, 293(5531):825–828, 2001.

[19] M. R. Dietrich, N. Kurz, T. Noel, G. Shu, and B. B. Blinov. Hyperfine and optical barium ion qubits. *Phys. Rev. A*, 81(5):052328, May 2010.

[20] R. W. P. Drever, J. L. Hall, F. V. Kowalski, J. Hough, G. M. Ford, A. J. Munley, and H. Ward. Laser phase and frequency stabilization using an optical resonator. *Applied Physics B: Lasers and Optics*, 31(2):97–105, June 1983.

[21] T. G. Eck and P. Kusch. Hfs of the $5^2p_{\frac{3}{2}}$ state of in^{115} and in^{113}: Octupole interactions in the stable isotopes of indium. *Phys. Rev.*, 106(5):958–964, Jun 1957.

[22] T. Y. Fan, R. L. Byer, G. Huber, and P. Mitzscherlich. Spectroscopy and diode laser-pumped operation of Tm, Ho:YAG. *IEEE Journal of Quantum Electronics*, 24:924–933, June 1988.

[23] G. Floquet. Observation of population inversion by optical adiabatic rapid passage. *Annales scientifiques de l'Ecole Normale Superieure*, 2(12):47–88, 1883.

[24] Christopher J. Foot. *Atomic Physics (Oxford Master Series in Atomic, Optical and Laser Physics)*. Oxford University Press, USA, February 2005.

[25] Norval Fortson. Possibility of measuring parity nonconservation with a single trapped atomic ion. *Phys. Rev. Lett.*, 70(16):2383–2386, Apr 1993.

[26] G. Marx, G. Tommaseo, and G. Werth. Precise $\backslash sfg\_j$- and $\backslash sfg\_i$-factor measurements of ba^+ isotopes. *Eur. Phys. J. D*, 4(3):279–284, 1998.

[27] Alan Gallagher. Oscillator strengths of ca ii, sr ii, and ba ii. *Phys. Rev.*, 157(1):24–30, May 1967.

[28] G. Galzerano, M. Marano, S. Longhi, E. Sani, A. Toncelli, M. Tonelli, and P. Laporta. Sub-100-ps amplitude-modulation mode-locked tm–ho:bay2f8 laser at 2.06 μm. *Opt. Lett.*, 28(21):2085–2087, 2003.

[29] V. Gerginov, C. E. Tanner, and W. R. Johnson. Observation of the nuclear magnetic octupole moment of ^{87}Rb from spectroscopic measurements of hyperfine intervals. *Canadian Journal of Physics*, 87:101–104, 2009.

[30] Vladislav Gerginov, Andrei Derevianko, and Carol E. Tanner. Observation of the nuclear magnetic octupole moment of cs133. *Phys. Rev. Lett.*, 91(7):072501, Aug 2003.

[31] D. Hanneke, S. Fogwell, and G. Gabrielse. New measurement of the electron magnetic moment and the fine structure constant. *Phys. Rev. Lett.*, 100(12):120801, Mar 2008.

[32] T.W. Hansch and B. Couillaud. Laser frequency stabilization by polarization spectroscopy of a reflecting reference cavity. *Optics Communications*, 35(3):441 – 444, 1980.

[33] Wayne Itano. External-field shifts of the 199 hg+ optical frequency standard. *Journal of Research of NIST*, 105(6):829–837, 2000.

[34] John David Jackson. *Classical electrodynamics*. Wiley, New York, NY, 3rd ed. edition, 1999.

[35] W. G. Jin, M. Wakasugi, M. G. Hies, T. T. Inamura, T. Murayama, T. Ariga, A. Yamashita, T. Wakui, H. Katsuragawa, T. Ishizuka, J. Z. Ruan, and I. Sugai. Nuclear moments and charge radius of ^{175}hf from optical measurement of hyperfine structure. *Phys. Rev. C*, 55(3):1545–1547, Mar 1997.

[36] K. H. Knöll, G. Marx, K. Hübner, F. Schweikert, S. Stahl, Ch. Weber, and G. Werth. Experimental g_J factor in the metastable $5d_{3/2}$ level of ba^+. *Phys. Rev. A*, 54(2):1199–1205, Aug 1996.

[37] H. KOGELNIK and T. LI. Laser beams and resonators. *Appl. Opt.*, 5(10):1550–1567, Oct 1966.

[38] N. Kurz, M. R. Dietrich, Gang Shu, R. Bowler, J. Salacka, V. Mirgon, and B. B. Blinov. Measurement of the branching ratio in the $6p_{3?2}$ decay of *baii* with a single trapped ion. *Phys. Rev. A*, 77(6):060501, Jun 2008.

[39] Donald A. Landman and Allen Lurio. Hyperfine structure of the $(6p)^3$ configuration of bi^{209}. *Phys. Rev. A*, 1(5):1330–1338, May 1970.

[40] P. Laporta, M. Marano, L. Pallaro, and S. Taccheo. Amplitude and frequency stabilisation of a tm-ho:yag laser for coherent lidar applications at 2.1μm. *Optics and Lasers in Engineering*, 37(5):447 – 457, 2002.

[41] Michael M. T. Loy. Observation of population inversion by optical adiabatic rapid passage. *Phys. Rev. Lett.*, 32(15):814–817, Apr 1974.

[42] M. Marano, P. Laporta, A. Sapia, and P. De Natale. Absolute frequency stabilization of a tunable tm:ho:yag laser to the hbr p(12) line at 2097 nm. *Opt. Lett.*, 25(23):1702–1704, 2000.

[43] Harold J. Metcalf and Peter van der Straten. *Laser Cooling and Trapping (Graduate Texts in Contemporary Physics)*. Springer, November 2001.

[44] Warren Nagourney. *Quantum Electronics for Atomic Physics*. Oxford University Press, 2010.

[45] Warren Nagourney, Jon Sandberg, and Hans Dehmelt. Shelved optical electron amplifier: Observation of quantum jumps. *Phys. Rev. Lett.*, 56(26):2797–2799, Jun 1986.

[46] Mark Notcutt, Long-Sheng Ma, Jun Ye, and John L. Hall. Simple and compact 1-Hz laser system via an improved mounting configuration of a reference cavity. *Opt. Lett.*, 30(14):1815–1817, 2005.

[47] W. H. Oskay, W. M. Itano, and J. C. Bergquist. Measurement of the $^{199}hg^+$ $5d^9 6s^2\ ^2d_{5/2}$ electric quadrupole moment and a constraint on the quadrupole shift. *Phys. Rev. Lett.*, 94(16):163001, Apr 2005.

[48] John D. Prestage, Robert L. Tjoelker, and Lute Maleki. Atomic clocks and variations of the fine structure constant. *Phys. Rev. Lett.*, 74(18):3511–3514, May 1995.

[49] Giulio Racah. Theory of complex spectra. ii. *Phys. Rev.*, 62(9-10):438–462, Nov 1942.

[50] Fritz Riehle. *Frequency Standards: Basics and Applications*. Wiley-VCH, 1 edition, January 2005.

[51] T. Rosenband, P. O. Schmidt, D. B. Hume, W. M. Itano, T. M. Fortier, J. E. Stalnaker, K. Kim, S. A. Diddams, J. C. J. Koelemeij, J. C. Bergquist, and D. J. Wineland. Observation of the $^1s_0 \rightarrow\ ^3p_0$ clock transition in $^{27}al^+$. *Phys. Rev. Lett.*, 98(22):220801, May 2007.

[52] J. J. Sakurai. *Modern Quantum Mechanics (Revised Edition)*. Addison Wesley, rev sub edition, September 1993.

[53] Charles Schwartz. Theory of hyperfine structure. *Phys. Rev.*, 97(2):380–395, Jan 1955.

[54] R. Shankar. *Principles of Quantum Mechanics*. Springer, September 1994.

[55] J. A. Sherman. Single barium ion spectroscopy: light shifts, hyperfine structure, and progress on an optical frequency standard and atomic parity violation. *ArXiv e-prints*, July 2009.

[56] J. A. Sherman. Single barium ion spectroscopy: light shifts, hyperfine structure, and progress on an optical frequency standard and atomic parity violation. *ArXiv e-prints*, July 2009.

[57] J. A. Sherman, A. Andalkar, W. Nagourney, and E. N. Fortson. Measurement of light shifts at two off-resonant wavelengths in a single trapped ba^+ ion and the determination of atomic dipole matrix elements. *Phys. Rev. A*, 78(5):052514, Nov 2008.

[58] Jeff A. Sherman, William Trimble, Steven Metz, Warren Nagourney, and Norval Fortson. Progress on indium and barium single ion optical frequency standards, 2005.

[59] Bruce Shore. *The Theory of Coherent Atomic Excitation*. John Wiley & Sons, 1990.

[60] Gang Shu. *Novel Ion Traps for Enhanced Fluorescence Collections and Single Photon Sources Based on Barium Ions*. PhD thesis, University of Washington, 2010.

[61] Roger E. Silverans, Gustaaf Borghs, Peter De Bisschop, and Marleen Van Hove. Hyperfine structure of the $5d^2d_j$ states in the alkaline-earth ba ion by fast-ion-beam laser-rf spectroscopy. *Phys. Rev. A*, 33(3):2117–2120, Mar 1986.

[62] D. G. Smith. Magnetic multipoles in theory and practice. *American Journal of Physics*, 48(9):739–745, 1980.

[63] A. V. Steele, L. R. Churchill, P. F. Griffin, and M. S. Chapman. Photoionization and photoelectric loading of barium ion traps. *Phys. Rev. A*, 75(5):053404, May 2007.

[64] Will Trimble. *High-resolution spectroscopy in 5In? and prospects for an indium ion optical frequency reference*. PhD thesis, University of Washington, 2007.

[65] M. Van Hove, G. Borghs, P. De Bisschop, and R. E. Silverans. Hyperfine structure of $5d^2d_{3/2}^{135,137}$ ba ions by collinear fast beam laser-rf double resonance spectroscopy. *Zeitschrift fr Physik A Hadrons and Nuclei*, 321:215–219, 1985. 10.1007/BF01493440.

[66] P Villemoes, A Arnesen, F Heijkenskjold, and A Wannstrom. Isotope shifts and hyperfine structure of 134-138 ba ii by fast ion beam-laser spectroscopy. *Journal of Physics B: Atomic, Molecular and Optical Physics*, 26(22):4289, 1993.

[67] K. Wendt, S. A. Ahmad, F. Buchinger, A. C. Mueller, R. Neugart, and E. W. Otten. Relativistic j-dependence of the isotope shift in the 6s-6p doublet of ba ii. *Zeitschrift fr Physik A Hadrons and Nuclei*, 318:125–129, 1984. 10.1007/BF01413460.

[68] G.K. Woodgate. *Elementary Atomic Structure*. Oxford University Press, 1980.

[69] X. Zhao, N. Yu, H. Dehmelt, and W. Nagourney. Isotope-shift measurement of the 6 $^2s_{1/2}$–5 $^2d_{5/2}$ transition in ba^+. *Phys. Rev. A*, 51(6):4483–4486, Jun 1995.

Appendix A

ERROR SIGNAL

In this appendix we review two methods of generating error signals used in the work described in this thesis.

A.1 Hansch-Couilluad Polarization Scheme

Let us briefly summarize the Hansch-Couillaud stabilization scheme. By analyzing the polarization of the light reflected off the input cavity one can derive an error signal suitable for locking to the top of a cavity mode without resorting to any modulation techniques. The setup is as follows. The incident light is linearly polarized so the amplitude of the electric field can be written using the Jones calculus [44] as

$$E^{inc} = \begin{pmatrix} E_H^{inc} \\ E_V^{inc} \end{pmatrix}$$

The light reflected off a the input coupler of this cavity is a superposition of a promptly reflected beam and light that leaks through the input coupler after circulating inside the cavity. On resonance these two beams interfere and the rejected beam is minimized. If the intensity transmission coefficient $T = 1 - R$ for the input coupler is equal to all other cavity losses, excluding the input coupling, the cavity is said to be impedance matched [44]. For the purposes of this discussion let us assume that this condition is satisfied since it simplifies the math. Under this condition the intensity of the light circulating inside the cavity is at a maximum and the intensity of the rejected beam goes to zero on resonance. The electric field in the rejected beam can be written in terms of the electric field in the incident beam.

$$\begin{aligned} E^{rej} = E^{inc}F(\omega)F(\omega) \qquad & \\ = \frac{r(e^{i\phi} - 1)}{1 - r^2 e^{i\phi}} & \end{aligned} \tag{A.1}$$

where ϕ is the phase that the light would accumulate over one round trip in the cavity which can be written in terms of the free spectral range of the cavity as $\phi = \frac{\omega}{FSR}$ and r is the reflectivity of a cavity mirror.

Brewster cutting the nonlinear crystal inside the cavity or including a Brewster window in the beam path ruins the cavity finesse for one linear polarization (we will take this to be the horizontal polarization). Light with horizontal polarization that enters the cavity is strongly and only the vertically polarized component of the rejected beam experiences the phase shift described in eq. A.1. We can write the following.

$$E_H^{rej} = E_H^{inc}\sqrt{R}$$
$$E_V^{rej} = E_V^{inc}F(\omega)$$

The rejected beam is passed through a quarter waveplate then a polarizing beam splitter. In the Jones calculus the electric field of the beams in the two outputs of the PBS can be written as

$$E_{a,b} = \frac{1}{2}\begin{pmatrix} 1 & \pm 1 \\ \pm 1 & 1 \end{pmatrix}\begin{pmatrix} 0 & 1 \\ 1 & 0 \end{pmatrix}\begin{pmatrix} E_H^{rej} \\ E_V^{rej} \end{pmatrix} \tag{A.2}$$

The intensity of the light seen at the two outputs of the PBS is monitored with photo-diodes. The Hansch-Couillaud error signal is given by the difference between the photo-currents in each photo-diode. A plot of this error signal is shown in figure A.1.

A.2 Pound-Drever-Hall Frequency Stabilization

The PDH technique is a way to achieve a high bandwidth lock to an optical reference cavity. The technique begins with frequency or phase modulating of the laser beam sent to the reference cavity. If E_{inc} is the amplitude of the electric field in the incident laser beam whose frequency is ω and the frequency and depth of modulation are Ω and β we can write

$$\begin{aligned} E_{inc} &= E_0 e^{(i\omega t + \beta \sin \Omega t)} \\ &= E_0 e^{i\omega t}\left(J_0\beta + \sum_{k=1}^{\infty} J_k(\beta)e^{ik\Omega t} + \sum_{k=1}^{\infty}(-1)^k J_k(\beta)e^{-ik\Omega t}\right) \\ &\approx E_0\left(J_0(\beta)e^{i\omega t} + J_1(\beta)e^{i(\omega+\Omega)t} - J_1(\beta)e^{i(\omega-\Omega)t}\right) \end{aligned} \tag{A.3}$$

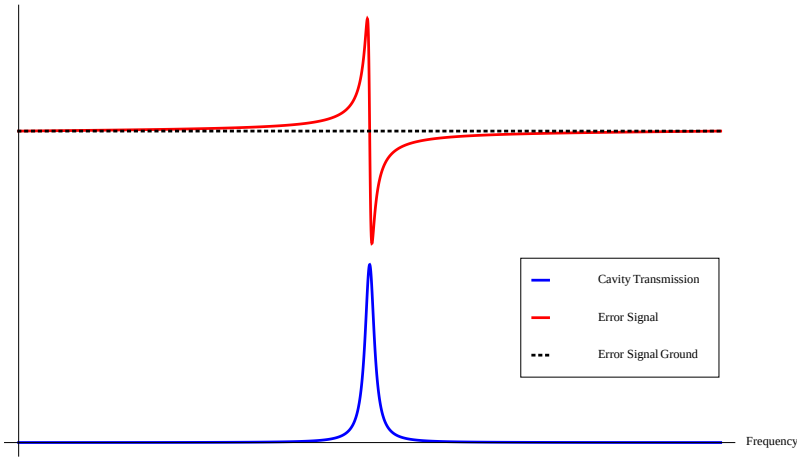

Figure A.1: The lineshape of the error signal derived using the polarization method described in the text.

For small modulation depths the beam has three components, an unmodulated carrier and sidebands at $\omega + \Omega$ and $\omega - \Omega$. Note that amplitude modulation sidebands will not have the necessary phase relationship to the carrier for this method. The modulated light is then sent to the reference cavity.

So far this setup is no different then more simple 'dither' locking schemes where the frequency (or phase) of the laser is modulated causing the intensity of the light transmitted through the cavity to oscillate at the modulation frequency. The phase of the intensity oscillations on the transmitted signal depend on whether the laser is tuned above or below and the the cavity resonance. Comparing these oscillations to the original modulating signal using a lock-in amplifier is a simple yet effective way to generate an error signal for laser frequency stabilization.

Such a scheme does not work for locking to cavities with transmission linewidths less than 100 kHz. The reason becomes apparent if one looks at things in the frequency domain. Suppose the carrier frequency was tuned to a cavity mode. If the modulation frequency is greater than the linewidth of the cavity, then the sidebands will be rejected and only the power contained in the carrier will be transmitted (figure A.2(a). The transmitted light is

unmodulated thus making it impossible to derive an error signal. One solution (shown in figure A.2(b)) would be to make the modulation frequency less than the cavity linewidth so that the modulation could be detected after the cavity. This leads to a very low bandwidth lock that usually cannot keep the laser frequency stable enough to maintain a lock to a narrow cavity mode.

The PDH method provides a solution to this problem. Rather than monitor the intensity of the transmitted signal, in the PDH method one monitors the intensity of the rejected beam. At first thought this may seem strange. This light never enters the cavity so why would it contain any information about the cavity modes? Using eq. A.1 We can write an expression for the electric field in the reflected beam as

$$E_{ref} = E_0 \left(F(\omega) J_0(\beta) e^{i\omega t} + F(\omega+\Omega) J_1(\beta) e^{i(\omega+\Omega)t} - F(\omega-\Omega) J_1(\beta) e^{i(\omega-\Omega)t} \right) \qquad \text{(A.4)}$$

The intensity of the beam, given by the square of equation A.4 can be written as a sum of terms proportional to $\cos\Omega t$, $\sin\Omega t$, $\cos 2\Omega t$, $\sin 2\Omega t$, and so on. The PDH error signal is contained in the amplitude of the $\sin\Omega t$ term which can be extracted using a frequency mixer. A plot of the PDH error signal and the transmission through the cavity of frequency modulated beam is shown in figure A.3. Because the error signal is derived from the reflected beam the modulation frequency can in principle be made arbitrarily high which allows for much greater feedback bandwidths.

The error signals at the frequencies where the sidebands are resonant with the cavity transmission mode. These error signals are of the opposite phase for stable locking so they do not interfere with the lock performance.

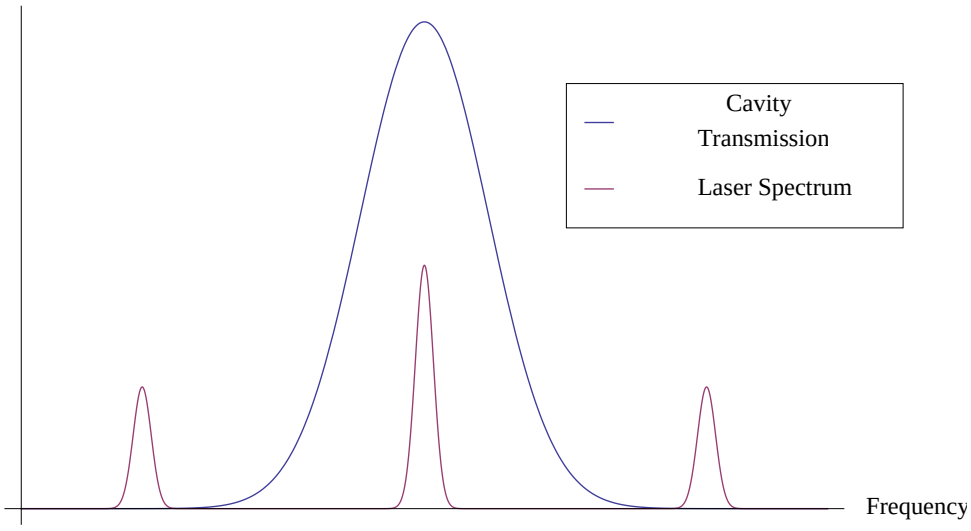

(a)

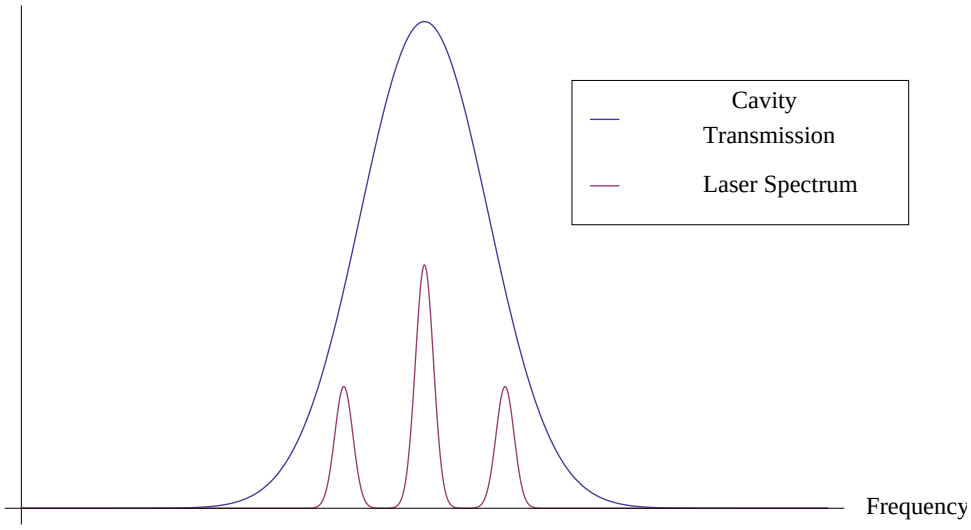

(b)

Figure A.2: If the frequency of the sidebands is less than the linewidth of the cavity transmission mode modulation can be observed in the transmitted signal. The PDH method allows for higher frequency modulation.

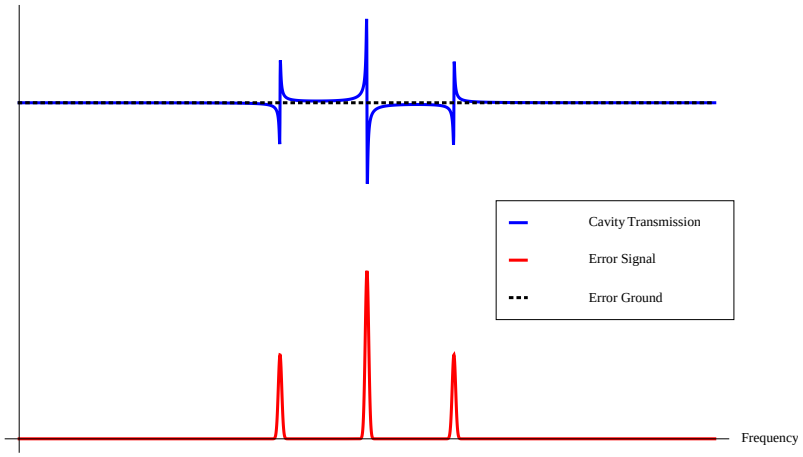

Figure A.3: The lineshape of the error signal derived using the PDH method.

Appendix B

LOCK BOX CIRCUITS

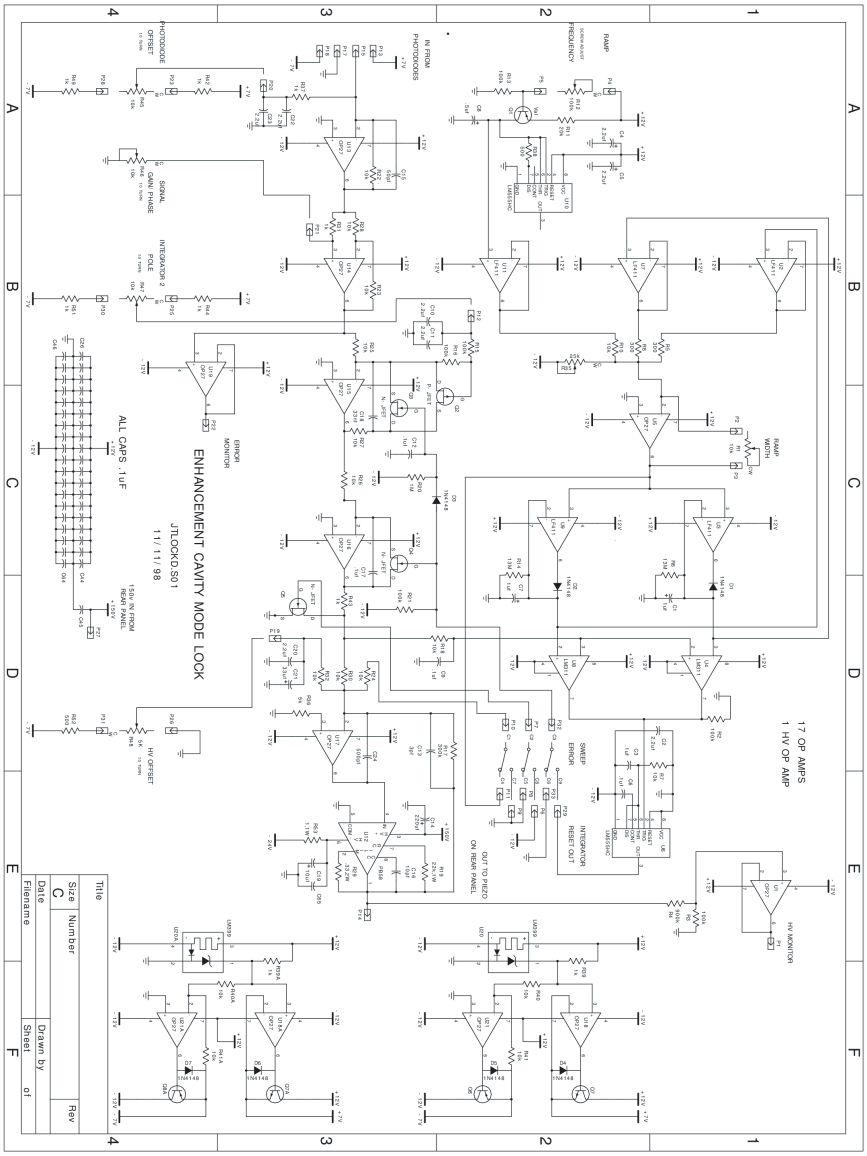

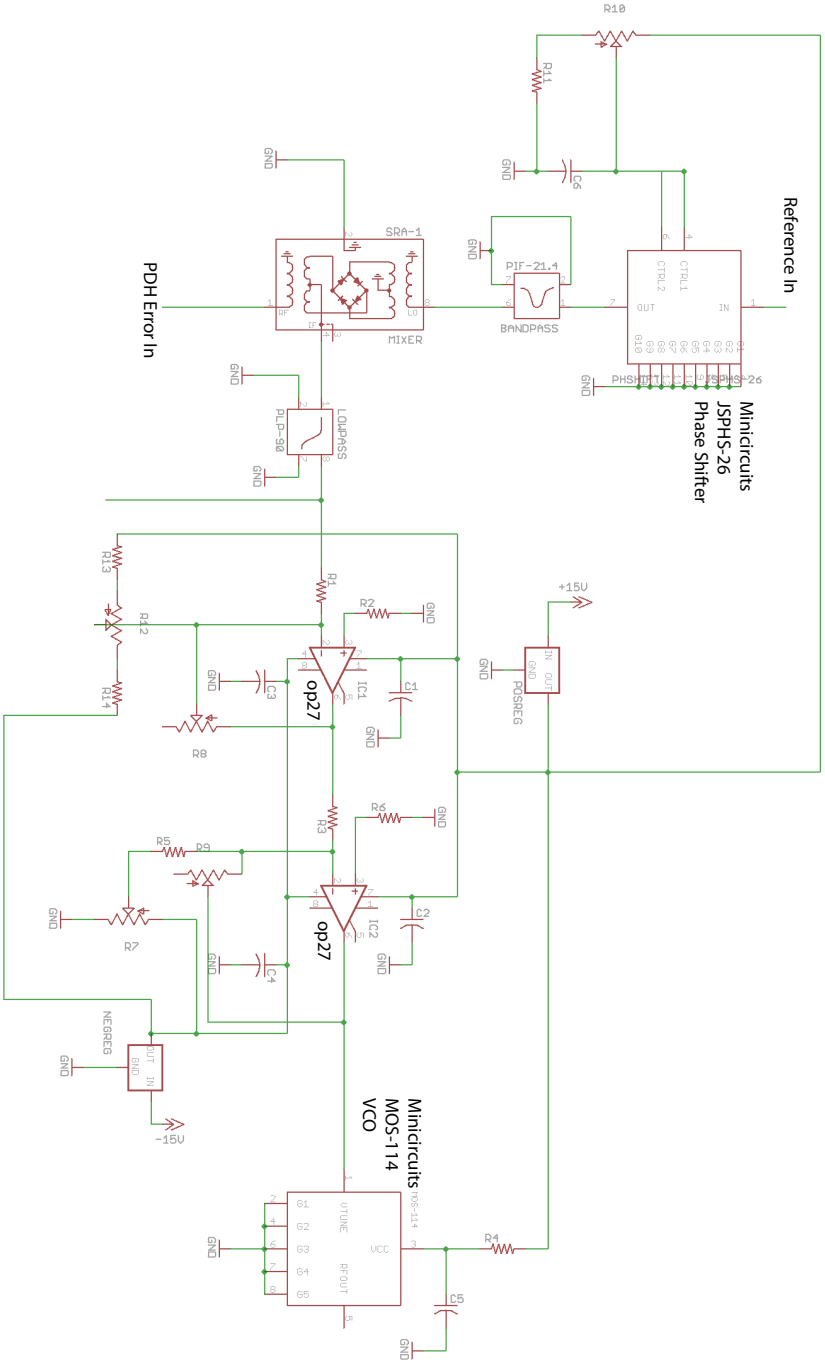

Figure B.1: Fast feedback circuit

Appendix C

NUCLEAR MULTIPOLE OPERATORS

Information about nuclear charge and current distributions is represented quantum mechanically by a nuclear wavefunction. If we wish to extract information about the nucleus from the energy of atomic electrons the Hamiltonian we use to describe the hyperfine interaction ought to contain operators that act on the nuclear wavefunction. Let us first consider the electrostatic interaction between the protons in the nucleus and the outermost bound electron. The electrostatic Coulomb potential for charge configuration at the position of the outermost electron $\vec{r_e}$ is

$$V(r_e) = \sum_n \int \frac{\rho(r_n)}{|\vec{r_e} - \vec{r_n}|} d\tau_n \tag{C.1}$$

where $\rho(r_n) = \psi_N^* \sum_n e g_{ln} \psi_{N'}$ is the nuclear charge density. The sum is over all nucleons and g_{ln} is 1 for protons and 0 for neutrons. If we assume that the electrons occupy a space far away from the nucleus and never enter the region occupied by the nuclear charge ($r_e \gg r_n$) we can perform a multipole expansion of this potential.

$$V(r_e) = e \sum_{n,k} \int \psi_N^* \frac{r_n^k}{r_e^{k+1}} C_e^{(k)} \cdot C_n^{(k)} g_{ln} \psi_{N'} \tag{C.2}$$

where

$$C_{e,n\,q}^{(k)} = \sqrt{\frac{4\pi}{2k+1}} Y_{e,n\,q}^{(k)}(\hat{r})$$

are renormalized spherical harmonics. Electronic wavefunctions for states with non-zero orbital angular momentum go to zero at the origin. Our assumption is therefore reasonable for electrons in non-s orbitals.

Eq. C.2 has the form of a tensor product between a rank-k tensor in electronic coordinates and a rank-k tensor in nuclear coordinates. We can replace these tensors with

quantum mechanical tensor operators

$$D_q^{(k)} = e\sum_e \frac{1}{r_e^{k+1}} C_q^{(k)}(\hat{r}_e)$$
$$F_q^{(k)} = e\sum_n g_{ln} r_n^k C_q^{(k)}(\hat{r}_n) \tag{C.3}$$

and write the electrostatic interaction between the nucleus and outermost electron as a perturbing Hamiltonian

$$H'_e = \sum_{q,k>0} (-1)^k D_q^{(k)} F_{-q}^{(k)}$$
$$= \sum_{k>0} D^{(k)} \cdot F^{(k)} \tag{C.4}$$

where the dot in the previous expression is the scalar product of two equal rank tensors defined in the usual way and the sum does not include the $k = 0$ term which corresponds to the Coulomb interaction and was included in the original Hamiltonian.

Deriving an expression for the magnetic hyperfine Hamiltonian is more complicated for several reasons. If we adopt the gauge

$$\nabla \cdot \vec{A} = 0$$

We can can write an expression for the vector potential at the location of the outermost electron

$$\vec{A}(r_e) = -\sum_n \int \frac{\vec{j}_n}{|\vec{r}_e - \vec{r}_n|} \tag{C.5}$$

While this looks similar to eq. C.1 $\vec{j}_n$ is a vector. A multipole expansion of this expression requires the use of vector spherical harmonics. Also $\vec{j}_n$ must be treated as the sum of two components; a 'convection current' associated with the movement of the charged protons,

$$\vec{j}_c = \frac{e}{2}\left[\psi_N^* \sum_n g_{ln}\vec{v}_n\psi_{N'} - \psi_{N'}\sum_n g_{ln}\vec{v}_n\psi_N^*\right] \tag{C.6}$$

and a spin current from the magnetic moments of the protons and neutrons

$$\vec{j}_s = \nabla \times \psi_N^* \sum_n g_{sn}\frac{e\hbar}{2M_p}\psi_{N'} \tag{C.7}$$

where $g_{sn} = -3.8263$ for neutrons and 5.5856 for protons and we have assumed that protons and neutrons have the same mass M_p. Finally to treat this system of spin 1/2 particles interacting with electromagnetic fields one ought to begin with the Dirac equation rather than the Schroedinger equation. Presenting a complete treatment of this problem would not serve our immediate purpose so without proof we quote the following expression for the multipole expansion of the vector potential eq. C.5.

$$\vec{A}(r_e) = \frac{e\hbar}{2M_p c}\sum_{k,q}\frac{1}{k(k+1)}\vec{L}_e C^{(k)}_{eq} \times \frac{1}{r_e^{k+1}}\int_0^{r_e}\psi^*_N\sum_n \nabla(r_n^k C^{(k)}_{nq})^* \cdot (2g_{ln}\vec{L}_n + (k+1)g_{sn}\vec{S}_n)\psi_{N'}d\tau_N \quad \text{(C.8)}$$

A complete derivation of this expression can be found in a number of atomic physics texts ([1] for example). From eq. C.8 we can form two more tensor operators $M^{(k)}$ and $N^{(k)}$ which like their electric counterparts $D^{(k)}$ and $F^{(k)}$ act on the electric and nuclear wavefunctions respectively.

$$\begin{aligned} M^{(k)}_q &= \sum_e \frac{ie}{r_e^{k+1}}\sqrt{\frac{k+1}{k}}\left(\vec{\alpha}C^{(k)}\right)^{(k)} \\ N^{(k)}_q &= \frac{e\hbar}{2M_p}\sum_n (-1)^q \nabla(r_n^k C^{(k)}_{n-q})^* \cdot \left(\frac{2g_l n}{k+1}\vec{L}_n + g_{sn}\vec{S}_n\right) \\ &= \frac{e\hbar}{2M_p}\sum_n \sqrt{2k(2k-1)+1}\, r_n^{k-1}\left[\frac{2g_{ln}}{k+1}\left(C^{(k-1)}_n \vec{L}_n\right)^{(k)}_q + g_{sn}\left(C^{(k-1)}_n \vec{S}_n\right)^{(k)}_q\right] \end{aligned} \quad \text{(C.9)}$$

The Hamiltonian describing the Hyperfine interaction can be written as

$$H_{hyp} = \sum_{k>0}\underbrace{G^{(k)}\cdot F^{(k)}}_{electric} + \underbrace{M^{(k)}\cdot N^{(k)}}_{magnetic} \quad \text{(C.10)}$$

Appendix D

THE SECOND ORDER HYPERFINE INTERACTION

Second order energy corrections are of the form

$$E''_{IJF,J'} = \frac{1}{E_{\gamma J} - E_{\gamma' J'}} \sum_{k_1,k_2} \left\langle \gamma J I F m_F \right| T_e^{(k_1)} \cdot T_n^{(k_1)} \left| \gamma' J' I F m_F \right\rangle \times \left\langle \gamma' J' I F m_F \right| T_e^{(k_2)} \cdot T_n^{(k_2)} \left| \gamma J I F m_F \right\rangle \quad \text{(D.1)}$$

where the tensors $T_{e,n}^{(k)}$ can be either the electric or magnetic tensor operators. Using the Wigner-Eckart theorem this can be rewritten in terms of reduced matrix elements.

$$E''_{IJF,J'} = \frac{1}{E_{\gamma J} - E_{\gamma' J'}} \sum_{k_1,k_2} \begin{Bmatrix} F & J & I \\ k_1 & I & J' \end{Bmatrix} \begin{Bmatrix} F & J & I \\ k_2 & I & J' \end{Bmatrix} \left\langle T_n^{(k_1)} \right\rangle_{II} \left\langle T_n^{(k_2)} \right\rangle_{II} \times \left\langle \gamma J \left\| T_e^{(k_1)} \right\| \gamma' J' \right\rangle \left\langle \gamma' J' \left\| T_e^{(k_2)} \right\| \gamma J \right\rangle \frac{(2I+1)}{\langle II k_1 0 |\, II \rangle \langle II k_2 0 |\, II \rangle} \quad \text{(D.2)}$$

Similar to our definition of A, B, and C let us define coupling coefficients containing the off-diagonal nuclear and electronic matrix elements that arise in second order perturbation theory. Again we note that these coupling coefficients depend on J and I but are independent of F.

$$\begin{aligned} \eta &= \mu^2 \frac{(I+1)(2I+1)}{I} \frac{\left| \left\langle \gamma J \left\| M^{(1)} \right\| \gamma' J' \right\rangle \right|^2}{E_{\gamma J} - E_{\gamma' J'}} \\ \zeta &= \mu \frac{Q}{2} \frac{(I+1)(2I+1)}{I} \sqrt{\frac{2I+3}{2I-1}} \frac{\left\langle \gamma J \left\| M^{(1)} \right\| \gamma' J' \right\rangle \left\langle \gamma J \left\| D^{(2)} \right\| \gamma' J' \right\rangle}{E_{\gamma J} - E_{\gamma' J'}} \\ \lambda &= \left(\frac{Q}{2} \right)^2 \frac{I(2I+1)(2I-1)}{(2I+3)(I+1)} \frac{\left| \left\langle \gamma J \left\| D^{(2)} \right\| \gamma' J' \right\rangle \right|^2}{E_{\gamma J} - E_{\gamma' J'}} \end{aligned} \quad \text{(D.3)}$$

$$O_1 = -\mu\Omega\frac{(I+1)(2I+1)}{I}\sqrt{\frac{(2I+3)(I+2)}{(2I-1)(I-1)}}\frac{\langle\gamma J\left\|M^{(1)}\right\|\gamma' J'\rangle\langle\gamma J\left\|M^{(3)}\right\|\gamma' J'\rangle}{E_{\gamma J}-E_{\gamma' J'}}$$
$$O_2 = -\frac{1}{2}Q\Omega\frac{(I+1)(2I+1)}{I}\frac{2I+3}{2I-1}\sqrt{\frac{(I+2)}{(I-1)}}\frac{\langle\gamma J\left\|D^{(2)}\right\|\gamma' J'\rangle\langle\gamma J\left\|M^{(3)}\right\|\gamma' J'\rangle}{E_{\gamma J}-E_{\gamma' J'}}$$
$$O_3 = \Omega^2\frac{(I+1)(2I+1)}{I}\frac{2I+3}{2I-1}\frac{I+2}{I-1}\frac{\left|\langle\gamma J\left\|M^{(3)}\right\|\gamma' J'\rangle\right|^2}{E_{\gamma J}-E_{\gamma' J'}} \tag{D.4}$$

η, ζ, and λ contain the dipole-dipole, dipole-quadrupole, and quadrupole-quadrupole off diagonal matrix elements. O_1, O_2, and O_3 contain the dipole-octupole, quadrupole-octupole, and octupole-octupole off diagonal matrix elements. The second order correction to a hyperfine sublevel is given by

$$E''_{IJF,J'} = \begin{Bmatrix} F & J & I \\ 1 & I & J' \end{Bmatrix}^2\eta + \begin{Bmatrix} F & J & I \\ 1 & I & J' \end{Bmatrix}\begin{Bmatrix} F & J & I \\ 2 & I & J' \end{Bmatrix}\zeta + \begin{Bmatrix} F & J & I \\ 2 & I & J' \end{Bmatrix}^2\lambda$$
$$+\begin{Bmatrix} F & J & I \\ 1 & I & J' \end{Bmatrix}\begin{Bmatrix} F & J & I \\ 3 & I & J' \end{Bmatrix}O_1+\begin{Bmatrix} F & J & I \\ 2 & I & J' \end{Bmatrix}\begin{Bmatrix} F & J & I \\ 3 & I & J' \end{Bmatrix}O_2+\begin{Bmatrix} F & J & I \\ 3 & I & J' \end{Bmatrix}^2 O_3 \tag{D.5}$$

If we add these second order corrections to our expressions for the frequency intervals ΔE_0, ΔE_1, and ΔE_2 in the $5D_{3/2}$ level we have

$$\Delta E_0 = -A + B - 56C - \frac{1}{100}\eta + \frac{1}{100}\sqrt{\frac{7}{3}}\zeta + \frac{7}{300}\lambda + \frac{1}{25\sqrt{6}}O_1 + \frac{1}{25\sqrt{6}}O_2 + \frac{2}{75}O_3$$
$$\Delta E_1 = -2A + B + 28C + \frac{1}{75}\eta - \frac{1}{75}\lambda - \frac{1}{25}\sqrt{\frac{2}{3}}O_1 - \frac{1}{25}\sqrt{\frac{2}{3}}O_2 - \frac{8}{525}O_3$$
$$\Delta E_2 = -3A - B - 8C + \frac{1}{300}\eta + \frac{1}{20}\sqrt{\frac{3}{7}}\zeta + \frac{1}{700}\lambda + \frac{3}{175}\sqrt{\frac{3}{2}}O_1 + \frac{3}{175}\sqrt{\frac{3}{2}}O_2 - \frac{13}{1225}O_3 \tag{D.6}$$

If we solve this system of equations for the magnetic octupole moment hyperfine constant C we have

$$C(5D_{3/2}) = -\frac{1}{80}\Delta E_0^{(3/2)} + \frac{1}{100}\Delta E_1^{(3/2)} - \frac{1}{400}\Delta E_2^{(3/2)}$$
$$+ \frac{1}{2000\sqrt{21}}\zeta + \frac{3}{7000}\lambda + \frac{1}{700\sqrt{6}}O_1 + \frac{1}{700\sqrt{6}}O_2 + \frac{9}{19600}O_3 \tag{D.7}$$

Notice that equation D.7 does not depend on η. This is fortunate for us as it is one less source of theoretical uncertainty in our measurement of $C(5D_{3/2})$. Furthermore it can be shown that the third order dipole-dipole-dipole dependence in $C(5D_{3/2})$ must also vanish as will all other higher order dipole^n terms [5]. Electronic matrix elements of the rank 1 and 2 tensor operators $M^{(1)}$ and $D^{(2)}$ have been calculated [4] allowing us to evaluate the ζ and λ terms in eq. D.7.

$$\begin{aligned}\left\langle 5D_{3/2} \left\| M^{(1)} \right\| 5D_{5/2} \right\rangle &= -1160 \frac{\text{MHz}}{\mu_N} \\ \left\langle 5D_{3/2} \left\| D^{(2)} \right\| 5D_{5/2} \right\rangle &= 270 \frac{\text{MHz}}{\text{b}}\end{aligned} \tag{D.8}$$

Using the definitions of ζ and λ in equation D.3 we have

$$\begin{aligned}\frac{1}{2000\sqrt{21}}\zeta &= 1.59\text{Hz} \\ \frac{3}{7000}\lambda &= .28\text{Hz}\end{aligned}$$

The calculated values for these terms can be added as a correction to the frequency intervals we measure. An alternative method for eliminating the dependence of $C(5D_{3/2})$ on the second order dipole-quadrupole shift would be

The magnitude of the octupole coupling terms in eq. D.7 can be estimated if we assume that the off diagonal reduced matrix elements of electronic tensor operators contained in the coefficients O_1, O_2, O_3 are of the same order of magnitude as the diagonal matrix element of the same operator. Also the difference in frequency between the $5D_{3/2}$ levels and the $5D_{5/2}$ levels is approximately 24 THz.

$$\begin{aligned}\frac{1}{700\sqrt{6}}O_1 &\sim \frac{A(5D_{3/2})\, C(5D_{3/2})}{E_{5D_{5/2}} - E_{5D_{3/2}}} \sim 10^{-7}\text{ Hz} \\ \frac{1}{700\sqrt{6}}O_2 &\sim \frac{B(5D_{3/2})\, C(5D_{3/2})}{E_{5D_{5/2}} - E_{5D_{3/2}}} \sim 10^{-8}\text{ Hz} \\ \frac{9}{19600}O_3 &\sim \frac{C(5D_{3/2})^2}{E_{5D_{5/2}} - E_{5D_{3/2}}} \sim 10^{-14}\text{ Hz}\end{aligned}$$

We can safely assume that the second order octupole terms and other higher order terms will not contribute significant shifts to the octupole coupling constant $C(5D_{3/2})$.